Reservoir characterization of the Stø formation in the Hammerfest Basin, SW Barents Sea

Reservoir quality as a function of provenance, depositional environment and diagenesis

Henrik Nygaard Hansen

Master Thesis in Geosciences
Petroleum Geology and Petroleum Geophysics
30 credits

Department of Geosciences
Faculty of Mathematics and Natural Sciences

UNIVERSITY OF OSLO

01.06.2016

Reservoir characterization of the Stø formation in the Hammerfest Basin, SW Barents Sea

Reservoir quality as a function of provenance, depositional environment and diagenesis

Henrik Nygaard Hansen

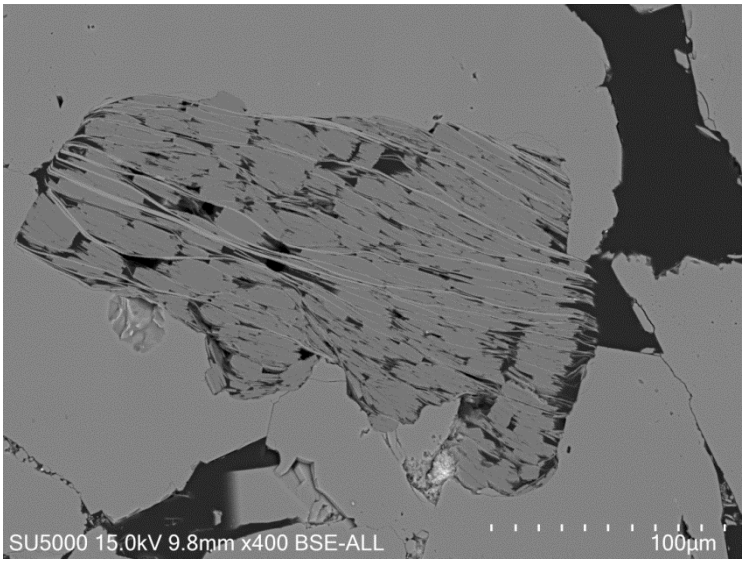

Master Thesis in Geosciences
Petroleum Geology and Petroleum Geophysics
30 credits

Department of Geosciences
Faculty of Mathematics and Natural Sciences

UNIVERSITY OF OSLO

01.06.2016

Reservoir characterization of the Stø formation in the Hammerfest Basin, SW Barents Sea

Henrik Nygaard Hansen

http://www.duo.uio.no/

Printed: Reprosentralen, University of Oslo

Acknowledgements

First of all, I would like to thank my supervisor professor Jens Jahren for valuable guidance in the preparation of this thesis.

I would also like to thank Lina Hedvig Line for assistance in the microscopy-lab and Berit Løken Berg for support in the SEM-lab.

Thanks to all my fellow students at Blindern and especially my friends Kristoffer, Jørgen and Hans-Martin.

Finally, I would like to thank my family for massive support throughout my academic years at the University of Oslo.

Henrik Nygaard Hansen

30.05.2016

University of Oslo

Abstract

A reservoir characterization of the Stø formation has been performed in two wells linked to the Snøhvit field within the Hammerfest Basin in the South-Western Barents Sea. The reservoir quality of the Stø formation has been described as a function of provenance, depositional environment and diagenesis where both a petrographic- and a petrophysical approach has been implemented. The primary focus has been to investigate processes which have had an influence on the reservoir quality in the Stø formation, with special regard to porosity.

Provenance and depositional environment have been of great importance for the resultant reservoir quality within the Stø formation as these processes determined initial rock properties such as mineralogy, sorting and grain size. The mature mineralogy of the Stø formation has been linked to leaching and reworking of the sediments prior to final deposition, whereas the detrital clay content has been related to a transgressive development of the shoreline in a shallow marine setting.

IGV results with respect to grain size indicate that intervals consisting of very fine sand had the best preserved porosity after mechanical compaction, whereas the same intervals indicate significant porosity reduction during the chemical compaction regime, due to quartz cementation. Highly cemented intervals have been linked to the distance between stylolites and the relative amounts of micro-stylolites, which is thought to be the most prominent silica dissolving mechanism. A relationship between quartz cement and porosity shows that quartz cementation is the major porosity reducing mechanism at depth within the Stø formation. The lower part of the Stø formation have the best preserved porosity and lies in the range of 8-13%, whereas upper part of the Stø formation have porosity values ranging from 4-14%. However, the majority of the porosity data are below 8% within the upper part of the Stø formation.

Authigenic kaolinite and illite has been suggested to have a minor influence on the reservoir quality within the Stø formation, due to the relatively small amounts of these clay minerals compared to the bulk volume. Thin clay laminations were sporadically observed within the upper part of the Stø formation that also is intervals with a high quartz cement volume. These intervals may reduce the vertical permeability.

Table of Contents

1. Introduction

1.1 Introduction

This thesis is a part of the Master`s degree program "Petroleum Geology and Petroleum Geophysics" at the University of Oslo and was compiled from the 05.01.2016 – 01.06.2016.

An integral part of petroleum exploration includes thorough analysis of the reservoir properties in the subsurface. Porosity and permeability are important parameters in terms of reservoir quality as these determine the hydrocarbon storage capacity and rate of fluid flow within a reservoir. Reservoir quality is a function of provenance, depositional environment and diagenesis where a great variety of processes may alter reservoir properties form the time of deposition, to the resultant reservoir quality observed at depth. Therefore, it is crucial to have an understanding of these processes in order to successfully predict the reservoir quality. This study aims to characterize the reservoir quality within the Stø formation from two wells located in the Hammerfest basin in the South-Western Barents Sea (SW Barents Sea).

1.2 Research objectives and methods

This project aims to describe the reservoir quality within the Stø formation by utilizing geophysical well logs and core material from two wells related to the Snøhvit field in the Hammerfest basin. The results will aim to describe various properties with regard to the Stø formation and link the observations to provenance, depositional environment and diagenesis. Finally, the aim will be to relate these processes to the reservoir quality of the Stø formation. The Petrographic results will be obtained by examine thin sections using an optical microscope, electron microscope (SEM) and Cathotoluminescence (CL). The petrophysical analysis will be carried out in the computer software Hampson and Russell (HRS) and Petrel, where geophysical well logs will be examined.

1.3 Study area

The Barents Sea is situated on the north-western corner of the Eurasian plate and covers an area of approximately 1.3 million km^2 (Ohm et al., 2008), and is one of the largest continental shelfs on the Earth today (Smelror et al., 2009). The Barents Sea is limited by the Norwegian mainland and the Kola Peninsula in the south, the Novaya Zemyla in the east, the Franz Josef Land and Svalbard in the North and a continental margin in the west, which separates the Barents shelf from the Norwegian Sea (Figure 1.1). This area has been formed in response to a complex geological history and is characterized by geological features such as basins, highs and platforms (Faleide et al., 1984, Doré, 1995). The Barents shelf can be dived into an eastern- and western region in terms of the geological evolution and corresponds approximately to the boundary between the Norwegian- and Russian sector (Worsley, 2008). The Hammerfest basin is situated in the SW Barents Sea (Figure 1.1) and is an important area on the Norwegian continental shelf in terms of petroleum resources. This area was initially targeted because reflection seismic data, acquired in 1970, had proven thick sedimentary successions in this region which were thought to contain reservoirs similar to the earlier discoveries in the North Sea (Doré, 1995). Today about 25 discoveries are made in the Barents Sea and several of them are located in the Hammerfest basin region where the hydrocarbon accumulations are mainly located in sandstones of Jurassic age (Faleide et al., 2015). In this project, two wells linked to the Snøhvit field in the Hammerfest basin will be studied (figure 1.2). The geological evolution of the Barents Sea and especially the Hammerfest basin area will be further presented in chapter 2.

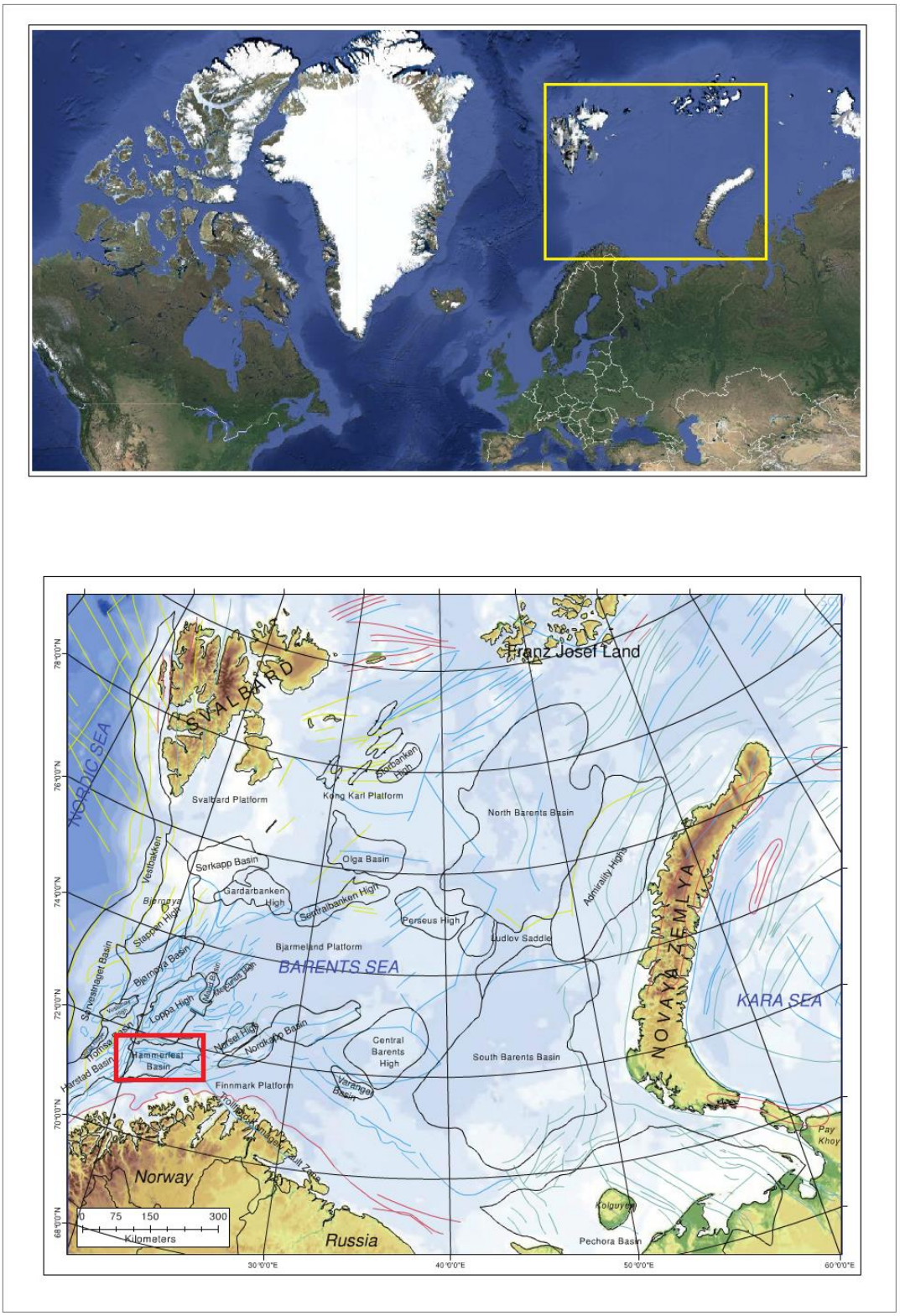

Figure 1.1: The figure shows the location of the Barents Sea (marked in yellow) and the location of the Hemmerfest Basin within the Barents sea (marked in red). Upper picture taken from Google Maps (maps.google.com). Lower picture modified from (Smelror et al., 2009).

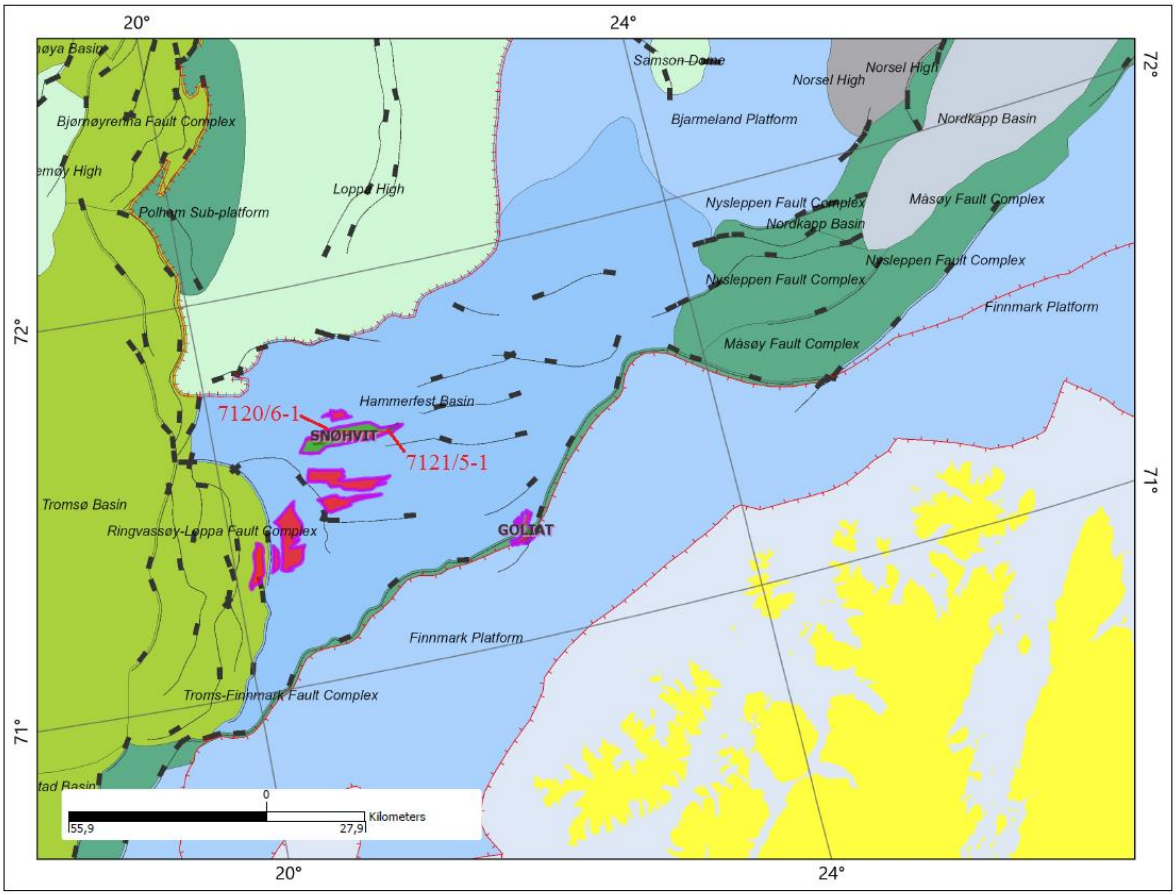

Figure 1.2: The figure displays the location of the two wells studied in this thesis. The picture is taken from (NPD, 2016).

1.4 Chapter description

The geological evolution of the Barents region and more specifically the Hammerfest basin will be presented in chapter 2. This will include a more detailed description of the Triassic and Jurassic sediments and the Stø formation. In chapter 3, a general overview of common diagentical processes within reservoir sandstones will be given and this will form the basis for the interpretation of the results obtained in this study. Chapter 4 will describe the methods and data used to obtain the results in this study. Further, in chapter 5 and 6, the results from the petrographic- and petrophysical analysis will be presented, respectively. In chapter 7 a discussion will aim to relate the observations from the petrographic- and petrophysical analysis to provenance, depositional environment and diagenesis and further to the reservoir quality of the Stø formation. Conclusions will be presented in chapter 8.

2. Geological setting – The Hammerfest basin

2.1 Introduction – General overview of the Barents Sea

The Barents Sea is situated north of Norway and is one of the largest continental shelfs on the Earth today. The Barents Sea is limited by Svalbard and Franz Josef Land in the north, Novaya Zemlya in the east and the Kola Peninsula and the Norwegian mainland in the south (Figure 1.1). The regional geological evolution of the Barents Sea is mainly a result of large scale processes related to plate tectonics, climatic changes and alteration in depositional setting. The continent collision between Laurentia and Baltica resulted in the the Caledonian Orogeny in the Early Devonian and the later breakup and opening of Norwegian and Greenland Sea in the Cenozoic, are events related to large scale plate tectonics (Smelror et al., 2009, Duran et al., 2013). The Barents Sea was influenced by crustal extension on a regional scale in the Late Paleozoic, while a later westward propagation of the rifting, led eventually to well-developed rift- and pullapart basins in the SW Barents Sea. This area is affected by a series of tectonic events since the Caledonian breakup, where three major rift phases in late Devonian-Carboniferous, Middle Jurassic –Early Cretaceous and Early Tertiary are considered the most prominent (Duran et al., 2013, Faleide et al., 2015). The eastern part of the basin has been influenced by the Uralian Orogeny and tectonically events related to the Novaya Zemlya (Smelror et al., 2009), but has been more tectonically stable since the late Carboniferous (Gabrielsen et al., 1990). Today the western part of the Barents Sea is associated with several structural features such as deep basins, highs and platforms (Faleide et al., 1984), while the eastern part is mainly dominated by two major basins, known as the Northern- and Southern Barents basin (Worsley, 2008). The SW Barents Sea is bounded by the continental margin in the west, comprising the Senja Fracture Zone in the south and Hornsund fault zone further north, the Norwegian coast in the south, Svalbard in the North and the Central Barents High in the east. The sedimentary successions deposited in the SW Barents Sea are affected by the structurally evolution of the Barents Sea through time and deposits ranging from Paleozoic to Cenozoic in age are present (Faleide et al., 2015). The Hammerfest basin is situated within this region.

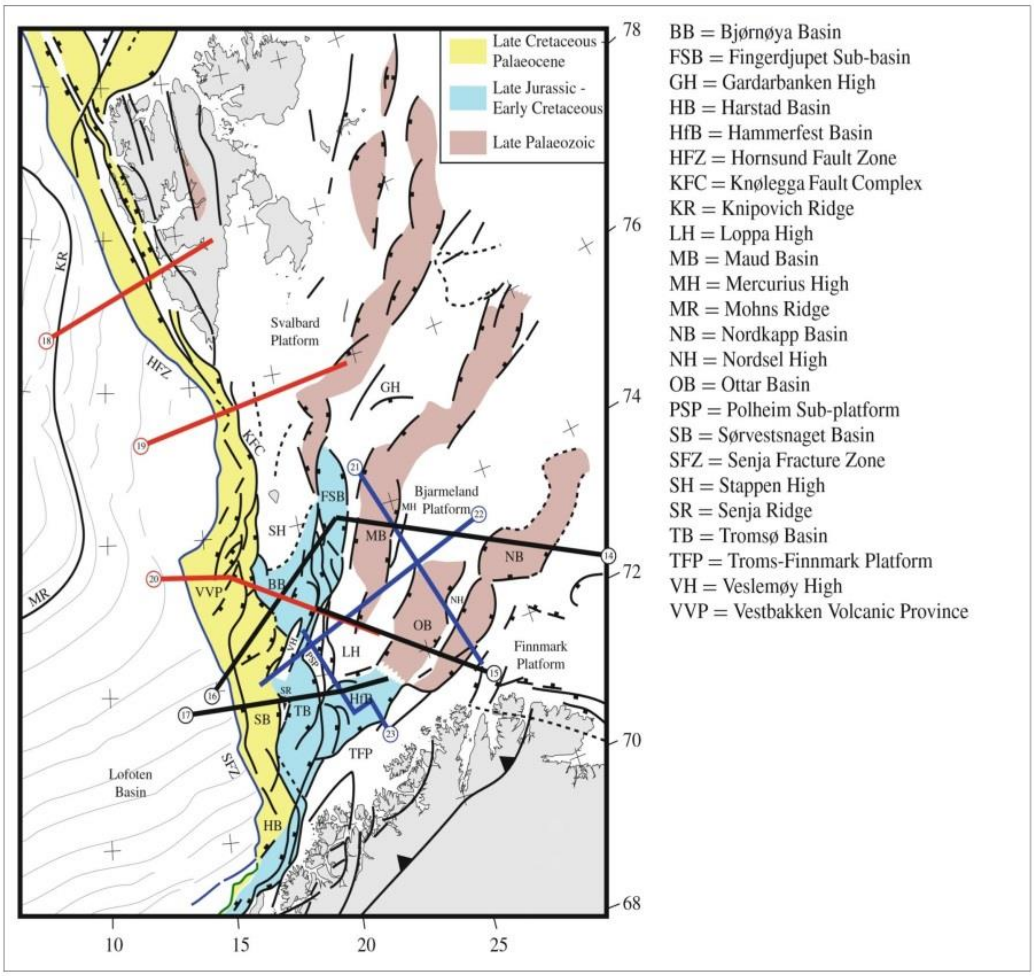

Figure 2.1: The figure shows the main structural elements in the SW Barents Sea (Faleide et al., 2015).

2.2 Geological evolution of the Hammerfest basin

The Hammerfest basin comprises rocks ranging from Carboniferous to Mid-Upper Cenozoic in age (Figure 2.2). Early basin development was created by an E-W oriented extensional regime, followed by the Caledonian Orogeny, which dominated from the Mid-Late Carboniferous and into the Mesozoic (Berglund et al., 1986). This rift event has been related to the north-eastern Atlantic rift between Norway and Greenland and created a several hundred km wide rift zone (Faleide et al., 2015). The western Barents Sea was dominated by highlands, fluvial- and alluvial settings which transported sediments into the newly formed basins. The western Barents Sea region was partly transgressed in Late Carboniferous and shallow shelf environments dominated in the basins where carbonates eventually started to accumulate. Some clastic sediments were still deposited at the basin margins as continental

conditions acted at the structural highs in the area. Further into the Permian, in response to a regional subsidence, an extensive carbonate platform established in the western Barents Sea (Smelror et al., 2009)

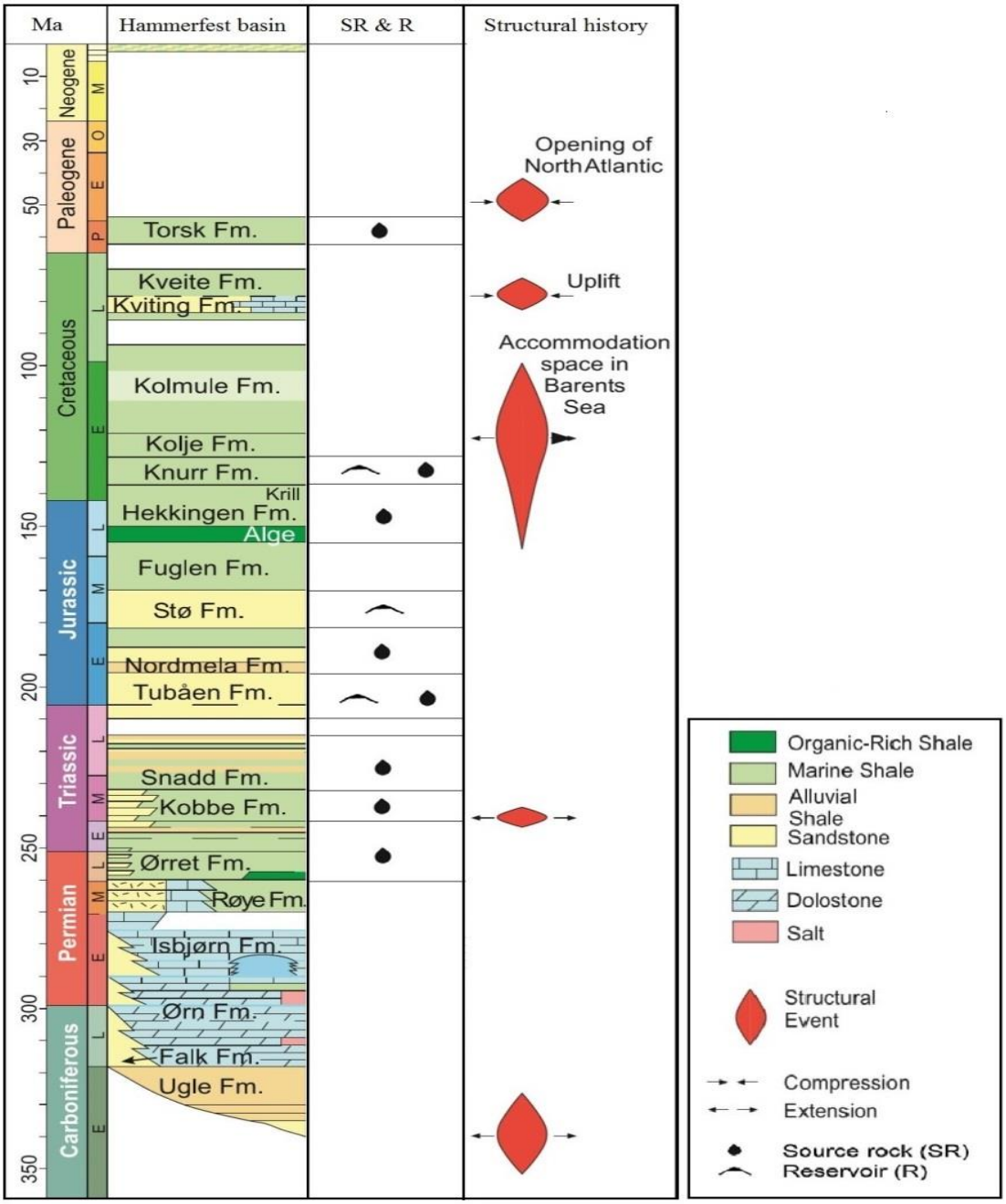

Figure 2.2: Stratigraphic column of the Hammerfest basin. The figure also includes the potential reservoir- and source rocks in area. Modified from (Ohm et al., 2008) and (Duran et al., 2013).

In the early Mesozoic, considerably amounts of sediments came in from the Uralian mountains and the Baltic Shield and the carbonates were overlain by clastic deposits, mainly sandstones and shales (Faleide et al., 2015). Marine environments dominated in the Late Permian to early Triassic, while an onset of a prograding deltaic system towards the north-west led to increasingly proximal sandy deposits on a regional scale in the Middle Triassic (Worsley, 2008, Glørstad-Clark et al., 2010) (Figure 2.3). Several deposits from upper Triassic –Mid Jurassic represents facies associated with shallow marine environments (Worsley, 2008), and established in response to a major transgression in the Late Triassic (Halland et al., 2013). These sandstones are the main reservoir sands in SW Barents Sea and comprise the Stø formation. Further, a regional transgression late in the Middle Jurassic in combination with the Mid-Jurassic – Early Cretaceous rift phase led to deposition of organic rich shales, especially towards the Upper Jurassic. The stratigraphically important unit, the Hekking formation, was formed during this event which is an important source rock in SW Barents Sea (Worsley, 2008).

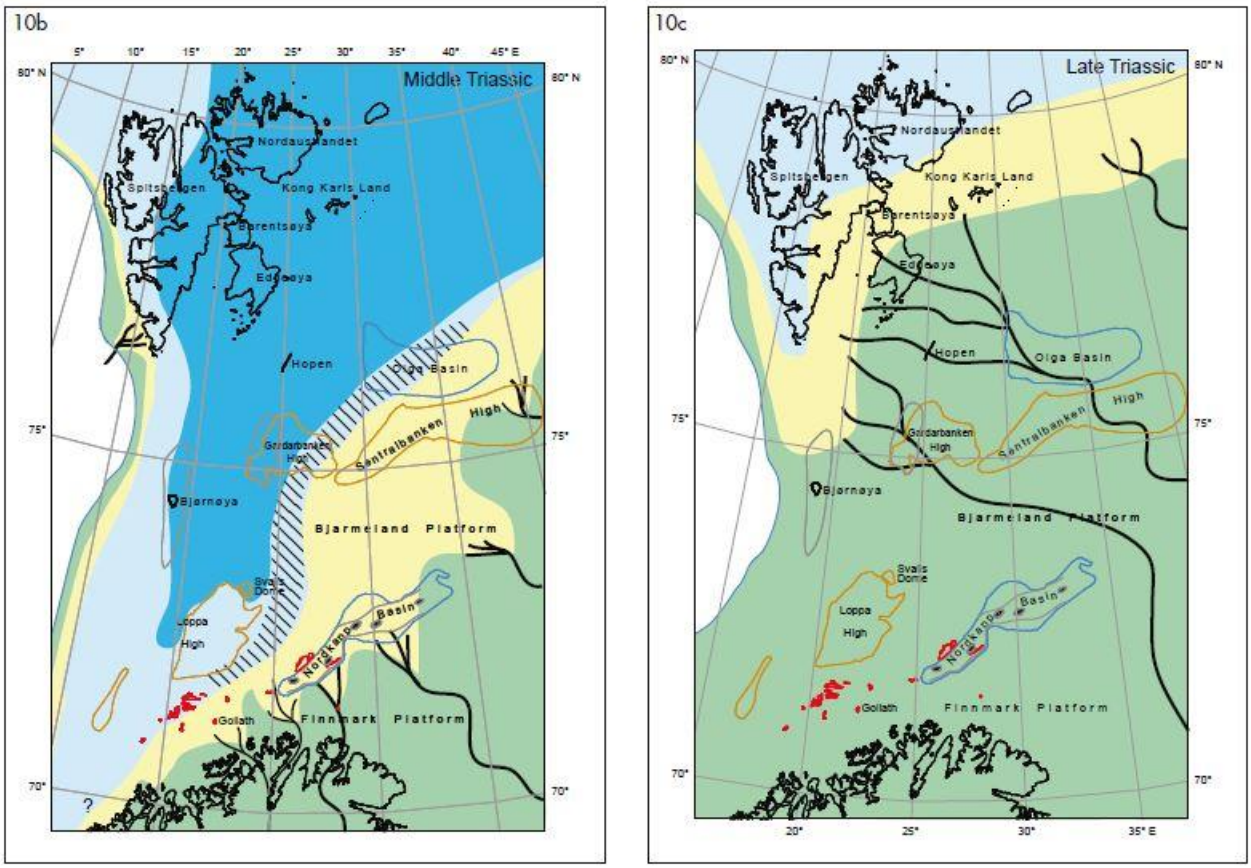

Figure 2.3: Reconstruction of the Triassic prograding deltaic system, after (Lundschien et al., 2014)

The Jurassic – Cretaceous transition is represented by a change in the depositional environment caused by a lowering of the sea level and less organic rich thick shale deposits dominate the basin infill (Worsley, 2008). The northern Barents Sea was influenced by widespread magmatism which originated from an igneous province in the Arctic during the Early Cretaceous. In Late Cretaceous the northern parts of the Barents Sea were influenced by uplift and erosion leading to exposure of basement and sediments from Upper Paleozoic (Worsley, 2008). On the contrary, sediments were still deposited in the SW region and Cretaceous successions are recognized both from the Tromsø- and Hammerfest basin. The Lower Cenozoic times is characterized by tectonic activity related to the western shelf margin, followed by the opening of the Norwegian-Greenland Sea. The continental breakup started by a continental strike-slip system, which was active during the Paleocene-Eocene and eventually a megashear zone developed all the way up to the Eurasian Basin, leading to break-up in the Oligocene time. Further, uplift of the Barents Sea in the Late Cenozoic resulted in erosion of most of the sedimentary successions from this period (Faleide et al., 2015).These sediments were deposited as clastic wedges at the western margin of the Barents Sea. The uplift during the Pliocene and Pleistocene (Cenozoic) seems to have been most prominent in the northwestern part, where 3000 meter of the sediments are removed. Further southwest the removal of sediments are estimated to 1000-1500 meters (Faleide et al., 2015). These Cenozoic sediments are represented by thinner successions at the structural highs and platforms compared to the deeper basins (Gabrielsen et al., 1990).

2.3 The Hammerfest basin

The Hammerfest basin is situated in the SW Barents Sea between Loppa high in the north, the Bjarmeland Platform in the east, the Finnmark platform in the south and the Tromsø Basin towards west. It is located between 70°50`N, 20°E, 71°15`N, 20°E, 72°15`N, 23°15`E and 71°40`N, 24°10`E (Figure 2.4, 2.5). The Hammerfest Basin is 150 km long and 70 km wide oriented ENE-WSW and is a relatively shallow basin in comparison to the deeper Tromsø basin (Gabrielsen et al., 1990, Ostanin et al., 2012). This basin is one of the most interesting areas in the Barents Sea regarding petroleum exploration and contains four significant discoveries which can be seen in figure 2.4. By 2011, a total of 90 wells are drilled in the southern Barents Sea and one third of these are located within the Hammerfest basin (Ostanin et al., 2012).

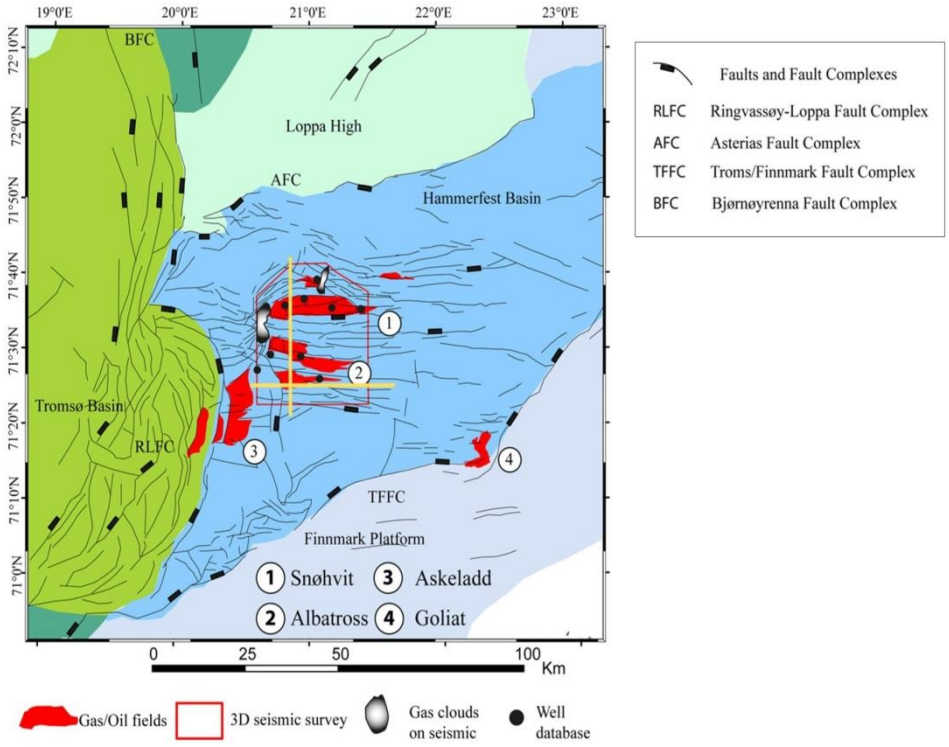

Figure 2.4: This figure shows the main fault systems limiting the Hammerfest basin as well as intra basinal faults from upper Jurassic level. The most most important gas/oil fileds in this region is also marked (Ostanin et al., 2012).

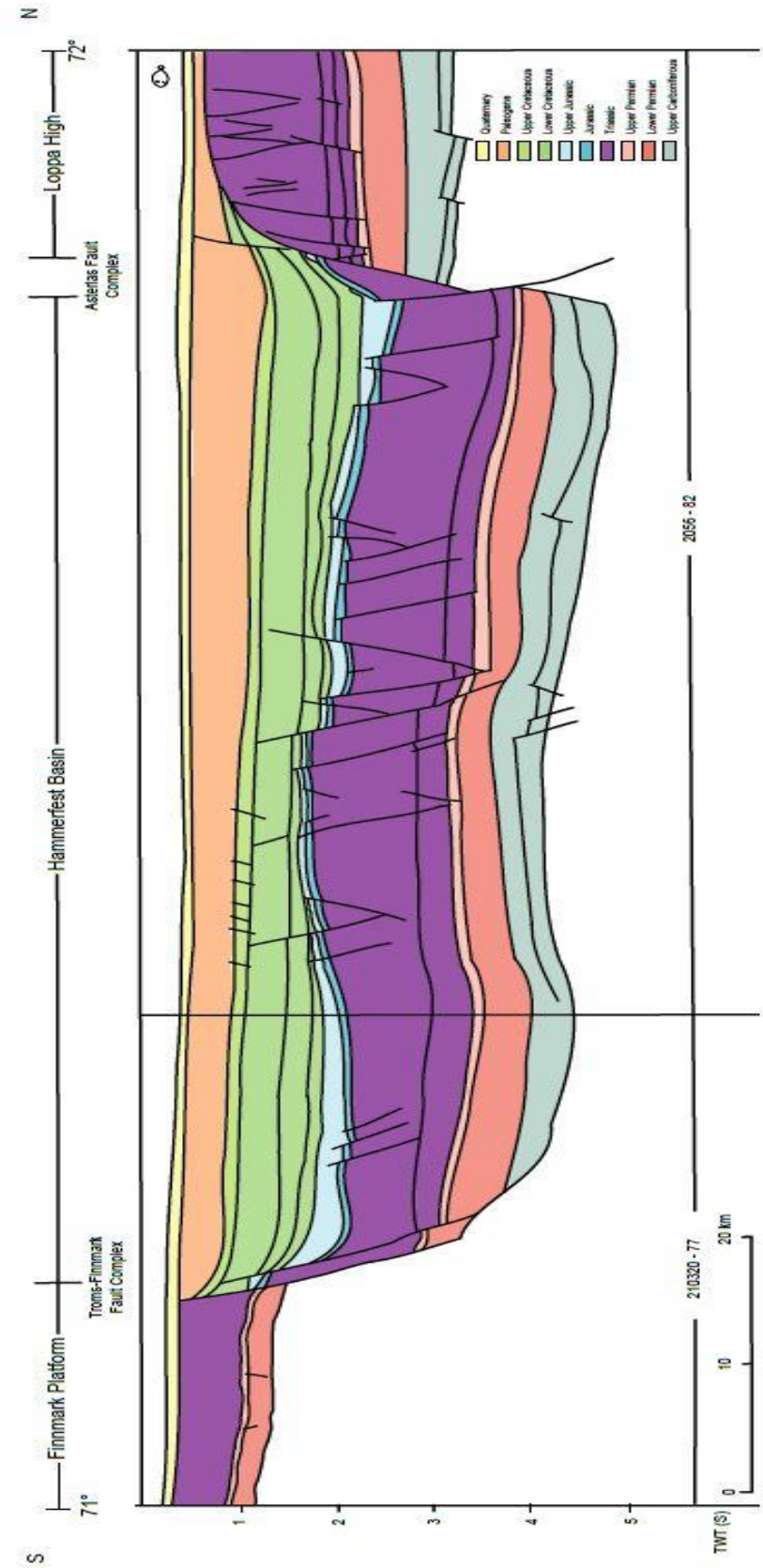

Figure 2.5: The figure displays a N-S cross-section of the Hammerfest exstending from the Loppa High in the north towards the Finnmark Platfrom in the south (Halland et al., 2013).

2.3.1 Structural setting

The Hammerfest basin is a fault controlled basin where the basin margins are limited by the Troms Finnmark Fault Complex (TFFC) in the south towards the Finnmark Platfrom and in the north towards Loppa high by the Asterias Fault Complex. It is separated from the Tromsø basin by the Ringvassøy-Loppa Fault Complex in the west, while the eastern boundary towards the Bjarmeland Platform is less fault influenced and shows characteristics more like a sag basin (Gabrielsen et al., 1990)(figure 2.6). The intra-basinal faults are oriented E-W and is parallel to a wide dome-shaped structure situated in the central part of the basin. This group of faults is termed the Hammerfest Basin Fault System (HBFS). The HBFS is marginally oblique to the overall striking axis of the basin and the TFFC which are oriented more or less ENE-WSW. In addition, the Ringvassøy-Fault Complex is oriented NNE-SSW, nearly perpendicular to the HBFS (Gabrielsen, 1984). This indicates several tectonic events which has influenced the basin margins and the intra-basinal fault system which has been related to uplift of the central dome structures (Øvrebø and Talleraas, 1977). The Hammerfest basin was most likely established during the Early to Late Carboniferous rifting, indicated by a well on the southern margin where basement overlain by Permian rocks were penetrated (Halland et al., 2013). In the Late Jurassic - Early Cretaceous the Hammerfest developed into a more mature basin with fault activity and uplift both in intra-basin- and margin areas (Berglund et al., 1986).

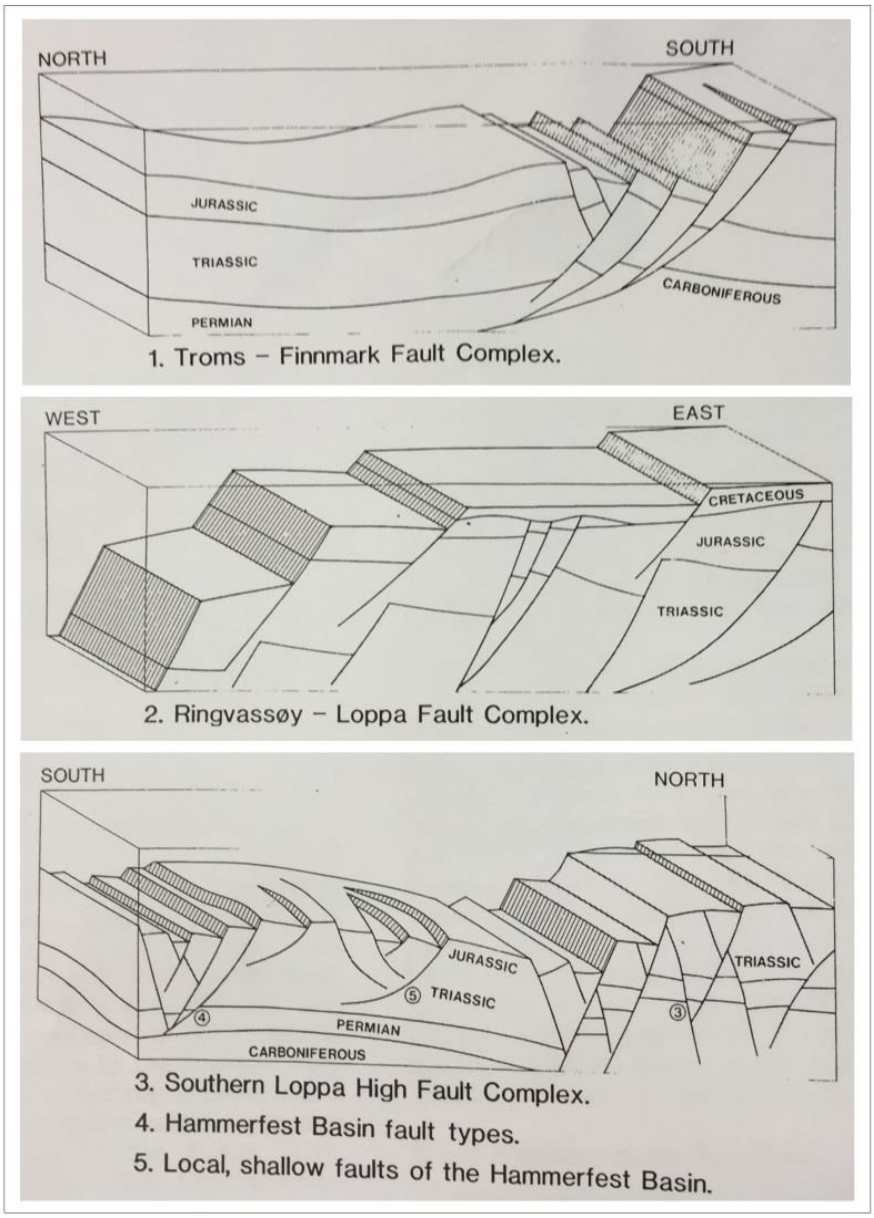

Figure 2.6: An outline of the architecture of the various fault systems related to the Hammerfest basin margins or intra-basinal areas are presented in this figure. From (Berglund et al., 1986).

2.3.2 Stratigraphy

The sedimentary successions in the Hammerfest basin reflect largely the regional evolution of the western Barents Sea (figure 2.2). In the following, a brief introduction to the Triassic and Jurassic successions will be given (Figure 2.7). A more detailed presentation of Stø formation (Mid Jurassic) will be given in section 2.5. The presented nomenclature is taken from Mørk et al. (1999) and formation characterization is mainly obtained from Dalland et al. (1988).

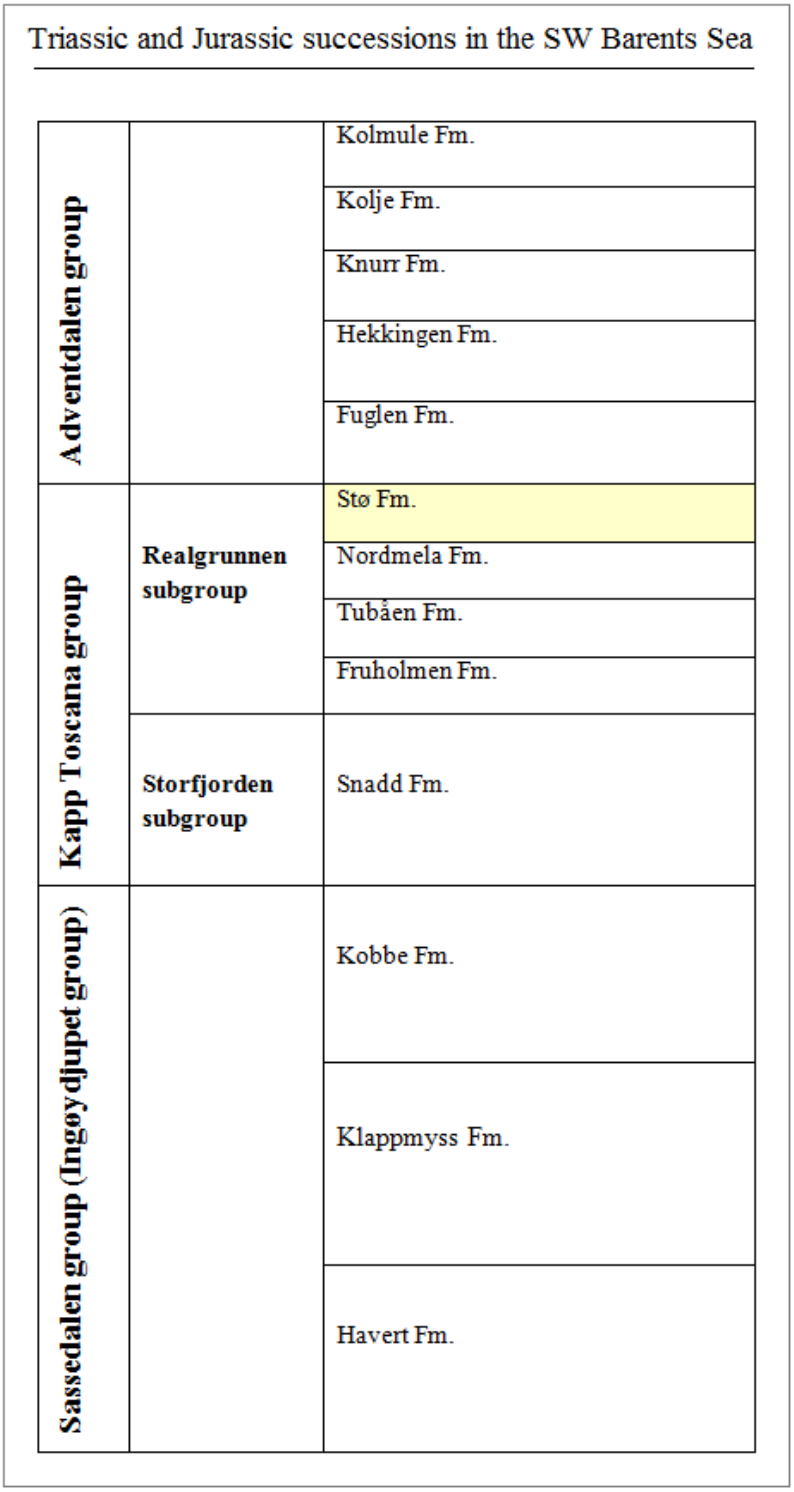

Figure 2.7: A schematically representation of the Triassic and Jurassic lithostratigraphy in the Hammerfest basin. The nomenclature used is taken from Mørk et al. (1999).

2.3.2.1 Triassic

The Sassedalen group comprises rocks of Lower to Middle Triassic and marks the boundary between Permian carbonates and the overlying fine grained clastic sediments of Triassic age (Lundschien et al., 2014). In the Hammerfest basin the Sassedalen group is represented by mainly by thick marine sediments with sporadic more coastal influenced intervals (Mørk et al., 1999).

The Havert-, Klappmyss- and Kobbe formations (Sassendalen group) are all consisting of medium to dark grey shales at the base and passes up to shales interbedded with silt- and sandstones. The Havert- and Klappmyss formations are both interpreted as marginal to open marine facies in the Hammerfest basin. The Kobbe formation has been linked to a transgressive development, followed by a buildout of clastic sediments in the Mid Triassic and has been interpreted as marginal marine facies (Dalland et al., 1988).

The Snadd formation (Kapp Toscana group, Storfjorden subgroup) shows the same coarsening upwards trend seen in the underlying successions. The base is represented by grey shales which develop into shales interbedded with silt- and sandstones (Dalland et al., 1988).

2.3.2.2 Jurassic

The upper part of the Kapp Toscana group is called the Realgrunnen subgroup and comprises rocks from Late Triassic to Mid Jurassic (Figure 2.7). This interval becomes increasingly sandier towards the top and has been linked to the large-scale prograding delta, following the Norian transgression.

The Fruholmen formation consists of dark grey shales at its base, developing into a sand dominated intermediate part while the upper portion is commonly recognized as more shaley. The basal shaley interval has been interpreted as open marine facies, while sandstone is thought to originate from fluviodeltaic progradation and the upper shaley portion has been interpreted as flood plain-deposits. The Tubåen formation is mainly dominated by sandstones which is located at the base and top, while the middle part is more shaley. This interval is thought to originate from shallow marine facies, influenced by high energy regimes related to tidal and/or estuarine facies. The shale dominated intermediate part represents more distal deposits with respect to the prograding delta system. The Nordmela formation consists of siltstones, sandstones, shales and coals and the sandstone intervals becomes increasingly more

common towards the top. This formation was deposited in a near coastal environment influenced by tidal- and flood plain environments (Dalland et al., 1988).

The Upper Mid – Upper Jurassic successions, Fuglen- and Hekkingen formation, are situated within the Adventdalen group and marks a change in the depositional style compared to the underlying interval (Mørk et al., 1999). These formations are commonly found as dark grey organic rich shales with some minor intervals of sandstone.

2.4 Petroleum system

The petroleum system of the SW Barents Sea is a complex system as source – and reservoir rocks are present at various stratigraphic levels, ranging from Late Paleozoic to Cenozoic in age. Both sandstone- and carbonate reservoirs have been recognized in this region, but the most important reservoir intervals are found within the Jurassic sandstone successions. The most important source rocks are located in the shales of Triassic and Upper Jurassic age (Faleide et al., 2015). The Upper Jurassic Hekkingen formation is considered the main source rock both in terms of TOC and remaining petroleum potential, but studies suggest that the petroleum product located in the reservoirs have originated from various source rocks (Ohm et al., 2008).

2.4.1 Uplift – implications on the Petroleum System

Uplift and erosion of the SW Barents Sea area is described in several studies, e.g. (Doré and Jensen, 1996, Dimakis et al., 1998, Ohm et al., 2008, Henriksen et al., 2011, Baig et al., 2016), and they all agree upon that uplifted regions have had a great influence on the petroleum system. Implications mentioned in these studies concerns source rock maturity and migration, reservoir quality, pressure conditions in the reservoir, cap rock failure etc., which may have positive or negative consequences in terms of exploration- and production activity.

In the Snøhvit field, oil staining observed below the present day oil-water contact is believed to result from gas expansion which subsequently led to oil spill from the trap (Nyland et al., 1992). This implies that the cap rock where able to prevent the gas from leaking during uplift. Several discoveries in the Barents Sea have proven to be gas charged often with a thin oil leg. On the contrary, oil discoveries have also been discovered within this uplifted region. The Goliat field, located at the southern basin margin of the Hammerfest basin, is thought to be oil

charged partly due to fractured cap rock. This led to leakage of the gas through the seal, while the oil remained in reservoir (Ohm et al., 2008).

The non-uniform uplift of the greater Barents Sea has also influenced the source rock maturity at various locations. The Hekking formation is for example deeply buried in the Tromsø Basin, whereas in the Hammerfest basin this formation has just reached the oil window. In a broader context, the source rock maturity trends in the Barents Sea compared to the North Sea and Haltenbanken area are very different, where the Barents Sea source rocks shows higher maturities at the same burial depth. This has been related to uplift, where this rocks have, pre-uplift, experienced higher temperatures (Ohm et al., 2008). These means that several source rocks may have been uplifted and exposed to too low temperatures and hence will not be able to effectively produce more petroleum (Henriksen et al., 2011).

In terms of reservoir quality and uplift, the reservoir unit will reflect the maximum burial prior to uplift. By considering a standardized compaction trend in the area, the uplifted reservoir unit will most likely have lower reservoir quality than the other formations located at this depth. On the other hand, quartz cementation may cease if uplifted to a temperature insufficient for dissolution and precipitation of quartz cement and hence may preserve porosity in this particular formation (Doré and Jensen, 1996).

2.5 The Stø formation

The Stø formation is present in large parts of the SW Barents Sea and comprises rocks from late Pliensbachian – Bajocian in age (Dalland et al., 1988). In the Hammerfest basin this unit thickens from east towards west, where the depth to the Stø formation also generally is the greatest (Figure 2.8 and 2.9) (Dalland et al., 1988, Halland et al., 2013).

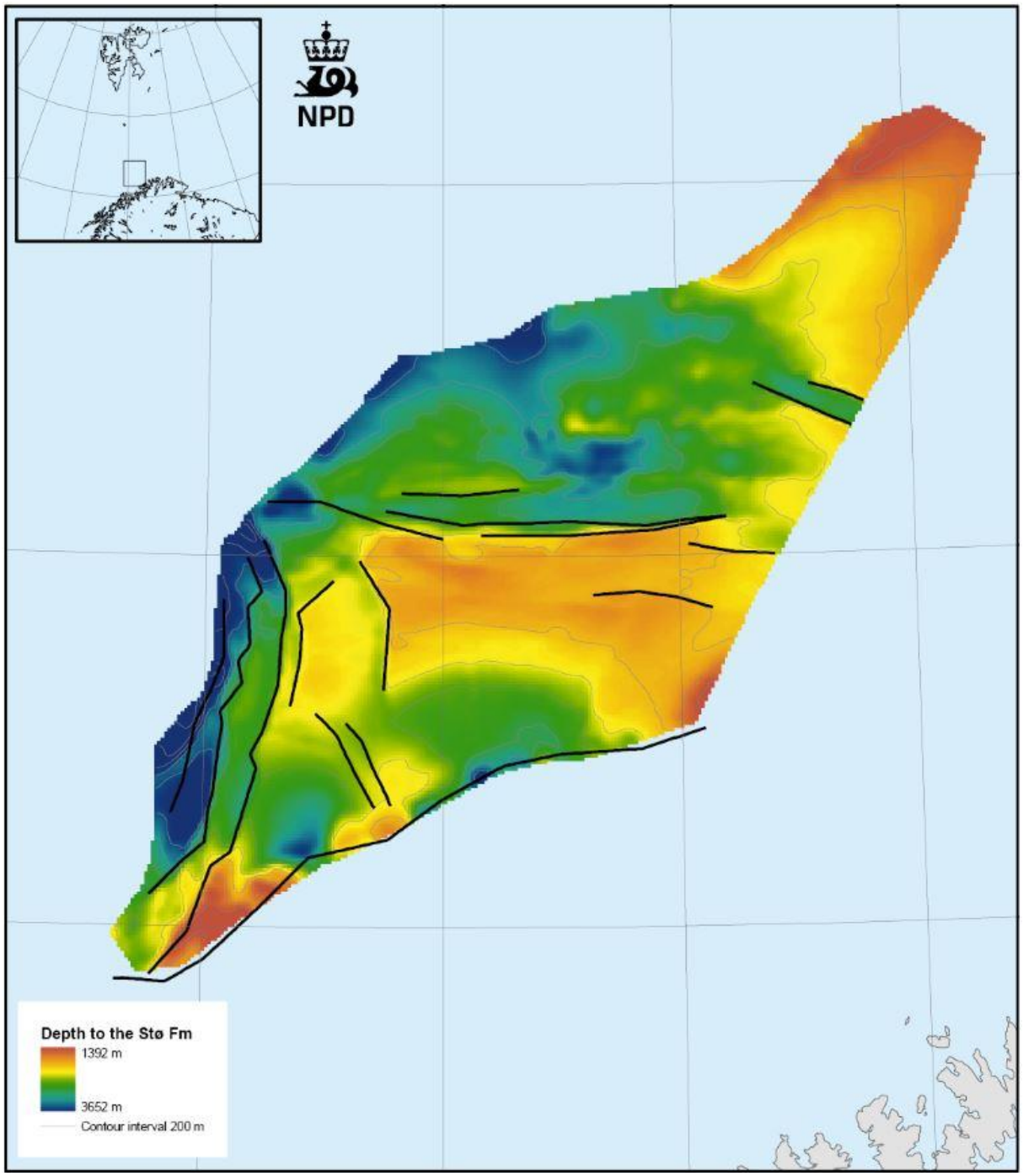

Figure 2.8: The contour map displays the depth to the Stø fromation within the Hammerfest basin. The Stø formation is located at greater depths in the western and northern areas (Halland et al., 2013).

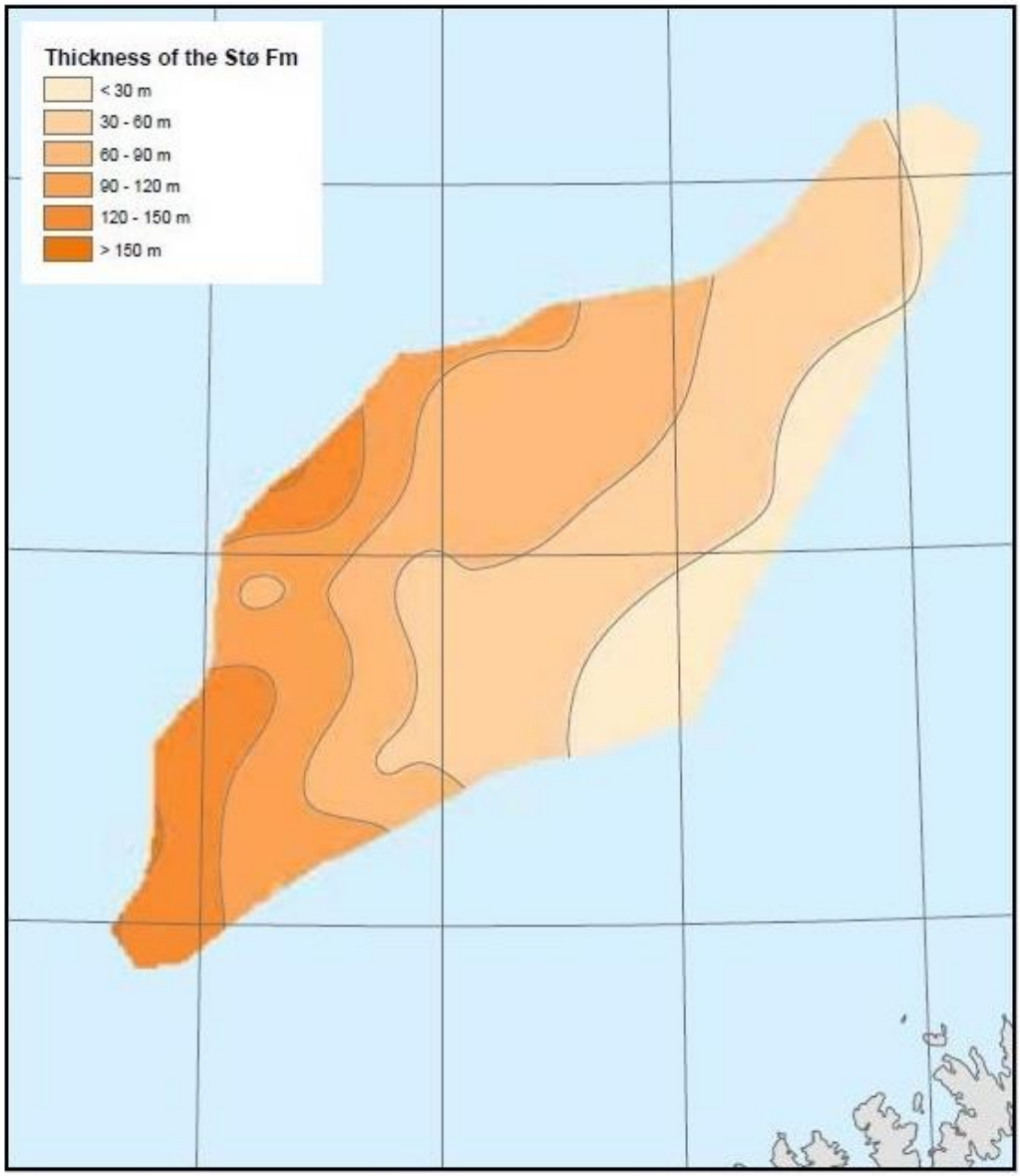

Figure 0.9: Thickness map of the Stø fromation within the Hammerfest basin (Halland et al., 2013).

The basal contact to the underlying Nordmela formation is often recognized as a conglomeratic interval, followed by a thick sequence of sandstone. The lower part of the Stø formation is characterized by fine-to medium grained sandstone, with moderately – to well-sorted intervals. From a mineralogical point of view, the Stø formation is dominated by mature sandstones where feldspar and lithic fragments only makes up a minor fraction of the bulk volume. A fining upwards trend has been recognized towards the uppermost part of the Stø formation, where bioturbation becomes significant and thin mudstones beds occurs more

frequently. In addition, thin pebbly sandstones beds have been recognized within this interval (Berglund et al., 1986).

The Stø formation is a widespread lithology where both facies related to nearshore and more distal marine environments have been identified. More specifically, these sandstones have been linked to foreshore, shoreface, transition/offshore and eustarine sub-environments strongly influenced by wave processes and some tidal effects. The widespread distribution of this unit in the SW Barents Sea has been linked to several minor sea-level changes which resulted in frequent relocation of the nearshore environments (Berglund et al., 1986).

3. Theoretical background

3.1 Introduction

This chapter focuses on theoretical concepts applied in this study. Initial sediment properties prior to diagenesis, i.e. textural properties and mineralogical composition at the time of deposition, are of great importance for the resultant reservoir quality. These properties are controlled by the provenance, transport mechanisms and depositional setting which will be shortly described in the following. Next section will concern diagenesis and will describe how sandy sediments are affected by an increase in stress and temperature, as the rock is buried to greater depths. Several mechanisms may prevent porosity loss in sedimentary rocks during diagenesis and will be included at the end of this chapter.

3.2 The origin of siliciclastic sediments and the importance for the reservoir quality

Siliciclastic sediments can be defined as sediments with a composition consisting mostly of silicate minerals which have been eroded from pre-existing igneous, metamorphic or sedimentary rocks (James and Dalrymple, 2010). The type of source rock (source area) being eroded determines the composition of the sediments of which is to be transported to a depositional site (Bjørlykke, 2015). During transportation, a progressive loss of unstable minerals with respect to the transport-distance and the degree of weathering alters the sediment composition. Quartz is considered a more stable mineral than for example feldspar and hence an increased quartz/feldspar ratio may be related to greater transport-distances. Grain shape- and sorting will also be altered during transportation, where feldspar is more readily rounded than quartz grains (Boggs, 2011). Climatic conditions are also controlling the weathering and transportation rates, as for example a more humid climate will subsequently control the water discharge to rivers which will affect the transportation rates. As sediments reach the site of deposition, the depositional system (facies) will influence both the microscopic- and macroscopic characteristics of the sediments. The grain size and sorting of the sediments deposited will be controlled by the flow regime within each particular depositional system which controls if the sediments will be transported further or deposited. The type of depositional system will also influence the geometrical appearance of the sediment bodies which will give rise to different types of reservoir both with respect to shape and size.

As described above, the mineralogical- and textural properties prior to diagenesis are a function of weathering (source areas), transport mechanisms and depositional setting. Therefore, it is important to understand these processes as they determine sediment properties prior to diagenesis which subsequently will control the reservoir quality at greater depths.

3.3 Diagenesis

Diagenesis involves all the processes related to burial of a given rock. As a rock unit is buried to greater depths an increase in stress and temperature causes the rock to compact, and this is generally associated with porosity loss (Bjørlykke and Jahren, 2012) (Figure 3.1). The compaction process is also a function of the initial bulk composition of the rock, which may be altered by various process at shallow depths (1-10m). It is therefore important to understand the initial sediment composition prior to diagenesis to be able to predict reservoir quality (Bjørlykke, 2014). This also implies that compaction curves may vary greatly according to location and geological evolution of a given area. In the following, three stages of diagenesis will be presented with examples of processes related shallow burial, mechanical- and chemical compaction for quartz-rich sandstones.

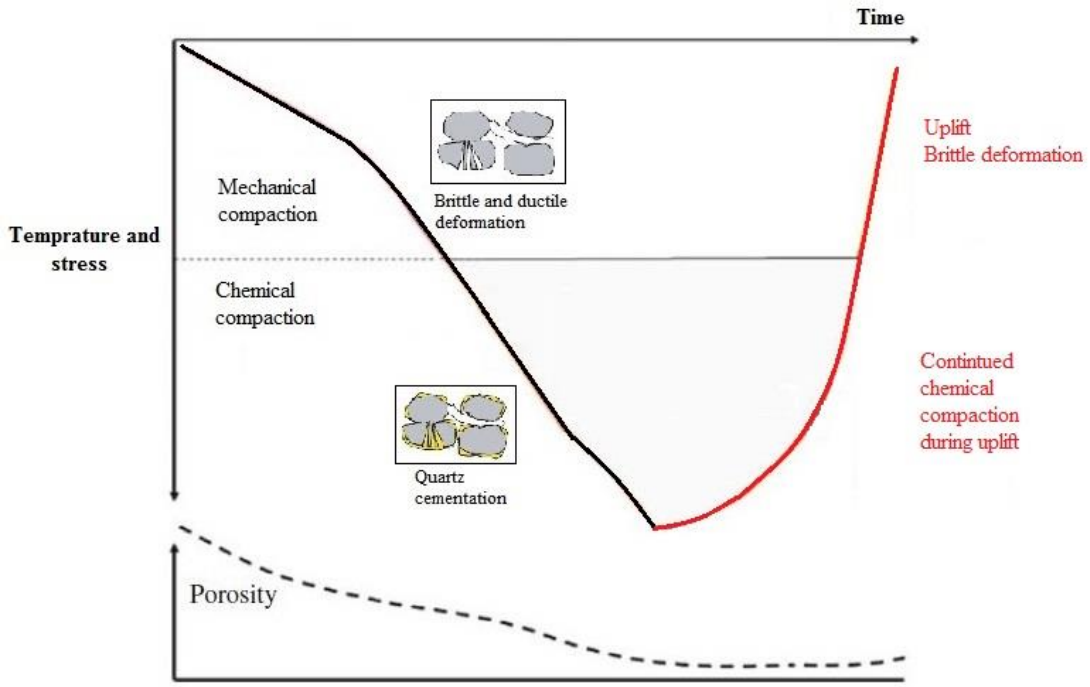

Figure 3.1: The figure displays a general overview of the main processes acting during diagenesis. A porosity loss is general associated with an increase in burial depth. Modified from (Bjørlykke and Jahren, 2015).

3.3.1 Shallow burial

Sediments close to the surface (~1-10m) are more likely to react with meteoric water and the atmosphere. Hence, the bulk composition of the sediments may change significantly during the early stage of burial. Dissolved solids are either transported by diffusion or fluid flow and are commonly most effective within the uppermost few meters of the subsurface. Meteoric water is often under-saturated (distilled water) with respect to all minerals and leaching of unstable minerals like feldspar and mica may result in precipitation of kaolinite as shown in the reactions below (Bjørlykke and Jahren, 2012):

Feldspar → Kaolinite + dissolved silica and cations:

$$2K(Na)AlSi_3O_8 + 2H^+ + 9H_2O = Al_2Si_2O_5(OH)_4 + 4H_4SiO_4 + 2K^+(2Na^+)$$

Muscovite → Kaolinite + dissolved cations:

$$2KAl_3Si_3O_{10}(OH)_2 + 2H^+ + 3H_2O = 3Al_2Si_2O_5(OH)_4 + 2K^+$$

These reaction rates are controlled by the supply of meteoric water as the water is under-saturated with respect to Na^+, K^+ and silica, and depends on the removal of the dissolved products. Hence, these processes are restricted to areas where permeable beds favor a constant flow of meteoric water. Rainwater is slightly acidic due to interaction with carbon dioxide (CO_2) and sulphur dioxide (SO2) in the atmosphere which may favor precipitation of kaolinite because of the low K^+/H^+ ratio (Bjørlykke and Jahren, 2012). In addition, removal of dissolved silica is important to obtain precipitation of kaolinite, as too high silica concentrations will result in precipitation of smectite as the kaolinite is no longer stable under these conditions.

Biogenic activity is another important process which influences the textural composition of the sediments. Burrowing organisms reorganizes the primary grain configuration, by for example mixing sand and clay, which may reduce the permeability and porosity. In other cases, organisms will destroy thin clay layers within the deposits and hence increase the vertical permeability. Decay of organic matter may also contribute to increase the acidity of the groundwater due to elevated carbon dioxide concentrations (Bjørlykke and Jahren, 2015).

Carbonate cementation in sandstones may also form close to the surface if sufficient amounts of carbonate ions (CO_3^{2-}) is present. In addition, in order to precipitate calcite ($CaCO_3$), dolomite($Ca,Mg(CO_3)_2$) or siderite ($FeCO_3$), cations such as Ca^{2+}, Mg^{2+} and Fe^{2+} most be dissolved from non-carbonate minerals (Saigal and Bjørlykke, 1987). The carbonate ions are in most cases sourced from biogenic carbonate and typically from organisms composed of aragonite, as leaching of e.g. plagioclase are in most cases not producing sufficient amounts of Ca^{2+}. Hence, the degree of carbonate cementation can be related to types of depositional environments which favor accumulations of biogenic organisms (Bjørlykke and Jahren, 2015).

3.3.2 Mechanical compaction

Mechanical compaction is a function of the effective stress mainly caused by the weight of overburden and the compressibility of the rock frame (Chuhan et al., 2002, Bjørlykke and Jahren, 2012). This process includes sliding, crushing, reorientation and repacking of the sediment grains, and accounts for the greatest porosity-reducing mechanism for sandstones during the first 2-3 km of burial (Lundegard, 1992, Paxton et al., 2002, Bjørlykke and Jahren, 2015). Porosity may be reduced from critical porosity, which is commonly 40-42% for sandstones, to 35 -25% at stresses of 20-30MPa depending on the physical behavior of sediments (Chuhan et al., 2002, Paxton et al., 2002).

The depths at which mechanical compaction is most effective varies accordingly to the geothermal gradient in the area, which controls the chemically driven processes in addition to time. At temperatures above 70 – 80°C, quartz cementation may cause the rock frame to strengthen and prevent further mechanical compaction(Bjørlykke and Jahren, 2012). Assuming a geothermal gradient of 30°C/km and stress gradient of 10 MPa/km, the interval of mechanical compaction will act to depth and stress levels of about 2-3 km and 20-30 MPa, respectively.

The degree of mechanical compaction is also a function of the sediment sorting, as the grain size controls the number of grain contacts. Generally, a fine-grained sand will allocate the effective stress to a larger number of contact points in comparison to a coarse-grained sand, which will experience a higher force at each contact point. This may cause a coarse-grained sandstone to compact more than a fine-grained sand (Figure 3.2). In addition, grain shape and the actual area of the contact surface will play a role in terms of stress at a given grain contact.

Hence, the porosity loss in a fine grained sandstone is associated with grain sliding and reorientation, while grain crushing act as the main porosity reducing mechanism in a coarse grained sand (Chuhan et al., 2002).

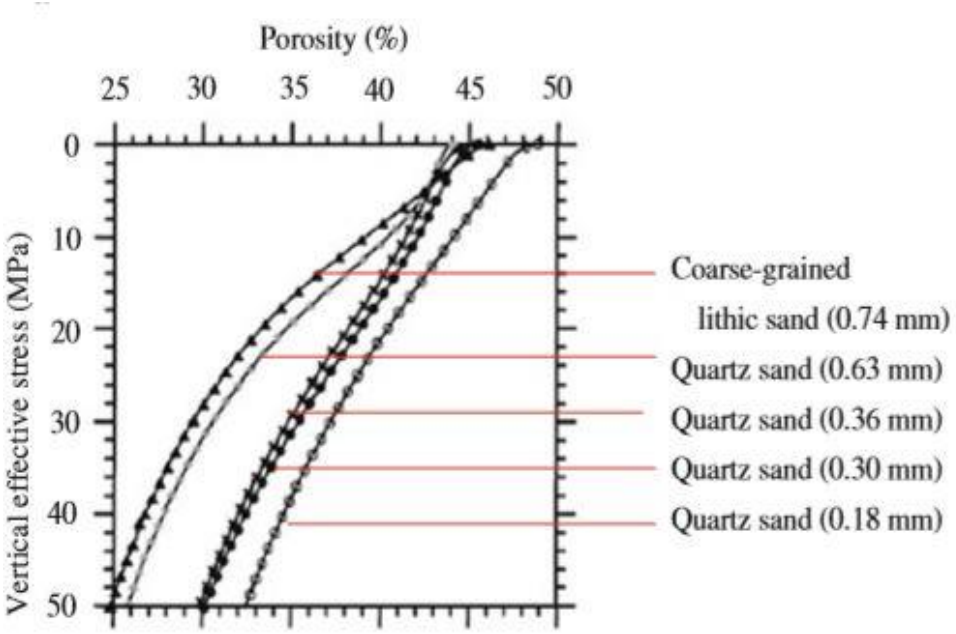

Figure 3.2: Shows the effect of grain size as a function of stress and porosity loss. Coarser grained sand compacts more readily than sands with a smaller grain size. After (Chuhan et al., 2002), taken from (Bjørlykke and Jahren, 2015).

The mineralogical composition will also influence the degree of mechanical compaction (porosity loss), as different minerals and mineral assemblages will yield very different physical behavior when exposed to increased pressure and temperature. Compaction experiments by Pittman and Larese (1991) studied compaction of sandstones related to the amount and type of lithic fragments present. Sedimentary lithic fragments are often considered more ductile than metamorphic fragments, while volcanic lithic fragments may be very ductile, when altered to sheet scilicates during erosion or diagenesis (Pittman and Larese, 1991). This study looked at a relation between the amount of soft minerals (clay, mica) and hard minerals (quartz and feldspar) and the degree of ductile deformation during mechanical compaction. For low ratios of soft-hard minerals indicates that the porosity loss is less than samples composed of mainly soft minerals. The type of lithic fragments also seemed to

control the compaction trends, where the most ductile lithic material resulted in greater porosity loss (Pittman and Larese, 1991).

3.3.3 Chemical compaction

Chemical compaction involves dissolution and precipitation of minerals and is the main porosity reducing mechanism at greater depths. This process is insensitive to stresses, in contrast to mechanical compaction. The depth at which chemical compaction will start to dominate is controlled by the temperature which subsequently controls the silicate reactions in siliceous sediments (Bjørlykke and Jahren, 2012). At temperatures above 75 - 80°C quartz cementation may start to precipitate (Walderhaug, 1994) and only small amounts of cement can cause the rock frame to strengthen and prevent further mechanical compaction (Bjørlykke and Jahren, 2012). Quartz cementation is a common diagenetic mineral in quartz rich sandstones during deeper burial and will be further discussed in the following (Walderhaug, 1994).

3.3.3.1 Quartz cementation

At the boundary between mechanical- and chemical compaction, at a depth of about 2-3km, most quartzarenites have been mechanically compacted and commonly displays an intergranular porosity in the range of 25 – 30%. A further porosity loss is caused by quartz overgrowth on available detrital quartz surfaces. The cementation processes can be divided into three steps regarding dissolution (source), transportation and precipitation of silica (Bjørkum et al., 2001).

Dissolved silica is most likely sourced from stylolites or at grain contacts between clay or mica (Walderhaug, 1994). Transportation of dissolved silica by diffusion is integrated in several existing cementation models and is thought to be responsible for distribution of the dissolved silica within the formation water (Figure 3.3) (Bjorlykke, 1993, Walderhaug, 1994, Walderhaug, 1996).

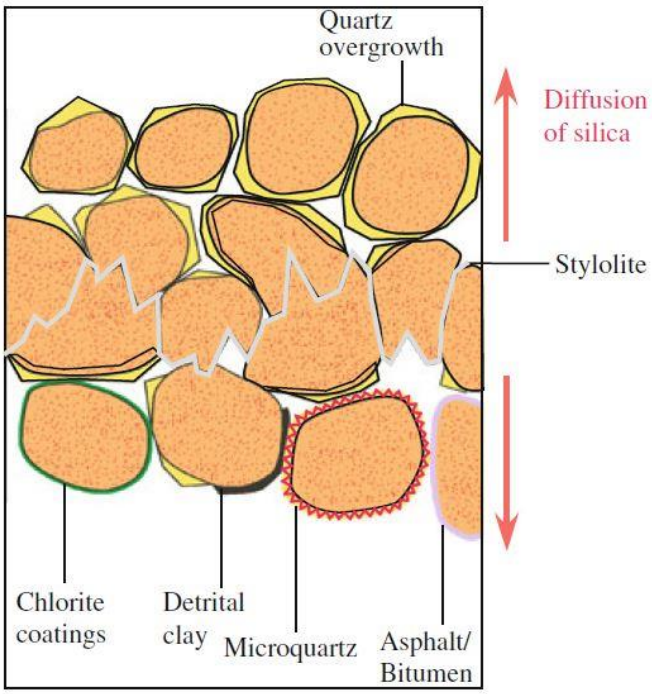

Figure 3.3: A conceptual representation of a stylolite. The dissolved silica is transported by diffusion and may precipitate at available detrital quartz grains. Picture taken from (Bjørlykke and Jahren, 2015)

Precipitation is mainly controlled by the available detrital- and overgrowth quartz grain surfaces and seems to be the rate limiting step for this reaction. A fine grained sandstone will have more surface area available for quartz cementation than a coarse grained sandstone, and hence may be more heavily cemented. On the other hand, some studies have shown that coarser grained sandstones cements more readily e.g. (McBride, 1989). The rate of quartz cementation has been discussed by several authors over the years. Later work (Walderhaug, 1994, Walderhaug, 1996) has pointed out that the rate limiting step may not be quartz dissolution or transportation of dissolved silica, but rather the rate of crystal growth (Lander et al., 2008). This was supported by the degree of quartz cementation detected between stylolites, where no obvious increase in amount of cement were observed closer to the stylolite; regions where dissolved silica concentrations were higher due to short-distance diffusion (Walderhaug, 1996). However, intervals with particularly large stylolite spacing, i.e. styliolite spacing in the range of meters, have showed that quartz cement volume may be significantly lower (Walderhaug et al., 2003).

As the rate limiting step is thought to be the precipitation rate of quartz, temperature is an important parameter to consider in any chemical reaction. Walderhaug (1996) simulated quartz cementation by testing three different temperature histories for a sandstone with equal textural and mineralogical properties with the aim to describe the effect of temperature variations. This simulation showed that the sandstone exposed to a continuous temperature increase during a period of 45 m.y. had been totally cemented, while the other two sandstones had been heated up to 120°C and 100°C and showed a porosity of 15.4% and 8.4%, respectively. All the samples had been heated up by 2°C/m.y. Although this model assumes that saturation levels are constantly sufficient for quartz precipitation in all the space between stylolites, the effect of temperature on precipitation rates is fairly obvious (Figure 3.4). The sandstone exposed to a constant temperature increase and the highest temperature, becomes totally cemented.

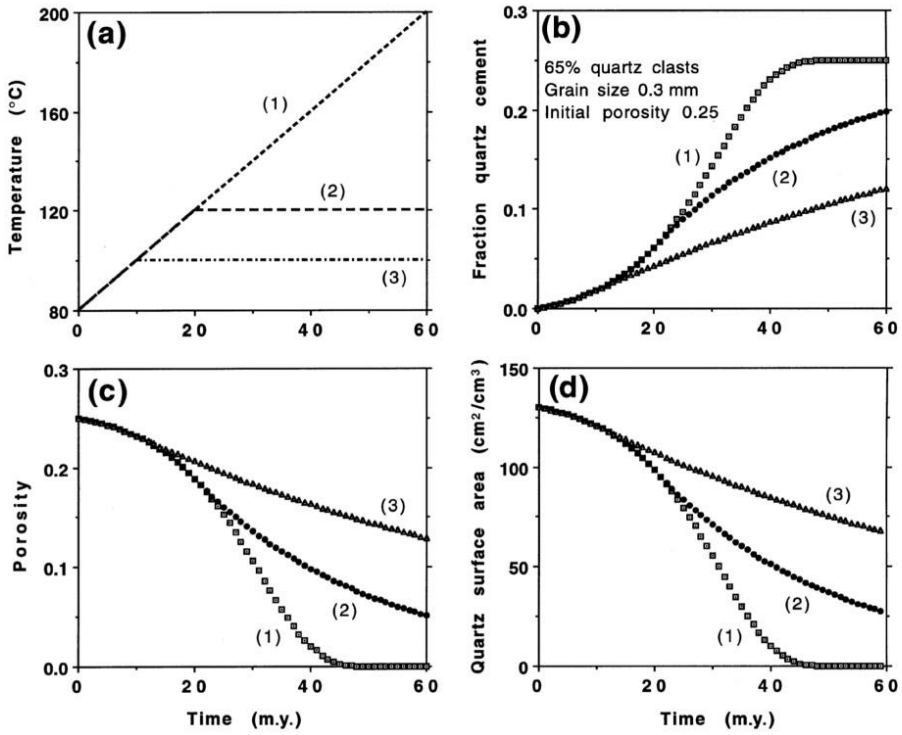

Figure 3.4: The figure displays the effect of temeprature as a function of time for three sandstones of similar mineralogical and textural properties. (a) temperature history for the sandstones (b) fraction of quartz cement, (c) porsity and (d) quartz surface area (Walderhaug, 1996).

The effect of quartz cementation causes the rock to compact at temperatures above 75-80°C, i.e. reducing porosity and increasing the density which results in a thinning of the rock-column. This process is partly responsible for creating accommodation space for sediments at the surface (subsidence), resulting in a cycle where sediments are constantly altered by new compaction processes acting at a specific depth. In figure 3.5, three scenarios where a sandstone with an initial thickness of 100 meter is exposed to different temperatures at a constant rate as a function of time can be seen. Higher temperatures cause the sandstone to be thinned at a higher rate due to more precipitated quartz cement (Walderhaug et al., 2001).

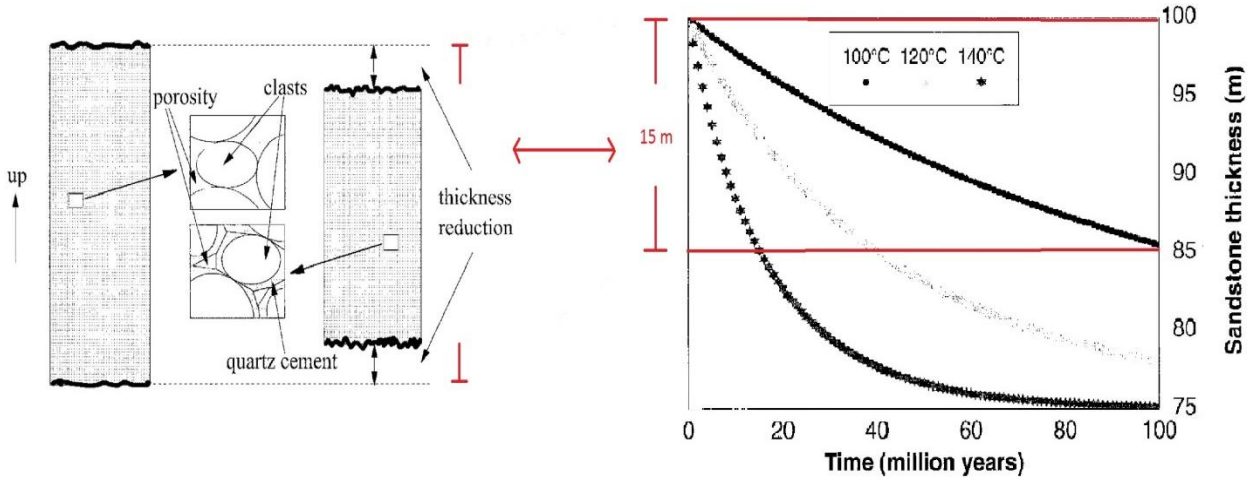

Figure 3.5: (left): a conceptual illustration of lithology-thinning, caused by the quartz cemntation. (right): a thinning experiment, where a sandstone exposed 100°C where thinned 15 meters in 100 m.y.. Modified from (Walderhaug et al., 2001)

Quartz cementation is most common processes involved in the chemical compaction window when dealing with quartz rich sandstones. However, other porosity reducing mechanisms may influence the sediments during this interval.

3.3.3.2 Authigenic clays

Authigenic clays can be referred to as the clay fraction that has been formed or regenerated, in place, during diagenesis. The authigenic clay minerals are thought to either precipitate directly from the formation waters or react with precursor materials within the sediment. Commonly, these clays can be recognized as pore linings, pseudomorphous replacements, pore fillings or fracture fillings (Figure 3.6) (Wilson and Pittman, 1977).

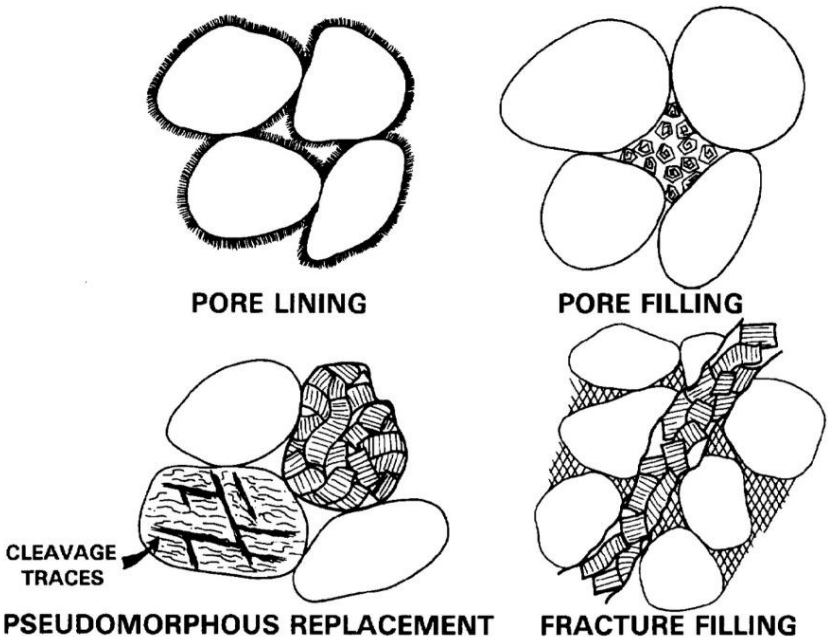

Figure 3.6: Different types of authigenic clays commonly recognized as matrix in sandstones (Wilson and Pittman, 1977).

In terms of reservoir quality, authigenic clays play an important role as only small amounts of such clays may alter the reservoir properties greatly. Pore linings may reduce permeability as the precipitated authigenic clay reduces pore throats volume and hence restrict fluid flow within the reservoir. In addition, the water saturation may increase in cases where significant amounts of authigenic clays are present because of water occupying micropores in the matrix (Wilson and Pittman, 1977). Precipitation of authigenic clay, associated with dissolution of detrital grains, is thought to be less important regarding enhanced porosity, as the net porosity gained is commonly very low (<0,25%) (Yuan et al., 2015).

3.3.3.3 Illitization

Illitization is another common chemical process which may become important at temperatures above 130°C, where K-feldspar and kaolinite is no longer stable together, which results in precipitation of illite. A simplified version of this reaction can be written as (Chuhan et al., 2000):

K-Feldspar + Kaolinite = Illite + Quartz

$$KAlSi_3O_8 + Al_2Si_2O_5(OH)_4 = KAl_3Si_3O_{10}(OH)_2 + 2SiO_2 + H_2O$$

In order to form illite, potassium most be available. The potassium is often sourced from the K-feldspar as this is considered the main potassium source in most sandstones. (Chuhan et al., 2000), recognized a relation between loss of K-feldspar and kaolin (kaolinite and dickite) associated with a sharp increase in Illite at a depth of 3.6 – 3.7 km (120-140°C) from mineralogical- and geochemical data obtained from the Haltenbanken area. Further, they argued that no change in the K/Al ratio at various depths indicated that this processes acted in a closed system i.e. no external potassium source. In the same study, data from the northern Viking Graben where only small amounts of K-Feldspar where present, contained almost no illite. A ratio between K-feldspar/kaolinite greater or equal to 1 is most likely to precipitate significant amounts of illite (Chuhan et al., 2000).

Another study regarding clay transformation during burial, shows that illitization from smectite start at lower temperatures (Dypvik, 1983). An increase in relative amount of pure illite and mixed layer clays where observed as a function of increasing temperatures, and at temperatures above 80-100°C illitic layers accounted for more than 70 % of the clay volume (Dypvik, 1983). The smectite may start to dissolve at temperatures of 65-75°C, which results in precipitation of illite (Bjørlykke, 1998). A release of substantial amounts of silica has been associated with the transformation of smectite to illite (Bjørlykke, 1998), where precipitation of quartz cement facilitates the smectite-illite reaction to proceed (Peltonen et al., 2009). A simplified version of the reaction can be seen below (Peltonen et al., 2009):

$$\text{Smectite} + K^+ \rightarrow \text{Illite} + SiO_2 + H_2O.$$

3.3.3.4 Albitization

(Saigal et al., 1988) suggested that albitization from K-feldspar may have occurred in situ within various reservoir sandstones from offshore Norway during diagenesis. Direct transformation of K-feldspar to albite can be described as the reaction below, where removal of potassium and supply of sodium are required for the reaction to proceed (Saigal et al., 1988):

$$KAlSi_3O_8 + Na^+ \rightarrow NaAlSi_3 + K^+.$$

Based on the petrographic results, Saigal et al. (1988) suggested that albitization from feldspar occurred between a depth of 2.2 – 3.4 km, corresponding to a temperature interval of 65 – 105˚C assuming a geothermal gradient of 30˚C/km; where a complete pseudomorphic albitization was restricted to the higher temperature intervals.

3.4 Porosity preserving mechanisms

Diagenesis is in general related to processes that cause the sediments to compact, i.e. an increase in density of the lithologies and decrease in the porosity as discussed above. However, some diagentical processes may prevent porosity loss which can benefit reservoir properties such as porosity and permeability and even make deeply buried reservoirs economical interesting. In the following porosity preserving mechanisms will be introduced.

3.4.1 Grain coats and grain rims

The term grain coats refer to a thin layer of a mineral, in most cases clay or microcrystalline quartz, which cover the surface of the detrital grains and is a result of processes acting subsequent to burial. Grain rims is often used to describe clay coats which were present prior to burial. Both grain coats and grain rims have proven to prevent quartz cementation and hence preserve porosity (Bloch et al., 2002). Authigenic coatings are more effective in preventing quartz cementation than detrital clay rims because they are often more continuous, i.e. covering all the surface area available for quartz cementation (Bloch et al., 2002). Other types of cement, e.g. carbonates, will continue to precipitate regardless of coating and hence influence the reservoir quality (Pittman et al., 1992).

3.4.2 Fluid overpressure

As discussed, sediment loading increases the vertical effective stress and causes the rock to be physically compacted. Fluid overpressure can be defined as the excess fluid pressure at given depth greater than the hydrostatic pressure (Bloch et al., 2002). Mechanisms causing development of overpressure can be divided into three categories: (1) a rapid reduction of pore volume compared to fluid release, (2) where fluid expansion occurs at a greater rate than fluid release and (3) processes related to large scale fluid movements (Osborne and Swarbrick, 1997, Bloch et al., 2002). All processes related to development of overpressure requires regions with impermeable zones where fluids are refused to equalize the pressure differences. In cases where fluid overpressure is developed within a formation, the effective stress at each grain contact will be reduced. Hence, in terms of porosity preservation, fluid overpressure is most important during the mechanical compaction stage (Bloch et al., 2002).

3.5 Reservoir quality

A reservoir quality prediction aims to better understand the relation between important reservoir parameters, such as porosity and permeability, and depth (compaction) in an area. Available remote sensing techniques are not jet capable to predict these parameters accurately and hence, reservoir quality predictions becomes an important element in risk analysis (Ajdukiewicz and Lander, 2010). Reservoir quality predictions becomes increasingly more important to consider as the potentially reservoir rock has been exposed to higher temperatures (> 100 °C) and/or significant effective stresses (Taylor et al., 2010). As the porosity reflects the total hydrocarbon storage capability of a given reservoir rock, it is important to describe this parameter in detail. Porosity is function of sandstone composition, textures and processes related diagenesis and will be an integral part of this thesis.

4. Methods and data

4.1 Introduction

The methods and data utilized in this thesis will be presented in this chapter. First, a short description of the data available for this study will be given. Further, methods used to obtain results from both petrographic and petrophysical analysis will be presented. A short discussion of the uncertainties related to this study will be presented at the end of each approach.

4.2 Database

The results obtained in this thesis are based on data from geophysical well logs (7121/5-1 and 7120/6-1) and thin section samples from the same wells, acquired from various depths within the Stø formation. Figure 4.1 displays all the thin sections and from which depth they were obtained and the same information is showed in table 4.1. The thin section names presented in table 4.1 and figure 4.1 will be used in this thesis, where sample 1 to 8 are from well 7121/5-1 and 9 to 20 are obtained from well 7120/6-1. The sample depth increases from thin section 1 to 8 and 9 to 20 in both wells separately. The Stø formation was dived into four different sequences based on the petrophysical- and the petrographic analysis. These sequences will be referred to when presenting data in a broader context (figure 4.1 and table 4.1). In well 7121/5-1, sequence A1 and A2 encompasses thin section 1 to 5 and 6 to 8, respectively, whereas in well 7120/6-1 sequence B1 includes thin section 9 to 16 and sequence B2 includes thin section 17 to 20. The general well information, regarding the geophysical well logs are summarized in table 2, which is taken from the (NPD, 2016). The available well logs in the two wells are presented in table 3. All the data were made available by the University of Oslo, as they are an associate member of the Diskos group.

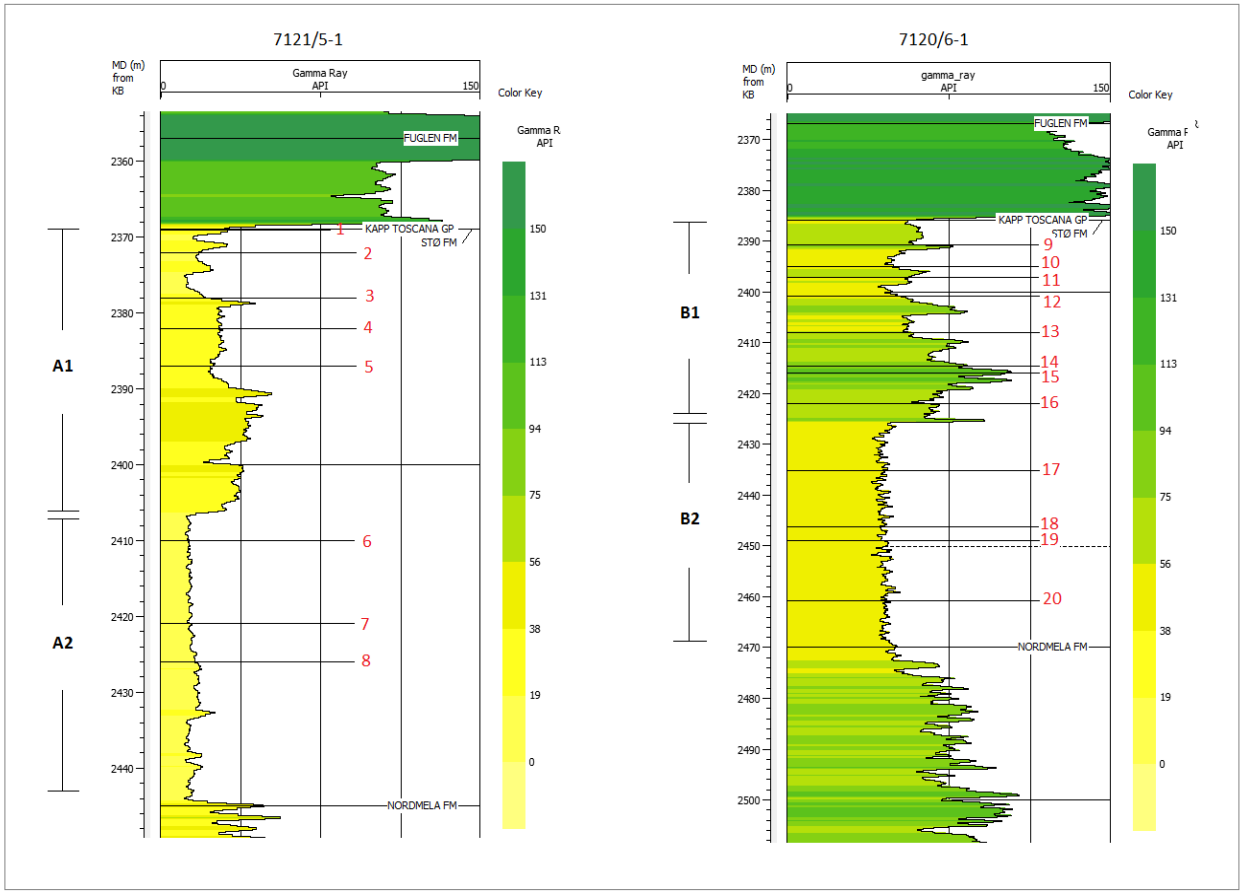

Figure 4.1 The figure displays the location of the thin section within the Stø formation in both wells. The depth of where the thin sections where obtained increases from 1-8 and 9-20 in both wells separately. Based on petrographic and petrophysical analysis the Stø formation was dived in to two sequences in each well. The figure shows which thin section that belongs to each sequence.

Table 4.1: The table summarizes figure 4.1, regarding the depth of the thin sections and which thin section that belongs to each sequence.

Well name	Thin section name	Sequence	Depth (KB) [m]
7121/5-1	1		2368
7121/5-1	2		2372
7121/5-1	3	A1	2378
7121/5-1	4		2382
7121/5-1	5		2387
7121/5-1	6		2410
7121/5-1	7	A2	2421
7121/5-1	8		2426
7120/6-1	9		2391
7120/6-1	10		2395
7120/6-1	11		2397
7120/6-1	12	B1	2400
7120/6-1	13		2408
7120/6-1	14		2415
7120/6-1	15		2416
7120/6-1	16		2422
7120/6-1	17		2435
7120/6-1	18	B2	2446
7120/6-1	19		2449
7120/6-1	20		2461

Table 4.2: The table summarizes general well information regarding well 7121/5-1 and 7120/6-1. The information is taken from (NPD, 2016).

Well name	7121/5-1	7120/6-1
Location	71° 35' 54.88" N 21° 24' 21.78" E	71° 37' 11.76" N 20° 55' 59.72" E
Well type	EXPLORATION	EXPLORATION
Completed date	28.09.1985	02.05.1985
Content	OIL/GAS	OIL/GAS
Water depth [m]	336.0	314.0
Kelly bushing elevation [m]	22.0	23.0
Total depth (MD)[m RKB]	3200.0	2820.0
Final vertical depth (TVD) [m RKB]	3197.0	2820.0
Stø formation [m RKB]	2369 - 2445	2386 - 2470
Maximum inclination [°]	4.75	3.8
Bottom hole temperature [°C]	115	104

Table 4.3: The table displays the available well logs in well 7121/5-1 and 7120/6-1.

Well name	7121/5-1	7120/6-1
Caliper	Yes	Yes
SP	No	No
GR	Yes	Yes
Density	Yes	Yes
Sonic log (P-wave/S-wave)	Yes/No	Yes/No
Bit size	No	No
Shallow Resistivity	Yes	Yes
Medium Resistivity	Yes	Yes
Deep Resistivity	Yes	Yes
Neutron Porosity	Yes	Yes

4.3 Petrographic analyses

The main goals of the petrographical analysis was to estimate the mineralogical distribution in each sample, describe textural properties (i.e. grain shape and size and grain contacts) and determine amounts of pore space, cement and authigenic matrix present. This was achieved by utilizing an optical microscope and a scanning electron microscope (SEM). These results will form the basis for calculation of the Intragranular volume (IGV) and a discussion related to the petrophysical analysis in order to describe the reservoir quality adequately.

4.3.1 Optical microcopy

All of the 20 thin sections were examined using a Nikon optical microscope and a point counting machine. 400 points in each sample were counted which was considered representative for the whole sample. Please note that thin section 1 was damaged during preparation and hence this sample represents only 150 data-points. Different types of detrital grains, matrix, cement, pore spaces etc. were identified and the results formed the basis for a mineralogical distribution in each thin section.

4.3.1.1 Mineralogy

The various samples can be plotted in a four-component diagram which is a classification chart from Dott (1964) figure 4.2. In this classification, sedimentary rocks are classified according to their framework mineralogy and amount of matrix (grains < 0,03 mm). The four-component diagram is commonly used to separate between amount of matrix, quartz, feldspar and rock fragment contents. Sandstones with a matrix percentage less than 15% are called arenites and further, rocks with a detrital quartz content of more than 95 % is called Quartz arenite (Bjørlykke and Jahren, 2015). All the samples considered in this study reveals a quartz content greater than 95 % and a matrix content less than 15%, hence it is meaningless to plot these data in such a diagram. The presentation of the results from the point count will focus on the relative amount of porosity, cement and matrix.

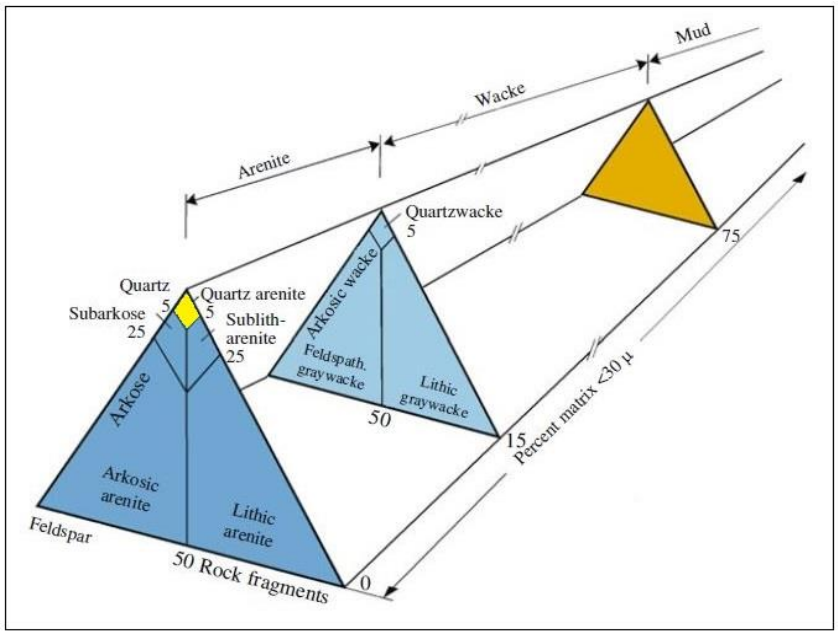

Figure 4.2: The figure displays the classification chart for sandstones from (Dott, 1964). The figure is taken from (Bjørlykke and Jahren, 2015)

4.3.1.2 Textural properties

100 randomly picked grains in each sample where examined during the optical microscopy analysis in terms of grain shape and grain contact. The criteria used to identify various grain shapes and contacts are presented in figure 4.3 and 4.4, respectivley. Grain shape characterization involved both the angularity and sphericity of each particular grain and were quantified according to the chart presented by Powers (1953). Due to the monomineralic appearance of the Stø formation in the samples these analysis was entirely based on characterization of quartz grains. The result obtained from these analyses was plotted in Excel and presented in a broader context, i.e. as sequences (see table 4.1 and figure 4.1).

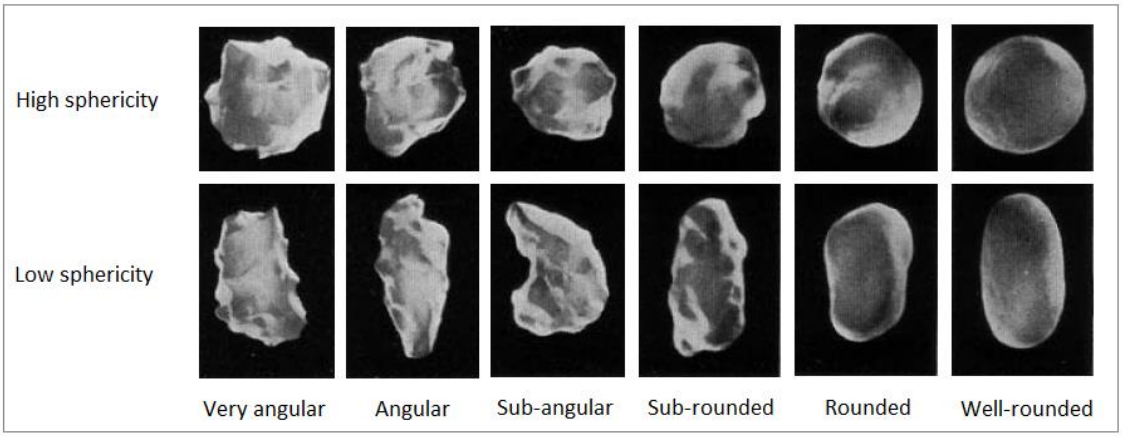

Figure 4.3: The figure displays the chart used to determine the angularity and sphericity of the detrital grains examined in optical microscope. Modified from (Powers, 1953).

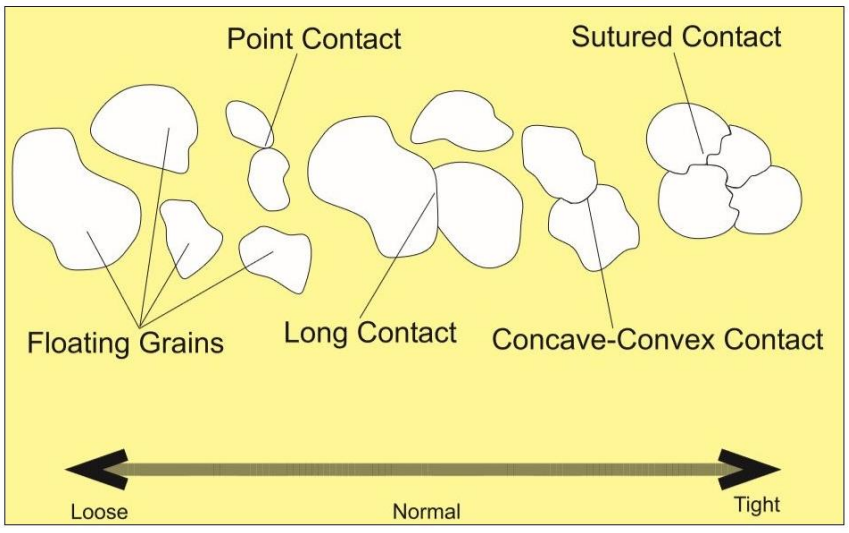

Figure 4.4: The figure displays the various grain contacts that have been recognized in the optical microscope analysis from (Santin et al., 2009).

Grain size estimates were obtained by measuring the longest grain-axis from 100 grains in each sample. This was achieved by using a microscope with a camera and accompanying photographing software. These data were exported to excel and converted to the Phi scale and plotted in a cumulative frequency plot in order to examine the grain size distribution and calculate statistical parameters such as sorting and skewness.

Sorting is a measure of the variety of grain sizes and the spread of these grain sizes within the sample examined, whereas the skewness describes the sorting of the "tail" of a non-normal grain size population (Boggs, 2011). The verbal terms used to describe skewness is obtained after Folk (1974) (table 4.4) which separates between fine or coarse skewed distributions. A fine skewed population means that the sample has a tail with additional fine grained particles in comparison to a normal distribution (Boggs, 2011). Sorting was calculated from the inclusive graphic standard deviation formula (Eq. 4.1) and skewness was calculated from the inclusive graphic skewness formula (Eq. 4.2). The verbal terms used for sorting is obtained from Folk (1974) (table 4.4).

Eq. 4.1 $$\sigma = \frac{\emptyset_{84} - \emptyset_{16}}{4} + \frac{\emptyset_{95} - \emptyset_{5}}{6.6}$$, (Boggs, 2011).

Eq. 4.2 $$SK_t = \frac{(\emptyset_{84} + \emptyset_{16} - 2*\emptyset_{50})}{2(\emptyset_{84} - \emptyset_{16})} + \frac{(\emptyset_{95} + \emptyset_{5} - 2*\emptyset_{50})}{2(\emptyset_{95} - \emptyset_{5})}$$, (Boggs, 2011).

Figure 4.5 displays an example of a grain size distribution where the Phi-scale is plotted against the cumulative frequency. In order to calculate sorting and skewness the 5th, 16th, 50th, 84th and 95th percentile values were calculated and inserted to the formulas above.

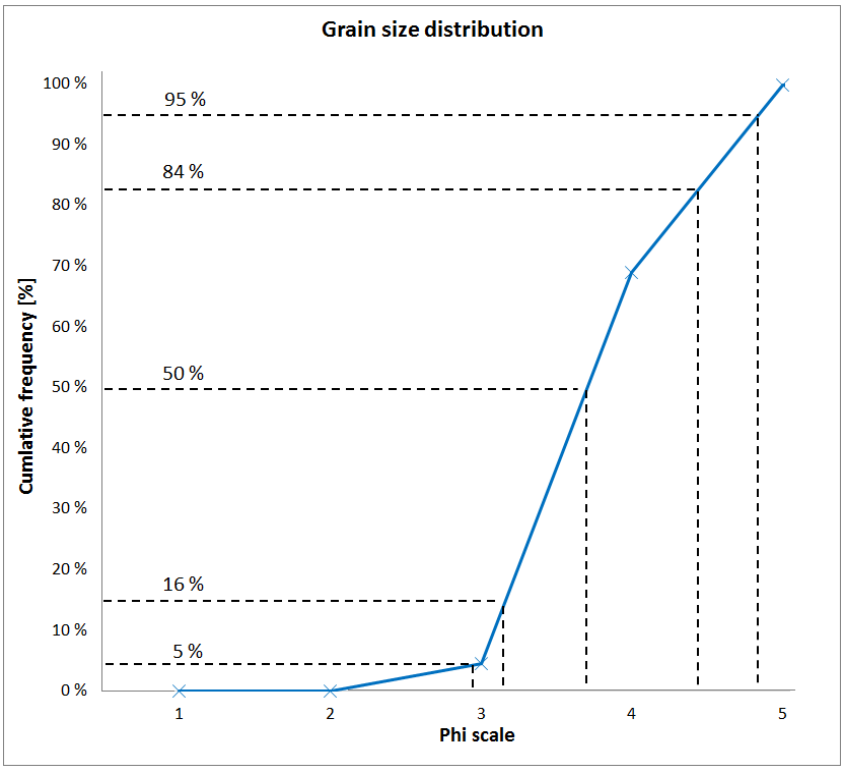

Figure 4.5: Shows an illustrative example of how the phi values where obtained. The percentiles were calculated in excel.

Table 4.4: The table displays the verbal terms used in this thisis to describe a spesific interval in phi values regarding the degree of sorting and skewness.

Sorting - Inclusive standard deviation		Skewness - Inclusive graphic skewness	
Phi standard deviation	Verbal terms after Folk(1974)	Calculated skewness	Verbal terms after Folk (1974)
< 0,35 σ	Very well sorted	> + 0,30	Strongly fine skewed
0,35 – 0,50 σ	Well sorted	+ 0,30 to + 0,10	Fine skewed
0,50 – 0,71 σ	Moderately well sorted	+ 0,10 to -0,10	Near symmetrical
0,71 – 1,00 σ	Moderately sorted	-0,10 to -0,30	Coarse skewed
1,00 – 2,00 σ	Poorly sorted	< -0,30	Strongly coarse skewed
2,00 – 4,00 σ	Very poorly sorted		
> 4,00 σ	Extremely poorly sorted		

4.3.1.3 Intergranular volume

Intergranular volume (IGV) can be defined as the combined volume of the intergranular porosity, intergranular cement and depositional matrix in a given volume of rock, where depositional matrix represents clay- and silt size particles which is present between the framework grains (Paxton et al., 2002). IGV can be used to describe the effect of mechanical compaction prior to cementation and can give a valuable understanding of the influence of non-chemical processes involved in diagenesis.

Based on the petrographic observations, the IGV was calculated for each individual thin section and plotted against depth. In addition, the IGV results were compared with the intergranular volume compaction curve constructed by Paxton et al. (2002). Further, the IGV was plotted against statistical parameters such as sorting and average grain size in order to evaluate the effect of textural parameters which influences the degree of mechanical compaction.

4.3.2 Scanning Electron microscopy and Cathodoluminescence

The scanning electron microscope analysis was mainly used to provide a more detailed characterization of the clay fraction present in the intergranular pore space. During the optical microscopy analysis, different types of matrix where only classified on the basis of their visual appearance but no mineralogical classification were possible for finest fraction clay fraction. In addition, mapping revealed some new minerals which were not observed in the optical microscope. Chemical formulas of matrix minerals and some of the detrital grains encountered in this study are presented in the table below (table 4.5). Further, the Cathodo luminescence was used to detect cemented regions and describe detrital grains prior to cementation.

Table 4.5: The table displays a list of minerals and their chemical formula encountered during the SEM analysis.

Mineral	Chemical formula
Illite	$(K,H_3O)(Al,Mg,Fe)_2(Si,Al)_4O_{10}[(OH)_2,(H_2O)]$
Kaolinite	$Al_2Si_2O_5(OH_4)$
Mica (muscovite)	$KAl_2AlSi_3O_{10}(OH)_2$
Albite	$NaAlSi_3O_8$
K-feldspar	$KAlSi_3O_8$
Anorthite	$CaAl_2Si_2O_8$
Calcite	$CaCO_3$
Dolomite	$CaMg(CO_3)_2$
Ankerite	$Ca(Mg,Fe)(CO_3)_2$

4.3.3 Uncertainties

Petrographic analysis depends largely upon the experience of the interpreter where especially clay minerals can be difficult to recognize and hence quantify. K-feldspars, due to poor preserved grains, and particularly albite were extremely difficult to separate from the quartz grains and were only found during mapping in the scanning electron microscope. Further, the estimated quartz cement volumes are suggested to be undercounted due to lack of dust rims on a significant amount of the detrital quartz grains. Regardless of the number of available predefined charts which describe grain shapes, such analysis depends on the interpreter. Another degree of uncertainty relates to the sample- frequency and resolution within the Stø formation, where actually observations have been made. This becomes increasingly important to consider, particularly when data from the thin section analysis are presented in broader context, e.g. presented as the sequences described in section 4.2. However, the results from the petrophysical analysis are used as supplement to populate/predict properties beyond intervals with observed data.

4.4 Petrophysical analyses

4.4.1. Introduction

The petrophysical analyses of the Stø formation was obtained from well 7121/5-1 and 7120/6-1 using the Hampson and Russell™ software (HRS) and Petrel™. The main goals of the petrophysical evaluation were to describe lithological similarities and differences in the Stø formation, calculate porosity, describe compaction trends, predict quartz cement- and shale volume and estimate uplift. In addition, the logs were used to define the transition zone between mechanical- and chemical compaction and give an estimation of the geothermal gradient in the area. In the following, a presentation of the methods used to obtain results from petrophysical analysis will be given.

4.4.2 Lithology description

The lithological characterization of the Stø formation in a broad context was obtained by utilizing the gamma ray- and density log. The gamma ray log was used to separate between intervals with higher matrix content and intervals which appeared to be composed of clean sand. Based on the gamma ray log the Stø formation was divided into two sequences, as described in section 4.2. The density log was used to detect intervals with significantly higher densities. Densities above 2,5024 g/cm^3, which is the equivalent to for example a water saturated quartzite with a porosity of 9%, was colored red in order to localize these intervals.

4.4.3 Compaction trends

4.4.3.1 Geothermal gradient

The geothermal gradient was calculated in order to estimate the depth at which quartz cement and illite starts to precipitate. The geothermal gradient was derived from the following formula (Eq. 4.3):

Eq.4.3 $$g_G = \frac{BHT - T_{ms}}{TD} * 1000$$

where BHT represents the bottom hole temperature, T_{ms} is the mean surface temperature and TD is depth where BHT is measured.

4.4.3.2 Velocity log

The P-wav velocity logs was used to investigate to recognize compaction trends in a broader context in the study area. However, the P-wave was mainly examined in relation with other parameters such as porosity and quartz cement volume (see section 4.4.3.3 and 4.4.5). In order to obtain more accurately results utilizing the P-wave velocity through the Stø formation, hydrocarbon bearing intervals were substituted with water and new P-wave velocities were estimated. In well 7121/5-1, a gas bearing zone has been recognized in the interval from 2369 – 2427, 5 meters and the oil/water contact at 2442 meters. In well 7120/6-1 the gas/oil contact and oil/water contact has been found at 2427 meters and 2443 meters, respectively. The top of the reservoir was encountered at a depth of 2385, 5 meters (NPD, 2016). All depth measurements are given in measured depth from KB. The hydrocarbon bearing zones were assumed fully saturated with the respective saturating fluid and the output saturation was assumed be fully water saturated. The fluid substitution calculation was carried out in HRS using the Fluid Replacement Model (FRM). Input parameters used in the calculations are presented in the table below which is default parameters in HRS (table 4.6). The input porosity originated from the neutron-density porosity (total porosity).

Tabell 4.6: The table displays the input parameters used in the FRM in HRS.

Input parameters from FRM	
ratio quartz / clay	80 / 20 [%]
density quartz	2,65 [g/cm^3]
density clay	2,58 [g/cm^3]
density gas / oil / water	0,2 / 0,75 / 1,09 [g/cm^3]
bulk modulus / shear modulus quartz	36,6 / 45 [Gpa]
bulk modulus / shear modulus clay	20,9 / 6,9 [Gpa]

4.4.3.3 P-wave velocity vs. total porosity

The relation between velocity (P-wave) and porosity was investigated in order to describe compaction trends in the study area and more particularly within the Stø formation. In addition the degree of sorting was examined, as critical porosity is a function of sorting (and packing) at the time of deposition (Avseth et al., 2005). The aim was not to obtain a quantified number of the critical porosity/sorting, but rather use it to describe relative differences. A crossplot between the P-wave and total porosity for the Stø formation was exported from HRS and imported to Excel and plotted along with the diagenetic trends and suspension line described by Avseth et al. (2005).

Generally, as the porosity decreases due to compaction the P-wave velocity increases (Avseth et al., 2005). The diagenetic background trends used in this study describes compaction, as a function of P-wave velocity and porosity, of sediments from the time of deposition by the suspension line (Reuss bound) and connect it with the mineral point (figure 4.6, B). Newly deposited sediments will fall along the suspension line, where the critical porosity is controlled by packing and sorting. The diagentic trends describes the compaction evolution of lithologies with varying age and constant sorting, whereas the sorting trends describes lithologies with constant cement volume and varying sorting.

The contact cement model after Dvorkin and Nur (1996) is used to describe the upper boundary for cementation of clean sandstones. This line follows the same trend as the upper Hashin-Shtrikman bound except at the starting point for cementation, where only small amounts of cement significantly strengthen the rock frame and hence significantly increases the velocity (figure 4.6, A). The porosity is more or less constant during this early stage of cementation (Avseth, 2015). The diagentic trends displayed in figure 4.6 were included, as they represent the compaction development for a formation with different critical porosities.

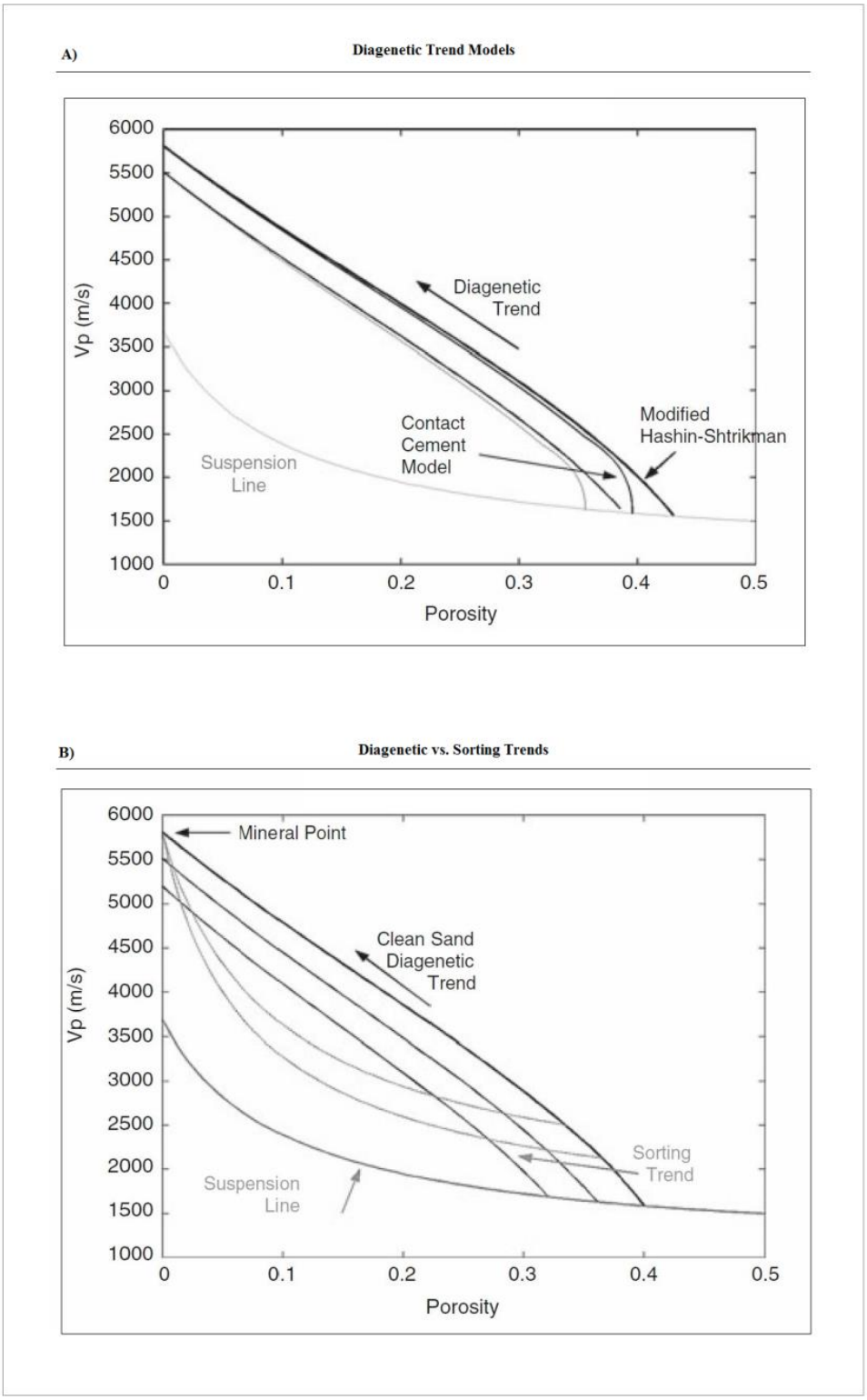

Figure 4.6: The figure displays some diagenetic trends used to investigate the Stø formation. A) the contact cement model after (Dvorkin and Nur, 1996). B) clean sand diagenetic trends described by (Avseth et al., 2005).

4.4.3.4 Uplift estimation

An uplift estimate was obtained by plotting the P-wave velocity against the true vertical depth (TVD). From the gamma ray log, accompanying velocity measurements with an API value below 60 were excluded from the velocity-depth relation; in order examine more shaly lithologies. The velocity-depth plot was compared with the linear velocity-depth trend of Storvoll et al. (2005), which is based on data consisting of mainly shales and shaly sediments.

4.4.4 Porosity estimation

Porosity estimates presented in this thesis were calculated in the HRS utilizing the equation for total porosity which combines both the density- and neutron derived porosity log (Eq. 4.4). By using this equation, it has been suggested that the lithology- and gas effect is more or less overpowered (Asquith and Krygowski, 2004b).

Eq. 4.4 $$\emptyset = \sqrt{\frac{\emptyset_N^2 + \emptyset_D^2}{2}}$$

The density derived porosity was calculated using the following formula (Eq.4.5):

Eq. 4.5 $$\emptyset = \frac{\rho_{ma} - \rho_b}{\rho_{ma} - \rho_{fl}},$$

Where ρ_{ma} is the density of the solid framework of the rock, ρ_b is the measured bulk density of the formation and ρ_{fl} is the fluid density occupying the pore space (Asquith and Krygowski, 2004b).

The neutron log measures the hydrogen concentration of a formation, which for a shale-free lithology more or less are a function of the pore filling fluid. The energy loss associated with the interaction of a hydrogen atom and a neutron are used to relate the hydrogen concentration to the porosity of clean formation (shale free formation) (Asquith and Krygowski, 2004b).

The calculated total porosity value was exported from HRS and imported to Excel and plotted along with the observed porosities obtained from the petrographic analysis.

4.4.5 Estimating cement volume

In order to obtain an estimate of the quartz cement volume within the Stø formation during the petrophysical analysis, the p-wave velocity data was compared with a study published by Marcussen et al. (2010). This study aimed to describe the quartz cement volume, among other topics, in the Etive formation from the North Sea at various depths and locations to be able to link the observed cement volume to the p-wave velocity. They constructed a linear relation between the observed quartz cement volume and the P-wave velocity, which is presented in figure 4.7. Further, the Etive formation was described as a quartzite to subarkosic in composition, with minor amounts authigenic clays such as illite and kaolinite. This makes this formation comparable with the Stø formation analyzed in this study. Hence, the p-wave velocities within the Stø formation were compared with the chart below (figure 4.7) and an estimation of the quartz cement volume was obtained. The cement volume was calculated for every single velocity measurement in each well. This result is presented along with observed quartz cement volume obtain from the petrographic analysis. The calculated cement volume derives from the equation below (Eq. 4.6) which represents the linear relation obtained by Marcussen et al. (2010).

Eq. 4.6 $$V_p = 84{,}95V_{qz} + 2775{,}21,$$

where V_p equals the P-wave velocity in m/s and V_{qz} represents the quartz cement volume. Rearranged the cement volume was estimated from the following (Eq. 4.7):

Eq. 4.7 $$V_{qz} = \frac{V_p - 2775{,}21}{84{,}95}.$$

Equation (4.6/4.7) was calculated from digitized data of figure 4.7 and may not represent the linear relation accurately.

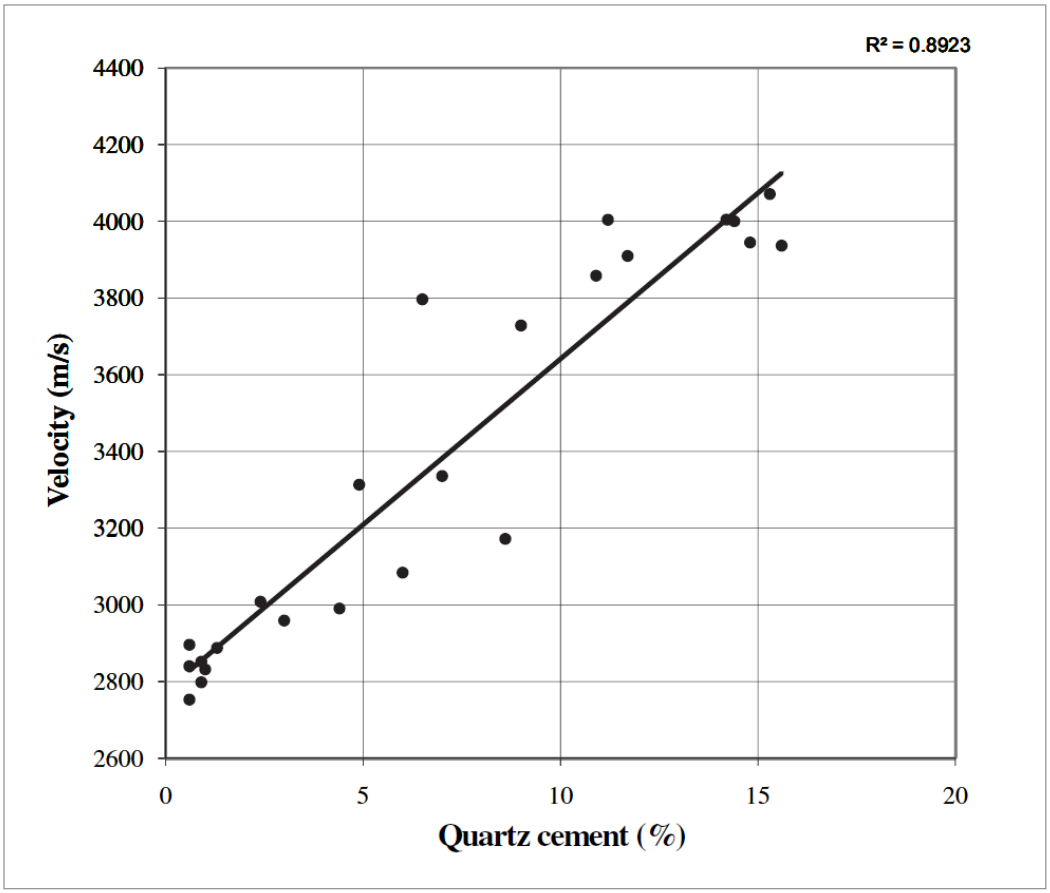

Figure 4.7: The figure displays the relation between Sonic velocity (P-wave) and quartz cement volume (Marcussen et al., 2010).

4.4.6 Shale volume estimation

The shale volume represents the fraction of the total rock volume of which is occupied by clay or other fine grained particles (Szabó, 2011). The shale volume predictions used in this study is based on the gamma ray log which is sensitive to the amount of thorium (Th), uranium (U) and potassium (K) present in the formation (Asquith and Krygowski, 2004a). The gamma ray index (I_{GR}) was calculated using (Eq. 4.8) in order to estimate the shale-volume (V_{sh}). The relation between I_{GR} and V_{sh} presented using a non-linear relation, called the Steiber correction (Eq. 4.9). Several non-linear relations exist which yields various shale volume for a given I_{GR}. The Steiber correction is used in this study, as the estimated shale volume is an intermediate value between the end-members, i.e corrections which returns either a higher or lower estimated shale volume (Asquith and Krygowski, 2004a). GR_{max} and GR_{min}, representing intervals which are believed to be clean shale and sand, were determined using the gamma ray log and a neutron-density crossover plot. The lower part of the Stø formation was used as reference for clean sand and an API value of 15 and 45 was used in well 7121/5-1 and 7120/6-1, respectively. Along with the gamma ray log, negative separations in the neutron-density crossover plot were used to identify clean shale intervals. The Fuglen-, Tubåen and Fruholmen formations have frequently intervals with a clear negative separation and were used to define clean shale in terms of API values. In well 7121/5-1, clean shale was set to an API value of 100, whereas for well 7120/6-1 an API of 120 was used.

Eq. 4.8 $$I_{GR} = \frac{GR_{log} - GR_{min}}{GR_{max} + GR_{min}}$$

(Asquith and Krygowski, 2004a)

E.q 4.9 $$V_{sh} = \frac{I_{GR}}{3 - 2 * I_{GR}}$$

(Asquith and Krygowski, 2004a)

4.4.7 Uncertainties

There will always be uncertainties related to petrophysical analysis, as a significant amount of the rock properties (e.g., density and porosity) obtained from such analysis are predicted from indirectly related measurements of for example acoustic-, radioactive- or electric properties. Further, formulas used to calculate various rock properties from these measurements requires, in some cases, that input parameters most be estimated. For example, when estimating the shale volume of a formation an upper- and lower gamma ray response, representing clean sand and pure shale respectively, must be determined in order to calculate the shale volume. In addition, the total gamma ray response was used to calculate shale volume, which for sandstones may yield an inaccurate result since greater amounts of uranium in the formation water or significant amounts of potassium minerals will influence the response (Asquith and Krygowski, 2004a). Another degree of uncertainty worth mentioning is when velocity/porosity depth trends have been compared with published diagenetic trends where these trends derive from datasets from other geographical locations, stratigraphical levels and type of formations. These trend lines can be used as guide lines for predicting e.g. velocity trends at a given depth, but the results should be handled with care. This is also true when the estimating the amount of quartz cement volume from a linear relation between P-wave velocity and quartz cement volume. Despite the uncertainties; the geophysical logs has been used in this study to recognize trends mainly within the Stø formation, where petrographical observations have been made frequently. This gives an increased level of confidence when utilizing the well logs as guide lines between levels where actual observations have been made.

5. Petrographic analysis

5.1 Introduction

Results obtained during the petrographic analysis will be presented in the following. This includes all aspects thought to be of importance for the reservoir quality of the Stø foramtion. Firstly, results obtained from the optical microscope will be presented and the results from the scanning electron microscope will be included at the end of this chapter.

5.2 Optical microscopy

5.2.1 Mineralogy

The mineralogical bulk volume results from the point count can be seen in figure 5.1 and 5.2 (also presented in Appendix A). These results show that the Stø formation is almost entirely composed of quartz where rock fragments only make up a small fraction of the rock frame. No feldspar was found during the point count, but the SEM analysis indicated that minor amounts of albite and K-feldspar is present (see section 5.2.5). The detrital quartz grain content is nearly constant in all the samples and commonly makes up 70 – 80% of the bulk volume. Small amounts of muscovite and kaolinite represents only a smaller fraction of the bulk volume. In terms of sandstone classification, all the samples would classify as quartz arenites as the relative content of feldspar and rock fragment compared to the quartz content is less than 5% in all the samples and the clay content is less than 15%. The clay volume varies significantly and it seems that thin section 6-8 in well 7121/5-1, and thin section 17-20 in well 7120/5-1 has the lowest clay content. This corresponds to sequence A2 and B2 (see section 4.2). Please note that thin section 1 only represents 150 data-points (see section 4.3.1.1).

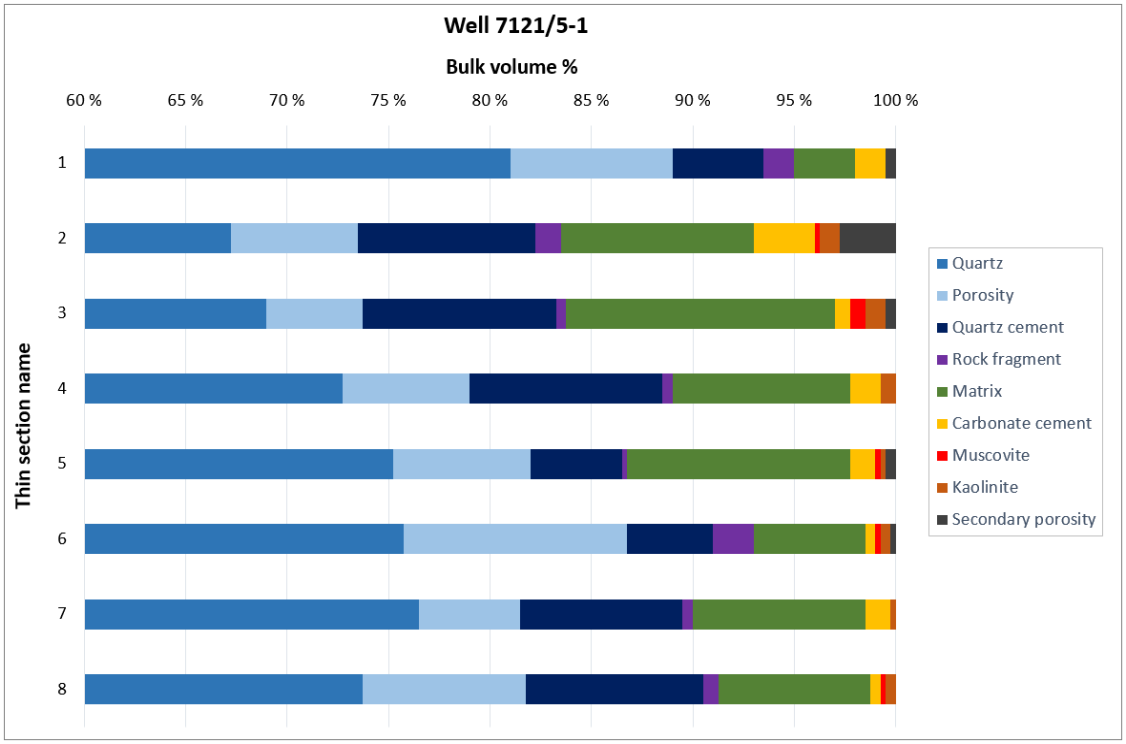

Figure 5.1: The figure summarizes the results obtained from the point count in the thin sections from well 7121/5-1. The results are presented as a percentages of the bulk volume. Note that the percentage starts at 60% and that detrital quartz grains represent the range between 0-60%.

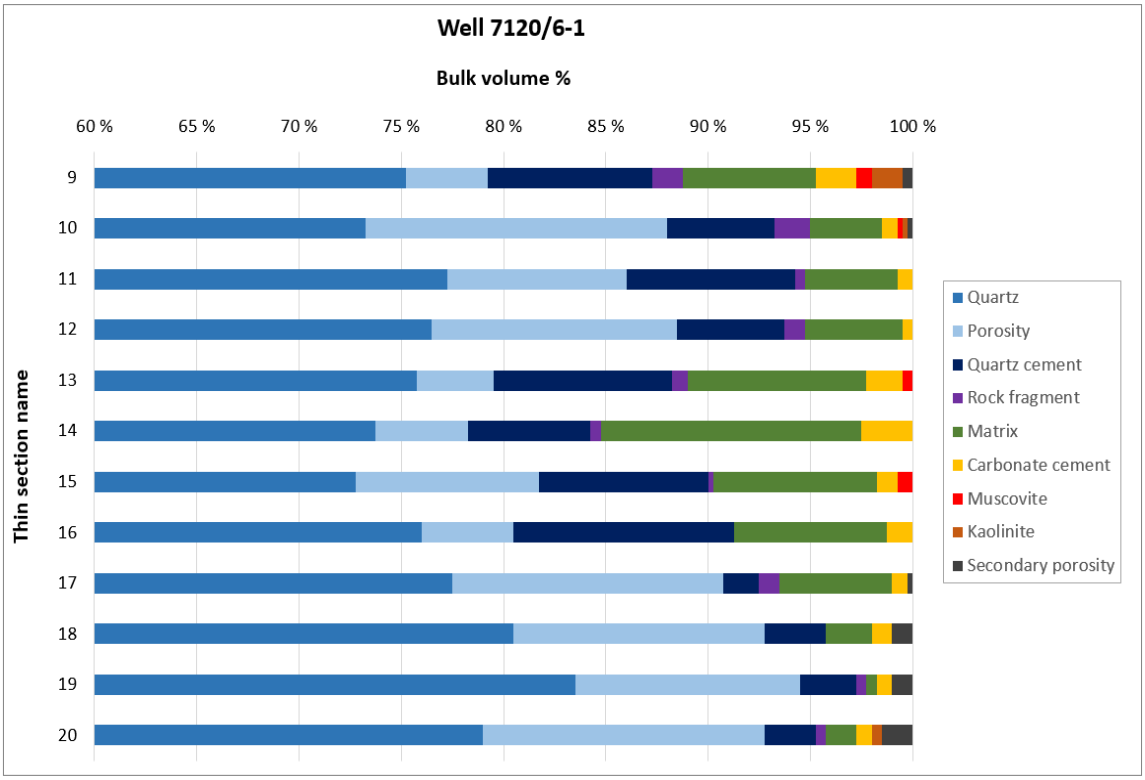

Figure 5.2: The figure summarizes the results obtained from the point count in the thin sections from well 7120/6-1. The results are presented as a percentages of the bulk volume. Note that the percentage starts at 60% and that detrital quartz grains represent the range between 0-60%.

5.2.2 Porosity and Quartz cement

The fraction of the estimated bulk volume which represents porosity and quartz cementation is presented in figure 5.3 and 5.4. In well 7121/5-1, the observed porosity commonly displays values in the range of 5-8% and a weak increase in porosity is observed with depth represented by the linear porosity line. The linearized quartz cement volume in this well is more or less constant at 7% of the bulk volume. However, thin sections 2-4 (sequence A1) displays higher cement volumes. In well 7120/6-1 (figure 5.4), a relation between porosity and quartz cement can be observed, where low cement volumes commonly are associated with high porosity intervals and vice versa. The results from the point count indicate a high porosity interval in sequence B2 (thin section 17-20) with low cement volume.

An example of a high- and a low cement volume interval observed in the optical microscope are presented in figure 5.5. This figure illustrates regions which are nearly totally cemented in sequence A1 and that sequence B2 are less influenced by quartz cement. In addition, figure 5.6 shows examples from the same two sequences (A1 and B2) where two thin section locations are presented in relation to the distances between the sample depth and the nearest clay-rich region and/or stylolites. The example shown from sequence B2 (B) are located approximately a meter away from clay-rich regions and observed stylolites, whereas in the example from sequence A1 (A) the distance to the nearest clay-rich region/stylolite is in the order of a few tens of centimeters. In figure 5.7, an example of the interaction between muscovite and quartz can be seen, where it looks like the muscovite has partly dissolved the quartz grain at the grain contact. Such micro-stylolites are more frequently observed within upper part of the Stø formation, i.e. sequence A1 and B1. Further, in figure 5.8, the relation between quartz cement and mean grain size indicates that finer grained sands have a higher cement volume than the coarser grained intervals.

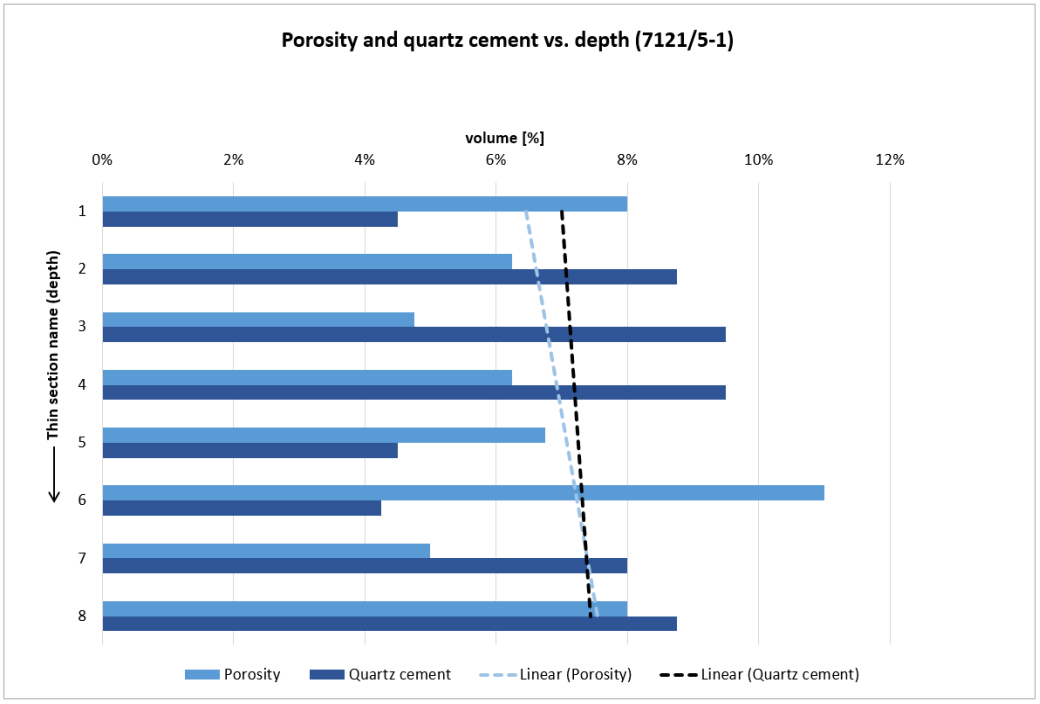

Figure 5.3: The figure shows the observed quartz cement volume in relation with observed porosity, as a fraction of the total bulk volume. The highest observed cement volumes are located in thin section 2-4 (sequence A1).

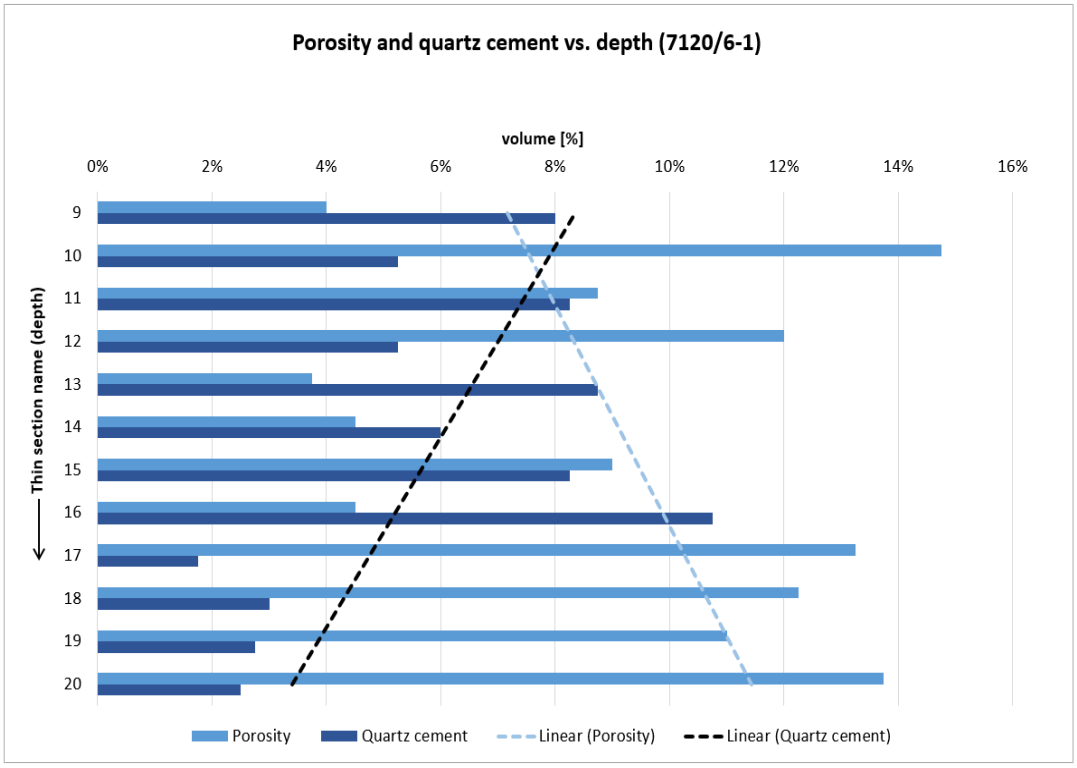

Figure 5.4: The figure displays the observed quartz cement content and porosity within the Stø formation in well 7120/6-1. A trend can be observed between the observed quartz cement content and porosity.

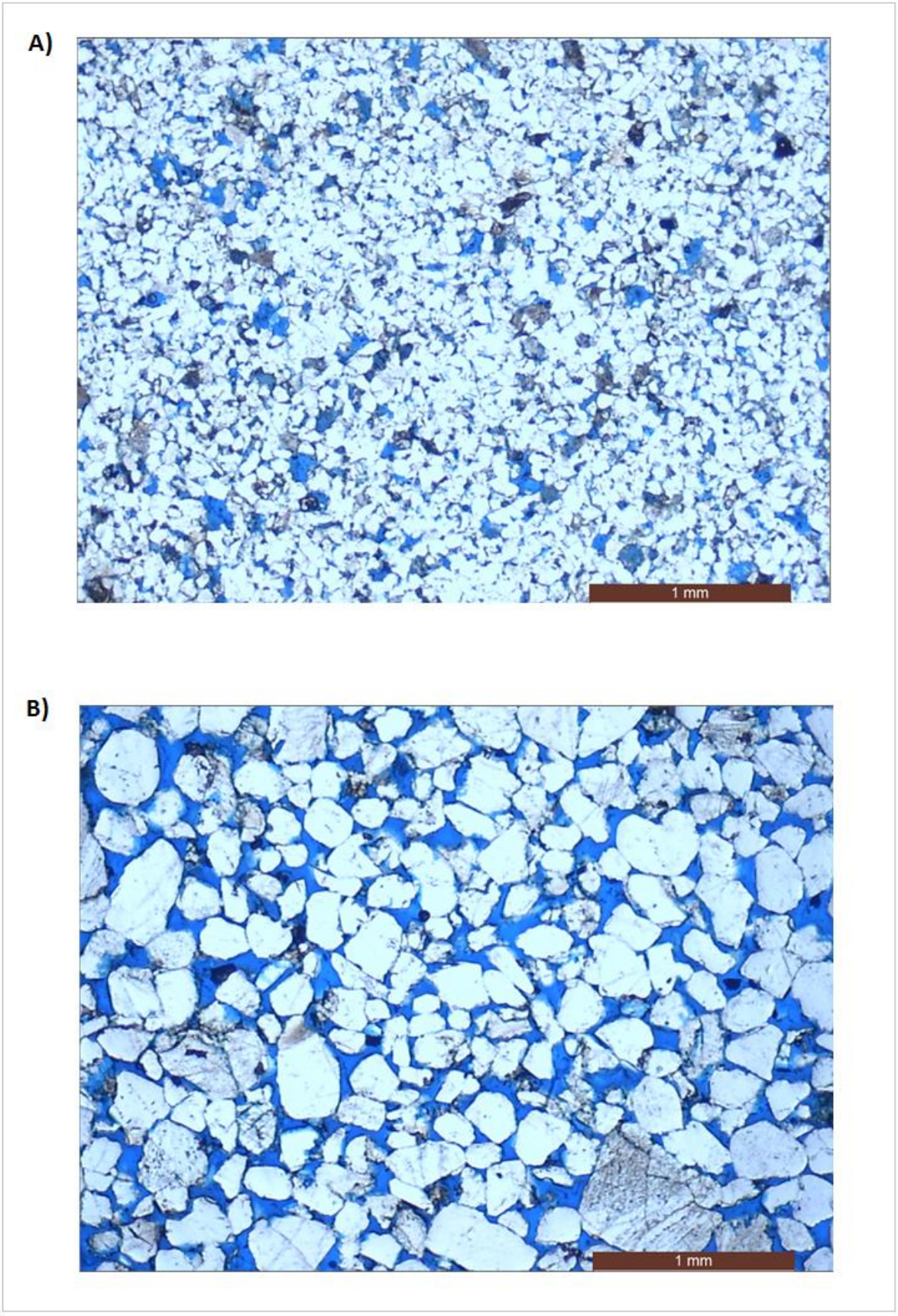

Figure 5.5: The figure shows an example of an interval with high and low cement volume taken in an optical microscope. The high cement volume interval (A) is taken in sequence A1 (exemplified by thin section 3) and the low cement volume interval originates from sequence B2 (demonstrated by thin section 20).

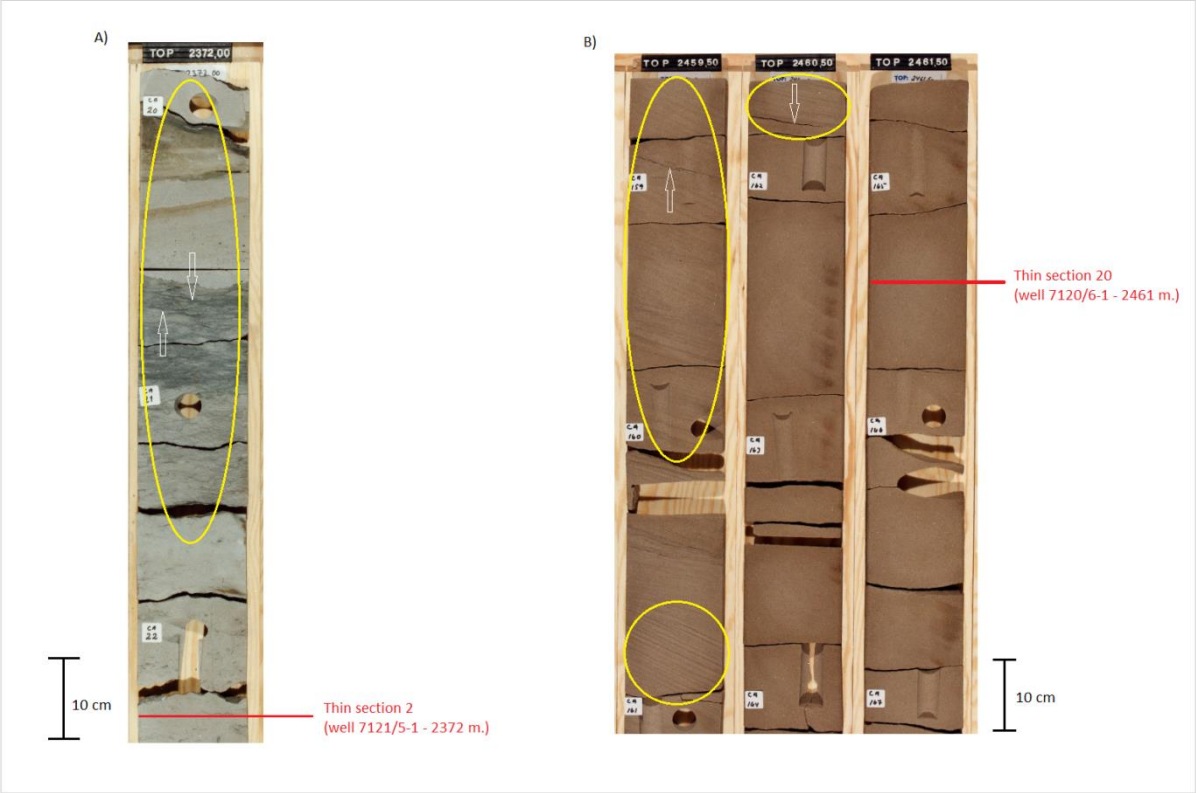

Figure 5.6: The figure shows two examples of spacing between the thin section analyzed and the distance to the nearest clay laminated region (marked in yellow). Observed stylolites are also marked on the figure (white arrows). Example A) is taken from well 7121/5-1 within sequence A1 (thin section 2 marked) and example B) is taken from well 7120/6-1 within sequence B2 (thin section 20 marked). Corephotos taken from (NPD, 2016).

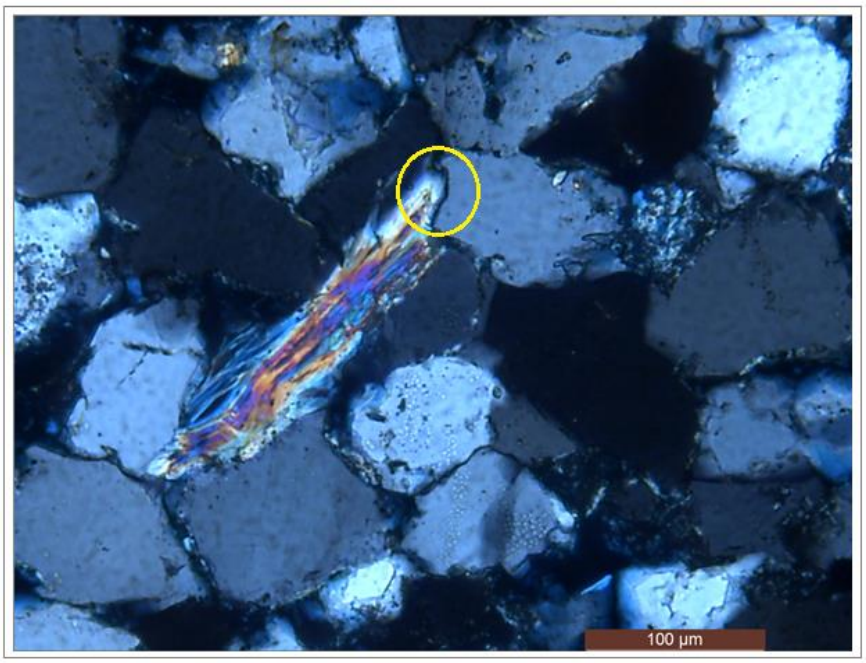

Figure 5.7: An example of the interaction between a quartz grain and a muscovite from thin section 15 in well 7120/6-1.

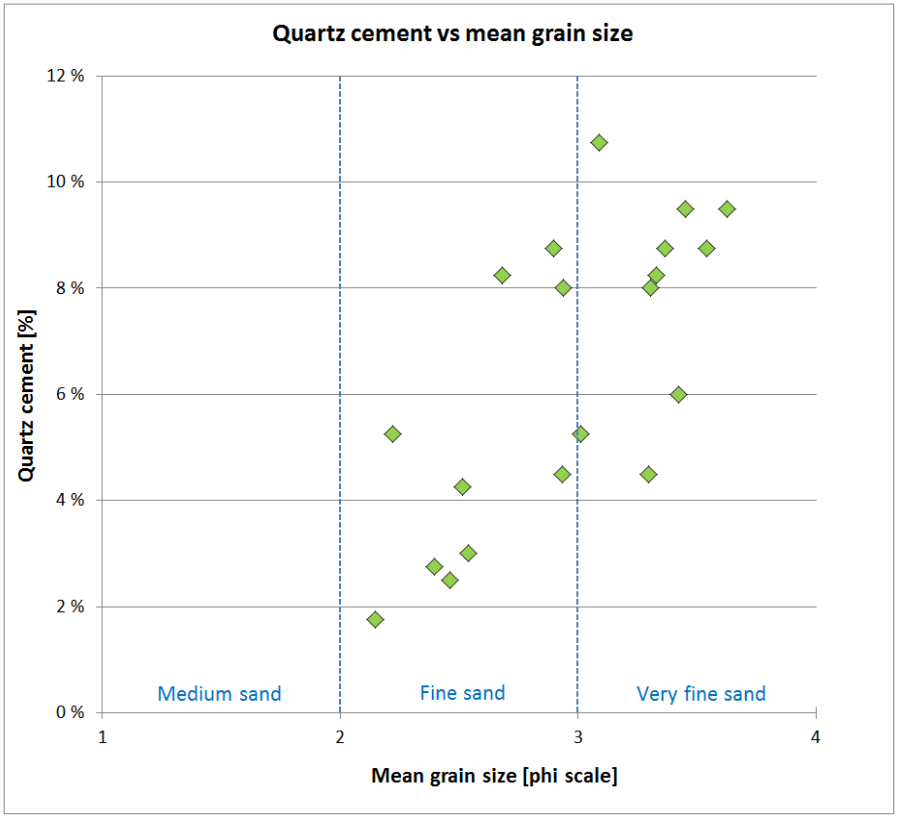

Figure 5.8: The figure displays the relation between mean grain size and observed quartz cement volume in all the thin sections.

5.2.3 Porosity and matrix

In figure 5.9 and 5.10 the total clay- and porosity volume for both wells are presented. In terms of clay volume, a boundary can be observed in both wells; where a noticeable decrease in clay content can be seen at the boundary between thin section 5 and 6 in well 7121/5-1 and between thin section 16 and 17 and in well 7120/6-1 (figure 5.9 and 5.10). These boundaries correspond to the separation of sequence A1 and A2, B1 and B2 in well 7121/5-1 and 7120/6-1, respectively. The highest clay volumes are observed in the interval between thin section 2 to 5 in well 7121/5-1 and between thin section 13 to 16 in well 7120/6-1. It should be noted that significant amounts of the clay sized fraction of the bulk volume are located within thin clay laminations (figure 5.11 A), where regions beyond these clay stringers appears much more clean. Further, the thin clay laminations were only located within sequence A1 and B1. Pore-filling clays are also sporadically observed within the Stø formation and an example can be seen in figure 5.11 B. A more detailed clay characterization will be presented in section 5.3.2.

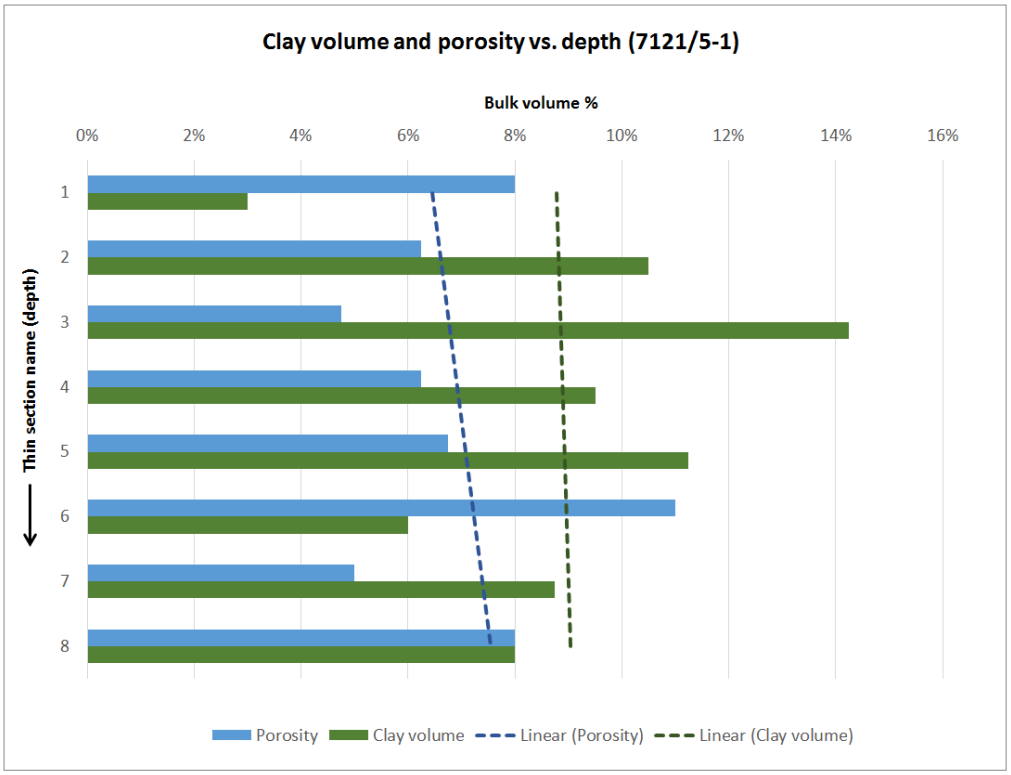

Figure 5.9: The figure displays the relation between observed clay content and porosity within the Stø formation in well 7121/5-1.

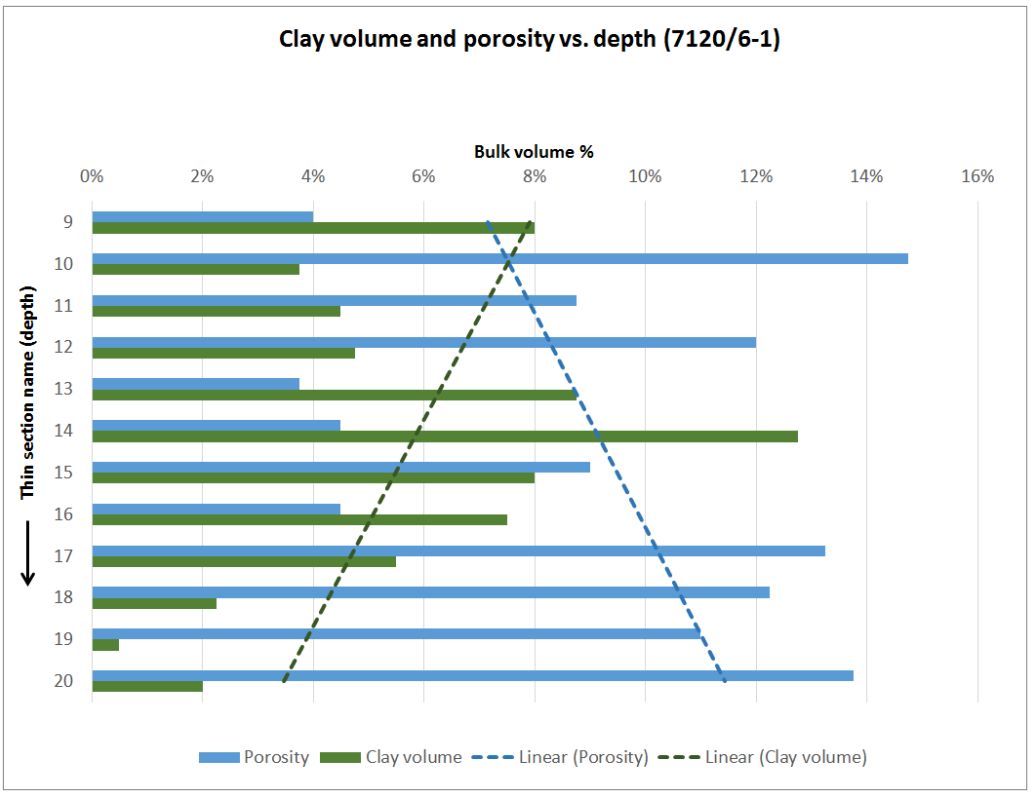

Figure 5.10: The figure displays the observed clay content and porosity in well 7120/6-1.

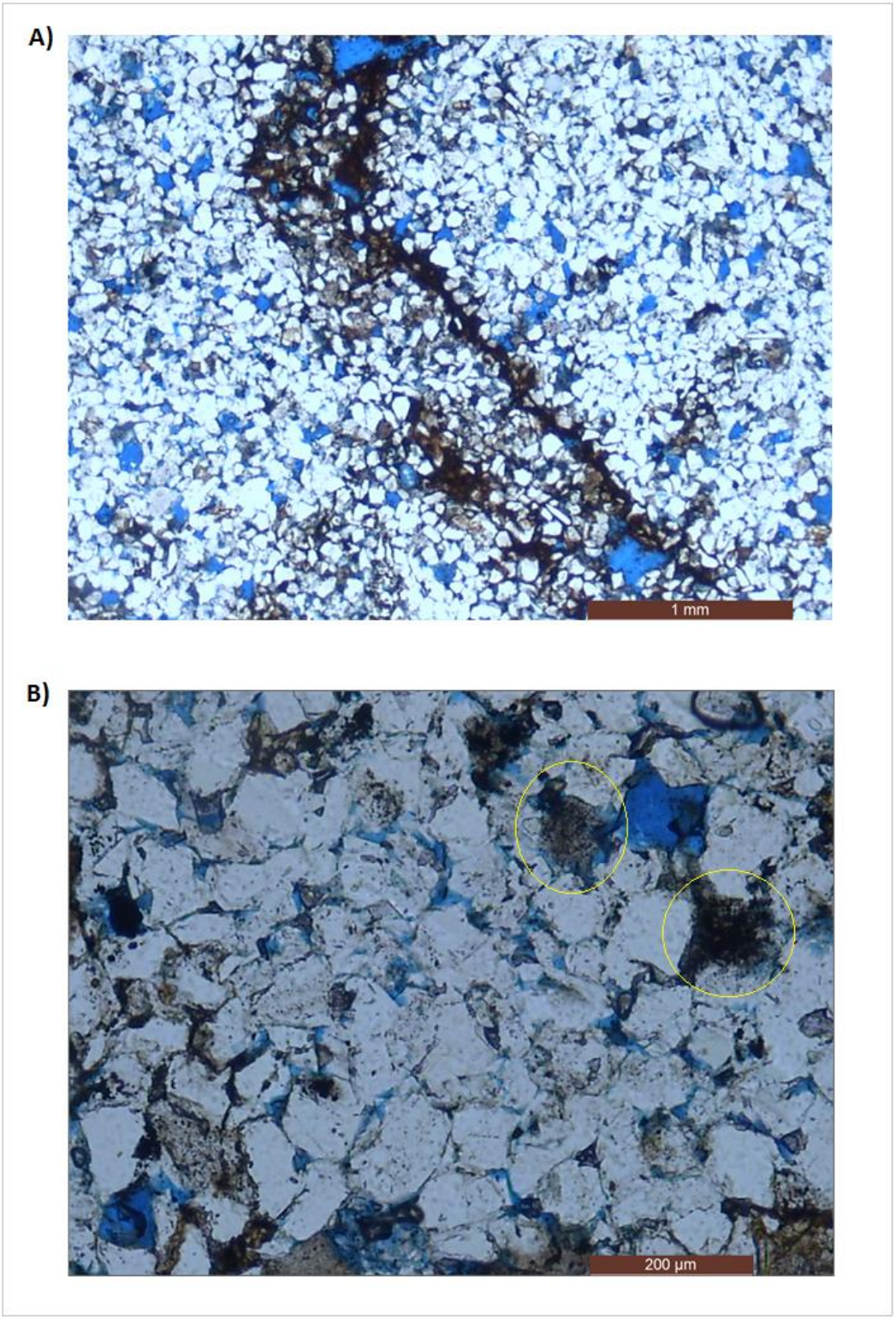

Figure 5.11: The figure shows the two most common modes of matrix occurrences. A) great amounts of the matrix volume observed in the thin sections are located within thin clay laminations; exemplified by a picture taken from thin section 3 (Sequence A1). B) the figure displays an example of pore-filling matrix and was taken from thin section 14 (Sequence B1).

The relation between observed muscovite and pore-filling kaolinite is presented in figure 5.12. The result suggests that an increase/decrease in muscovite content corresponds to an increase/decrease in kaolinite content. Further, the muscovite content is lower than the kaolinite content in all the samples. An example of pore-filling kaolinite and a heavily dissolved muscovite grain can be seen in the micrograph below, figure 5.13.

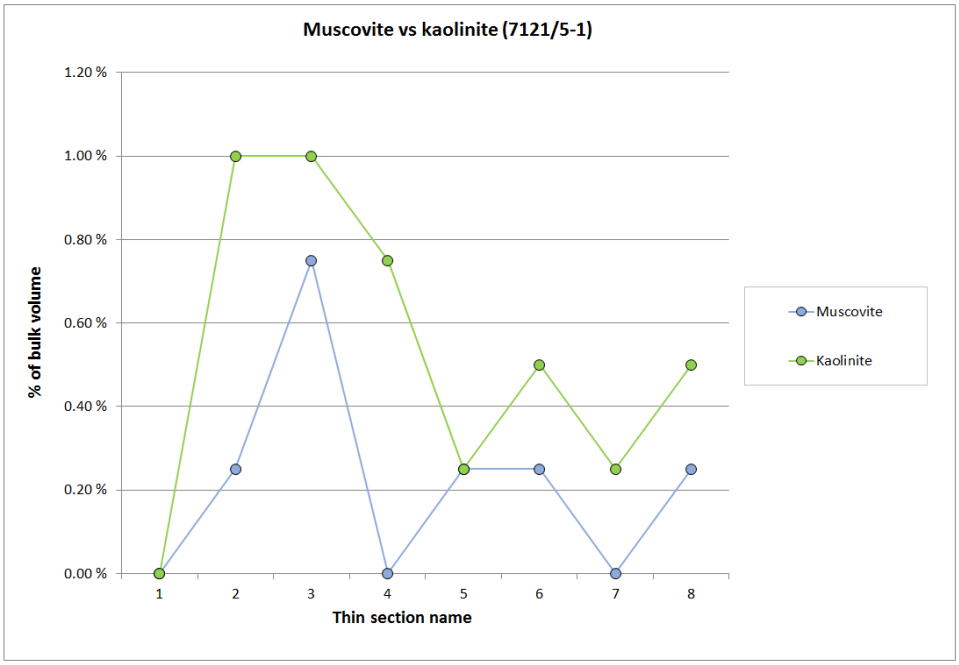

Figure 5.12: The figure displays the relation between the mica and kaolinite content in all the thin sections in well 7121/5-1. The kaolinite fraction presented here is only the amount of macroscopic kaolinite crystals, which is observable in the optical microscope.

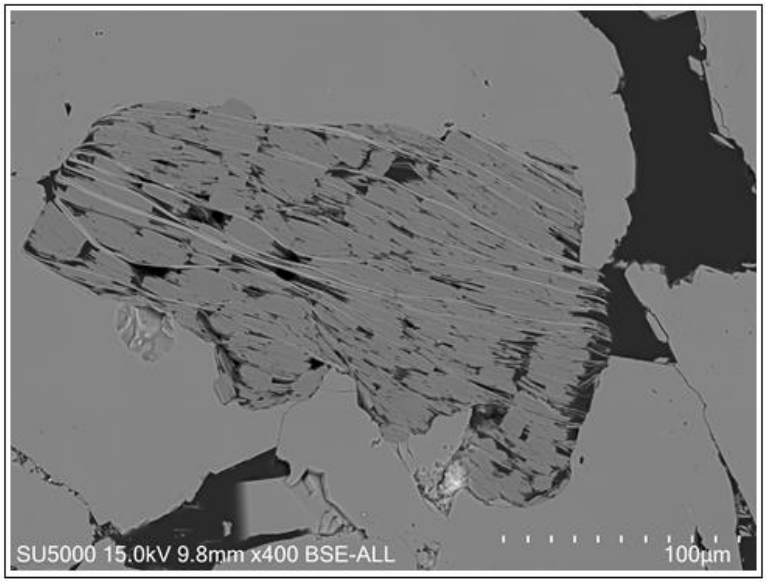

Figure 5.13: A micrograph of an almost entirely dissolved mica grain and where kaolinite has been precipitated. Example from well 7121/5-1, thin section 6.

5.2.4 Textural properties

5.2.4.1 Grain size

In figure 5.14, a cumulative frequency plot displays the grain size distribution within each sequence in both wells. The results suggest that the lower sequences (A2, B2) in the Stø formation are slightly coarser grained than the upper sequences (A1, B1). Further, sequence B2 (7120/6-1) seems to be the coarsest grained interval in the Stø formation where the majority of the grain sizes are above 3 on the phi scale. A more illustrative demonstration of the grain size distribution for each sequence is presented in figure 5.15. This figure shows that the upper sequences (A1, B1) have their majority of grain sizes in the very fine sand range. The lower sequences (A2, B2) consist of greater amounts of fine sand, and sequence B2 has the highest amounts of medium sized sand particles.

Further, statistical parameters such as sorting and skewness for each sequence are presented in table 5.1. The sorting calculations suggest that both sequences in well 7121/5-1 are well sorted, whereas the sequences in well 7120/6-1 are moderately well sorted. In terms of skewness, all the grain size populations suggest a nearly symmetrical distribution, except for sequence B1 which is coarse skewed.

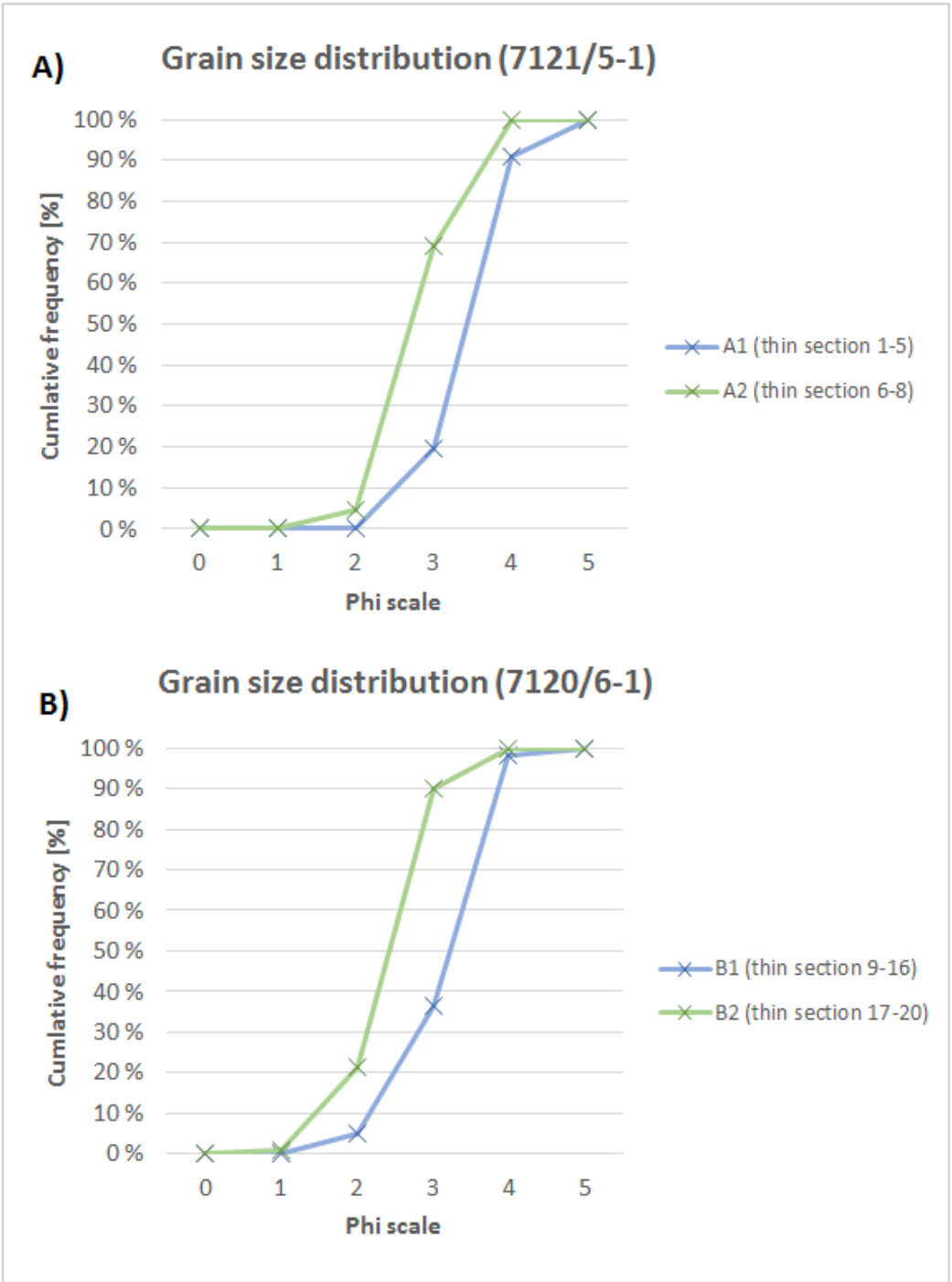

Figure 5.14: The figure displays the grain size distribution within each sequence in well 7121/5-1 (A) and well 7120/6-1 (B).

Table 5.1: Statistical parameters such as sorting and skewness are presented for each sequence in the table. Sequence A1 and A2 are better sorted than sequence B1 and B2. A near symmetrical distribution of the grain size population is found in sequence A1, A2 and B2, whereas sequence B2 is coarse skewed.

Statistical parameters (grain size)					
Well name	Sequnce	Sorting	Verbal term	Skewness	Verbel term
7121/5-1	A1	0,466	well sorted	0,0052	near symmetrical
	A2	0,451	well sorted	-0,0638	near symmetrical
7120/6-1	B1	0,621	moderately well sorted	-0,1842	coarse skewed
	B2	0,502	moderately well sorted	-0,0118	near symmetrical

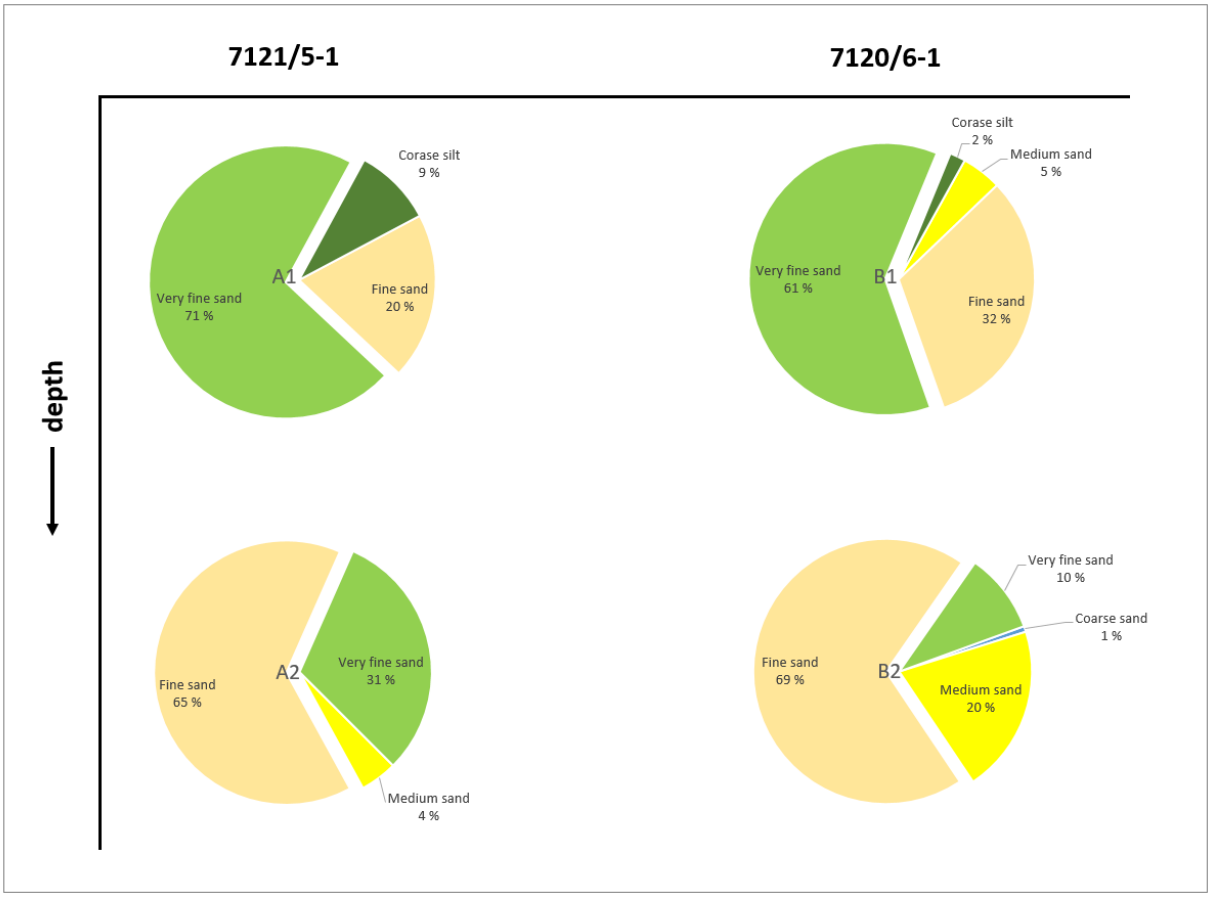

Figure 5.15: The figure displays the percentage of different grain sizes present within each sequence in both wells. The upper sequences A1 and B1 consists of mainly very fine sand, whereas the lower sequences in both wells are slightly coarser grained. Sequence B2 have the highest amount of medium sized sand.

5.2.4.2 Grain shape

The grain shape results obtained during the petrographic analysis are presented sequentially in figure 5.16 and 5.17. In terms of sphericity (figure 5.16), the ratio of high-to-low sphericities is more or less equally distributed within each sequence. Low sphericity grains are dominant in all the samples, where sequence A1 has a slightly higher ratio of high/low sphericity grains. The grain roundness results suggest that angular to sub-angular grains are the dominant particle shape present in all the sequences (figure 5.17). However, sequence B2 has a higher percentage of sub-angular grains compared with other the samples. SEM and CL examination revealed new findings directly related to these parameters, which may significantly alter the understanding of these data (see section 5.3.1).

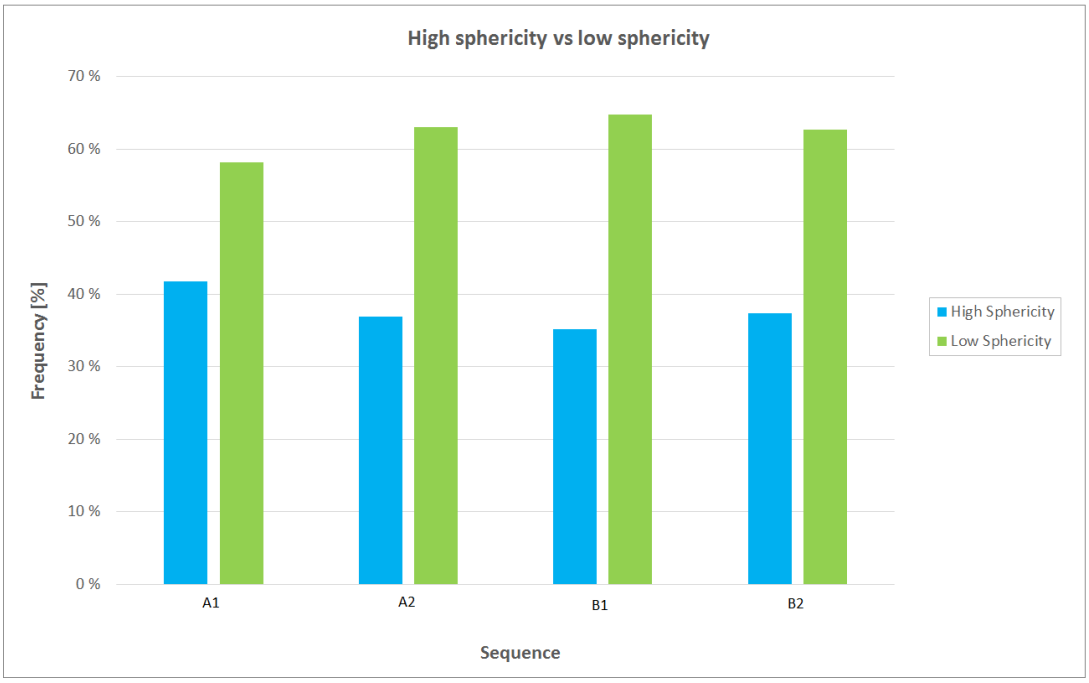

Figure 5.16: The figure displays the sphericity results within each sequence.

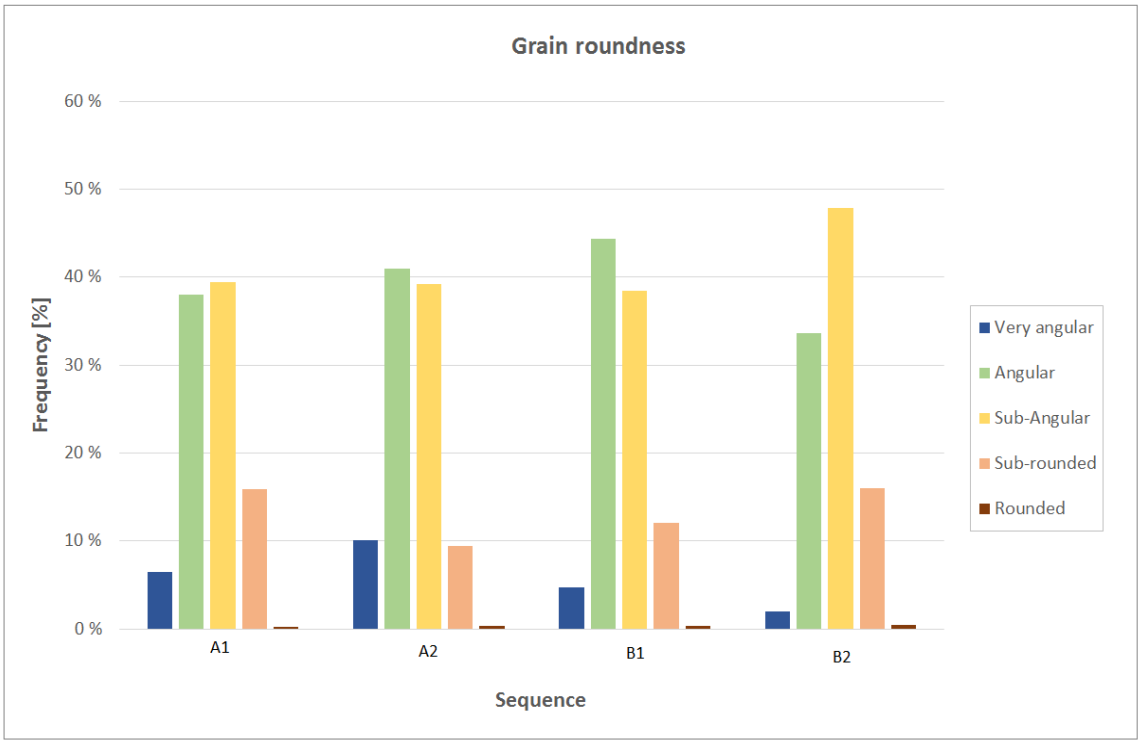

Figure 5.17: The figure shows the grain roundness results obtained during the examination of the thin sections in the optical microscope. The results are presented sequentially.

5.2.4.3 Grain contacts

The observed grain contacts (figure 5.18) shows similar trends compared with grain roundness results. Sequence A1, A2 and B1 shows generally the same distributions in terms of grain contacts, while sequence B2 indicate a higher percentage of long- and point contacts relative to the sutured contacts.

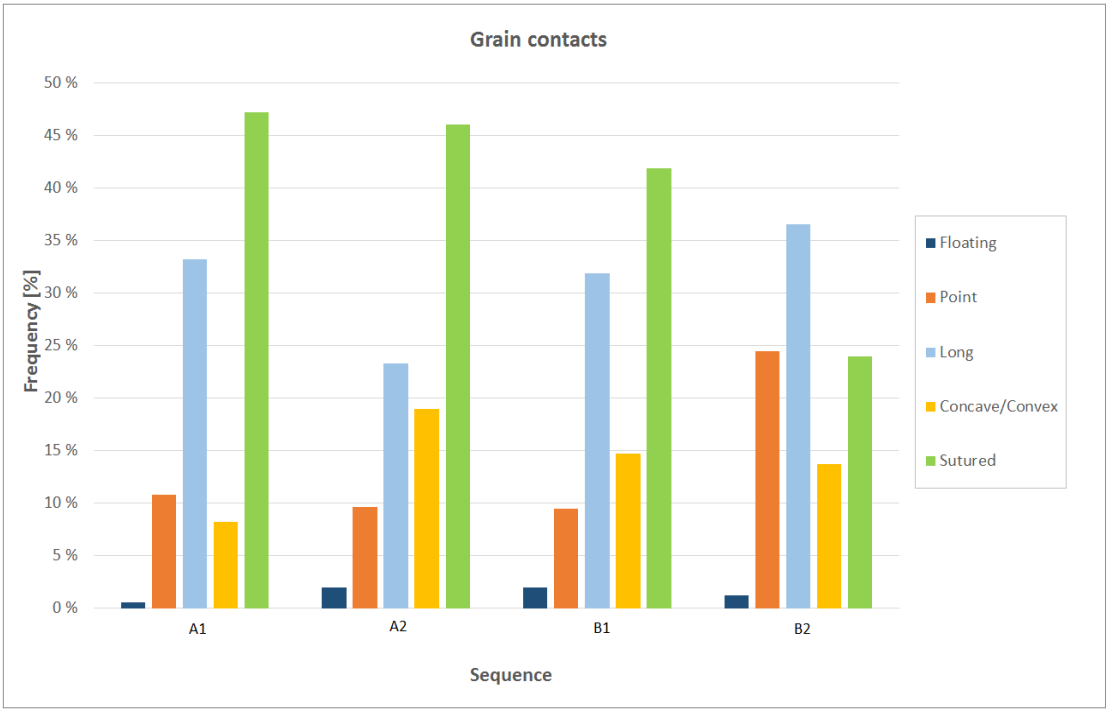

Figure 5.18: The figure shows the percentage of different grain contacts observed in each sequence. Sutured grain contacts dominate in all the sequences, except in sequence B2 where a higher amount of point- and long gain contacts are observed.

5.2.5 Intergranular volume

The intergranular volume (IGV) estimates for each individual thin section are presented in figure 19, 20 and 21. In figure 19, the predicted IGV is compared with IGV compaction curve of Paxton et al. (2002) as a function of depth. The majority of the predicted IGV values are somewhat lower than the IGV compaction curve and commonly plots in the range of 21-28%. Four of the points displays atypically low IGV values, i.e. below 20%. In figure 20 and 21 the estimated IGV are plotted against depth within the Stø formation in both wells, respectively. A trend can be observed in both cases, where it seems that the upper sequences A1 and B1 (thin section 2-5 and 9-16 in well 7121/5-1 and 7120/6-1, respectively) have slightly higher IGV than the lower sequence A2 and B2.

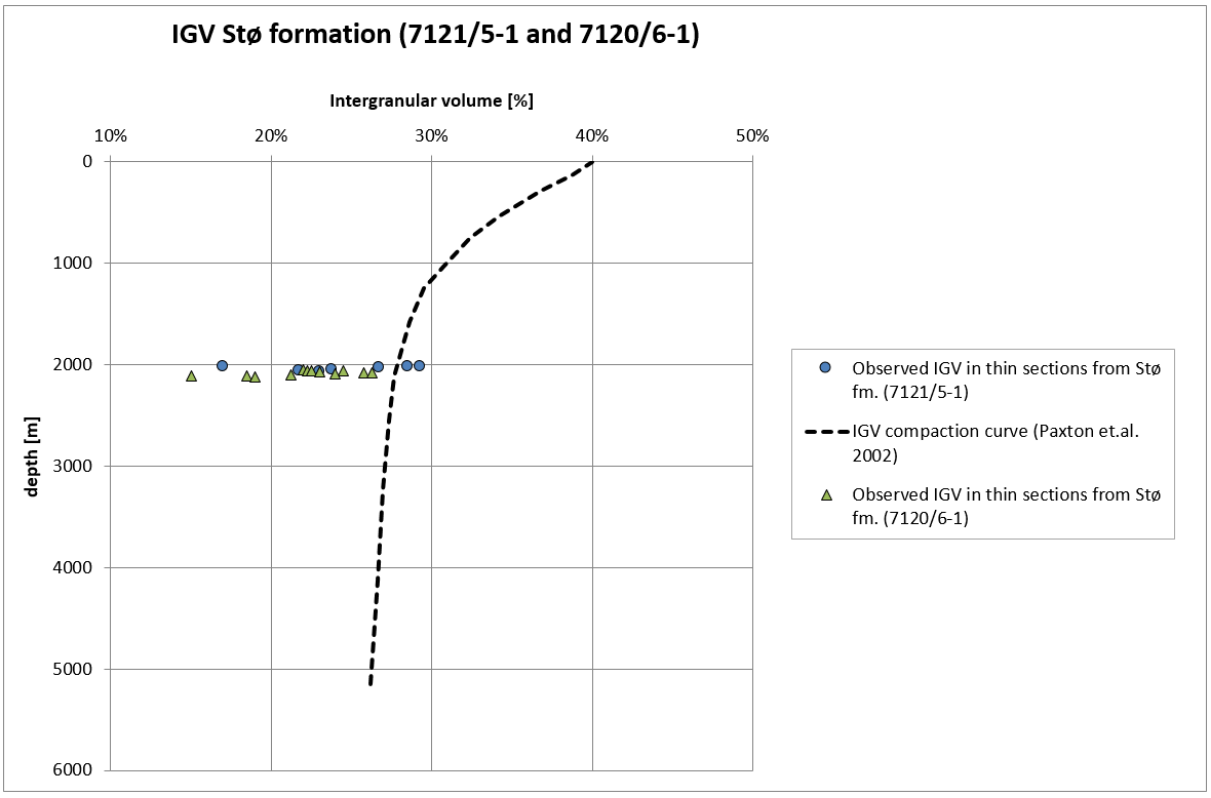

Figure 5.19: The figure shows the predicted IGV results for all the thin section individually. The results are compared with the IGV compaction curve of Paxton et al. (2002).

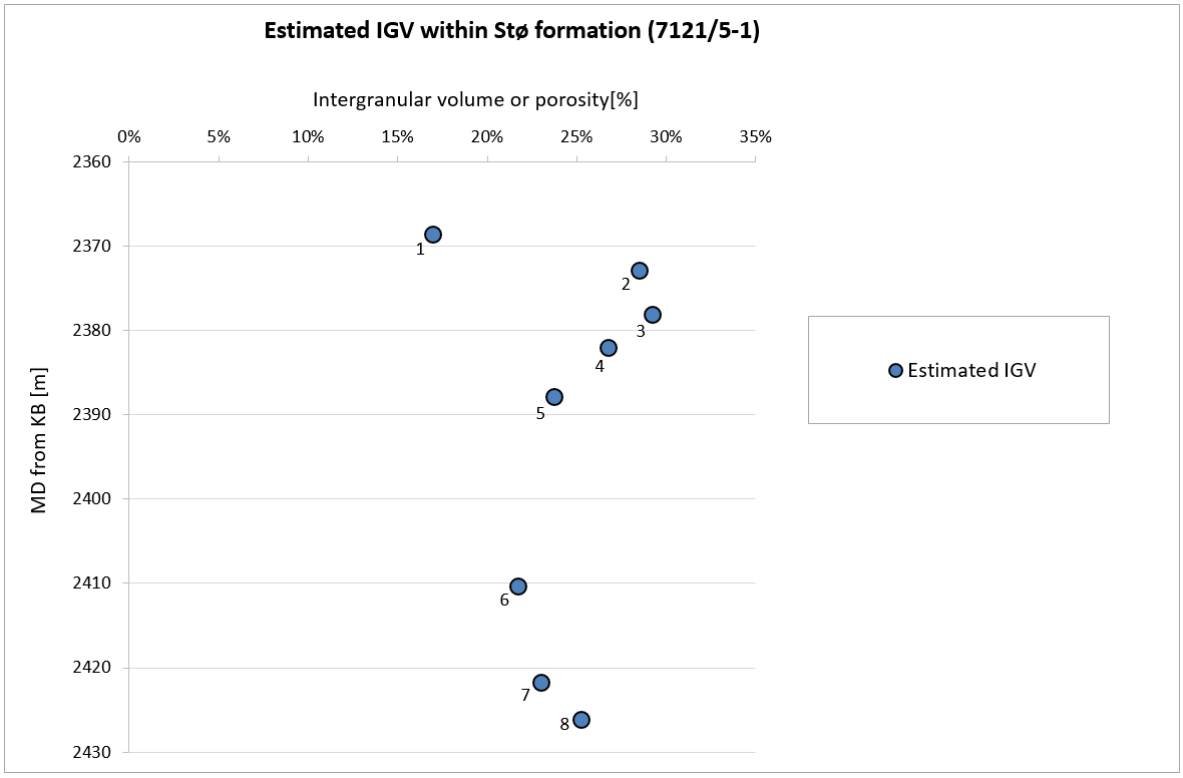

Figure 5.20: The figure displays the predicted IGV results from all the thin sections within the Stø formation in well 7151/5-1.

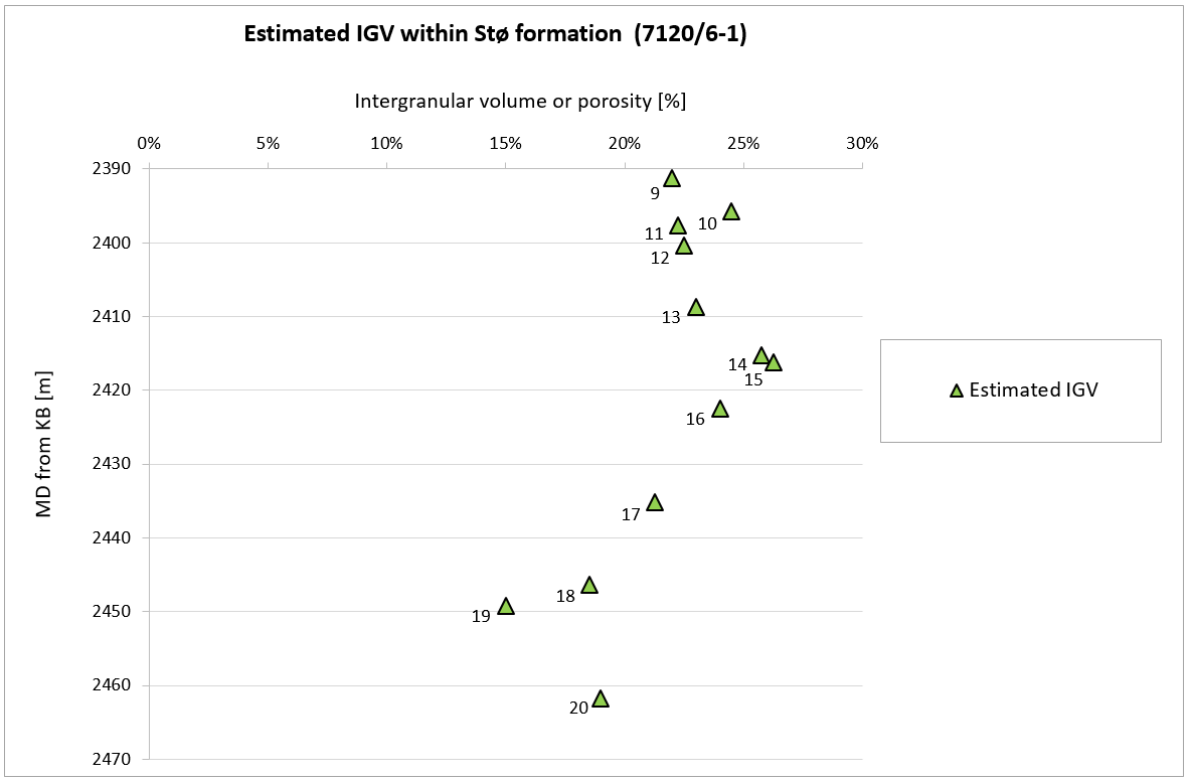

Figure 5.21: The figure displays the predicted IGV results from all the thin sections within in the Stø formation in well 7120/6-1.

In figure 5.22 and 5.23, the estimated IGV are presented in relation to grain size and sorting. Figure 5.22 relates the average grain size within each thin section to the estimated IGV, and a trend can be seen where the intervals with a higher fraction of finer grains have a higher IGV. Similarly, from figure 5.23, a trend can be seen where samples with a better sorting displays the highest IGV values.

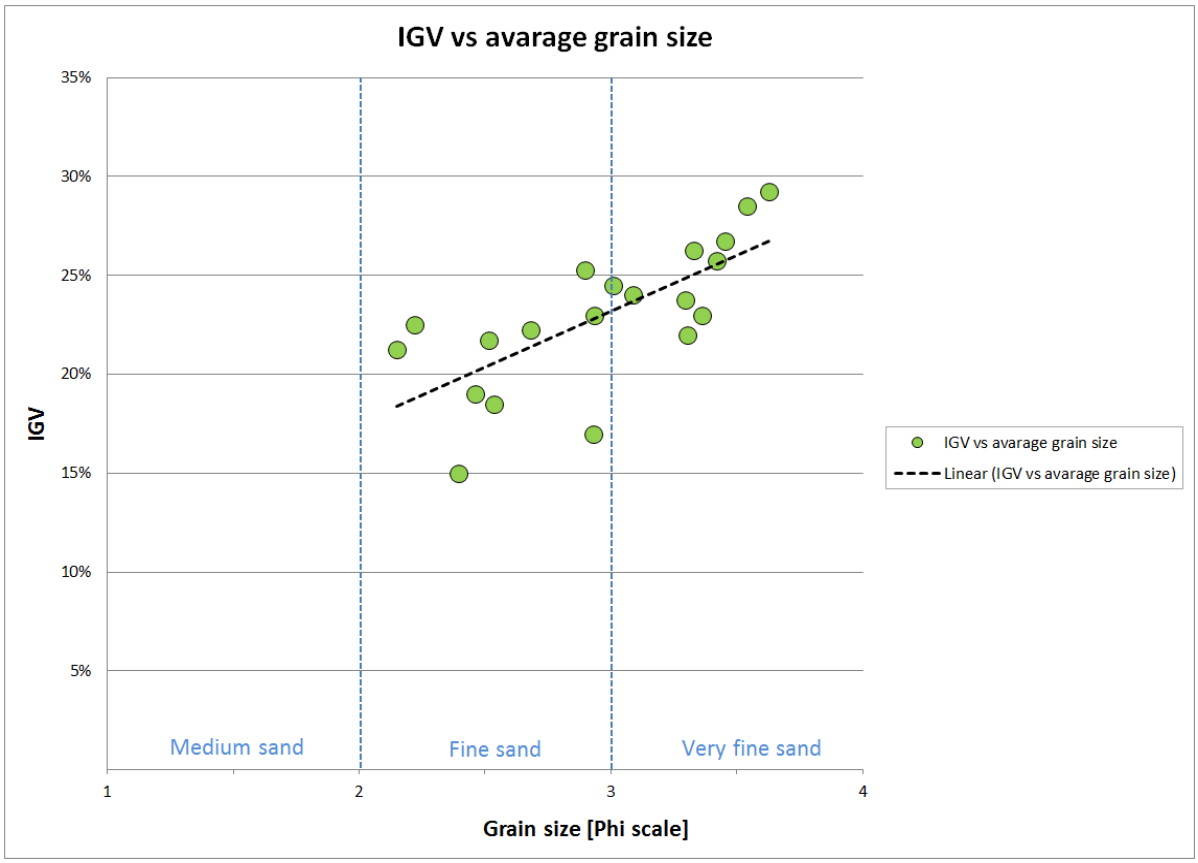

Figure 5.22: The figure shows the predicted IGV results within each thin section (both wells) as function of average grain size.

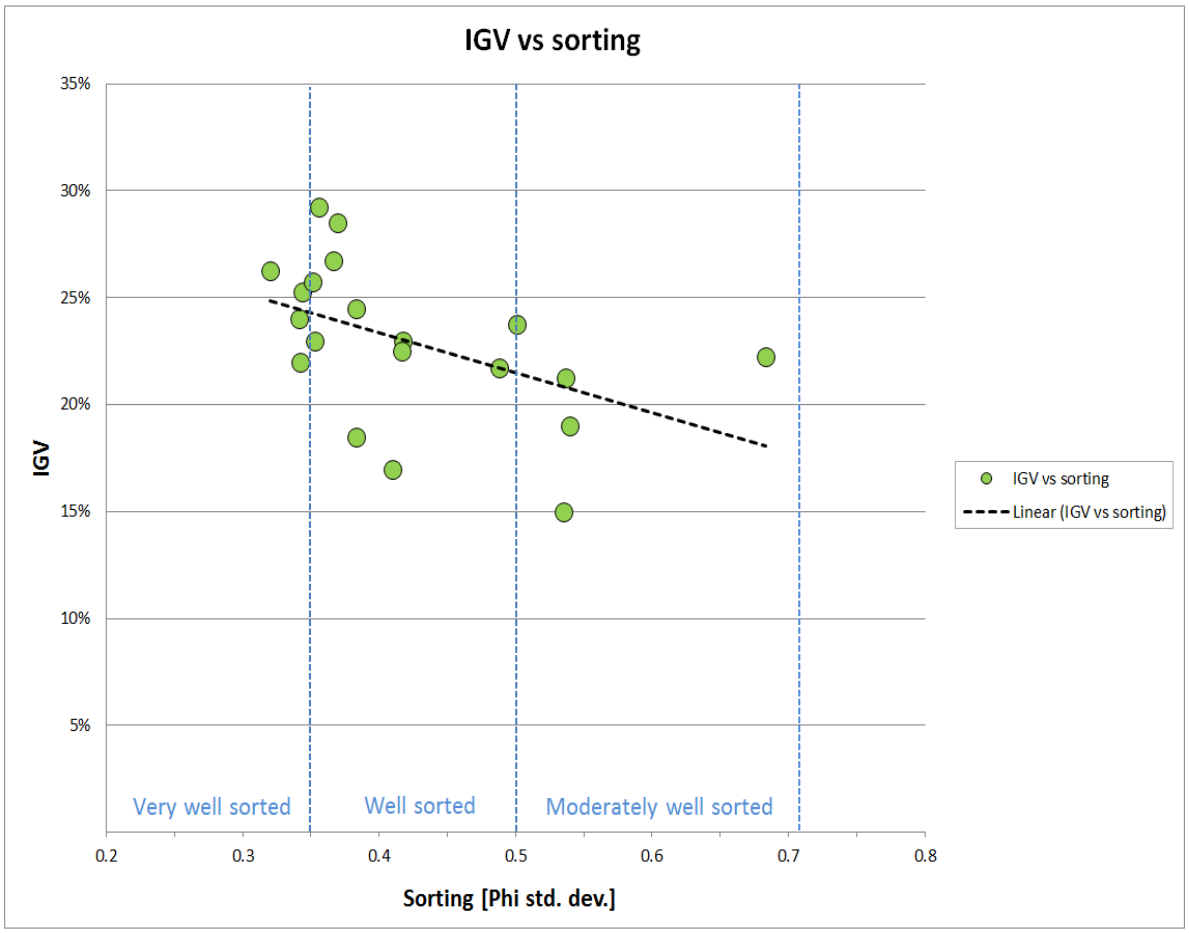

Figure 5.23: The figure shows the predicted IGV results as a function of sorting for all thin sections in both wells.

5.3 Scanning electron microscope and Cathodoluminescence

5.3.1 Quartz cement

The Cathodoluminescence (CL) analyses suggest that significant volumes of quartz cement are present in the Stø formation (Figure 5.24). Due to missing or weak dust rims on the detrital quartz grain surfaces these results indicate that the quartz cement volume has been underestimated during the thin section analysis in the optical microscope (Figure 5.24, A and B). In terms of grain shape, the CL analysis indicate that detrital quartz grains are more rounded than indicated by the optical microscope analyses (Figure 5.24, C and D).

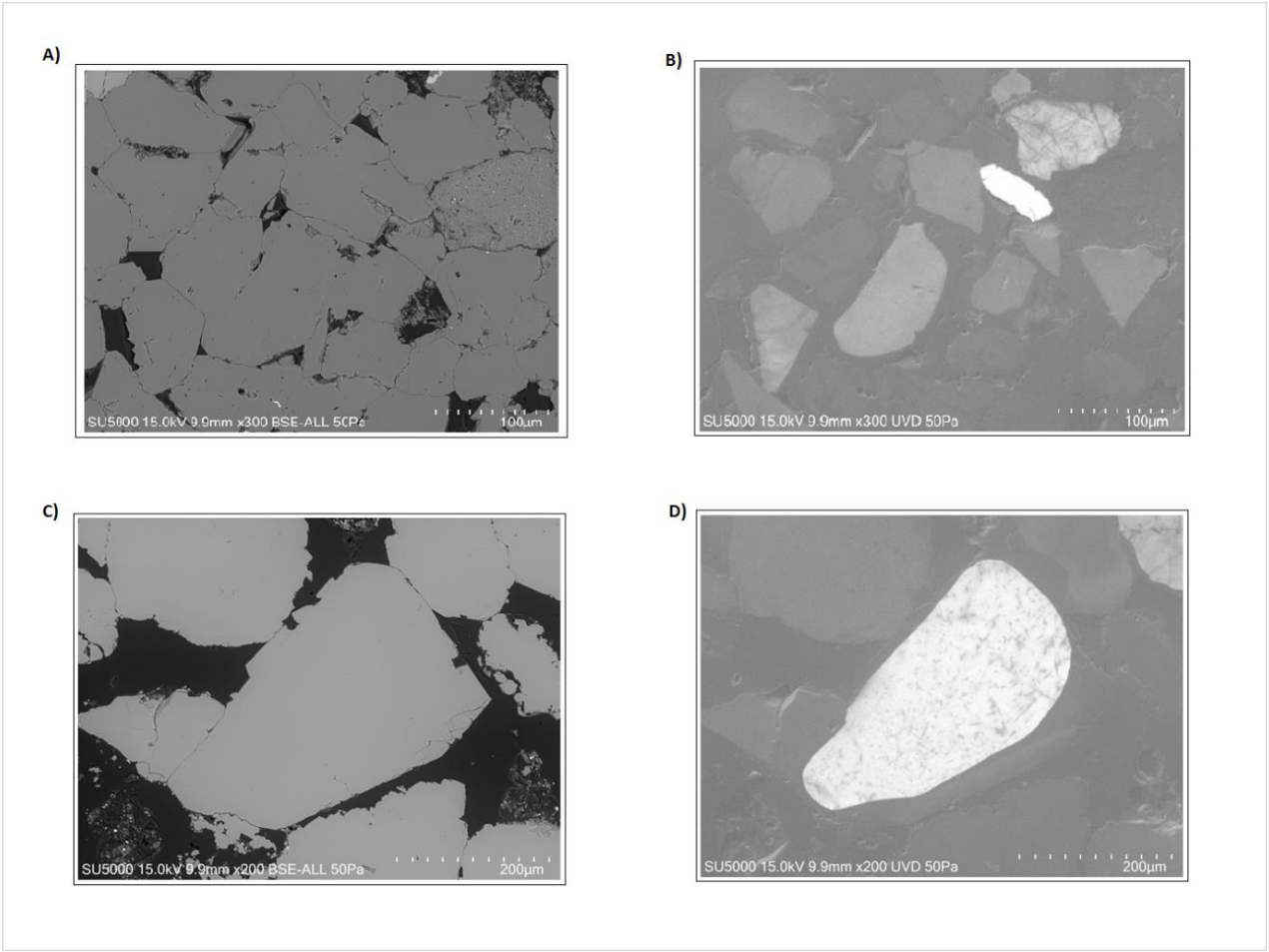

Figure 5.24: The CL analyses indicates that significant amounts of quartz cement are present in the Stø formation. Example A) and B) are from well 7121/5-1, thin-section 3. Example C) and D) are from well 7120/6-1, thin-section 20.

5.3.2 Clay characterization

Three different types of pore filling clay have been recognized during the SEM analysis; pure illite, pure kaolinite and a mixture of illite and microquartz (Figure 5.25). In addition, thin clay laminations have been observed in some of the samples (figure 5.25), which consist of a mixture of illite and muscovite. The content of the pore filling illite and the clay laminated illite and muscovite mixture were not distinguishable in the optical microscope and are thus quantified together in figure 5.27 and 5.28.

The pore filling illite is recognized as relatively pure illite, however, small amounts of zircon, rutile and pyrite was identified in several of the samples. None of these minerals were identified in the pore filling kaolinite cement. The porefilling illite/microquartz mixture can be described as individually microquartz grains or microquartz aggregates encompassed in illite, some of which is observed with a clear grain rim (figure 5.25, C). The thin clay laminations consisting of illite and muscovite (figure 5.26) makes up a significant amount of the observed matrix, if present. Further, these clay laminations were mainly located within the thin sections located in sequence A1 and B1. Pyrite is present in these clay laminations. Small amounts of illite on the detrial quartz grain surfaces were also sporadically observed within intervals beyond clay-rich regions. The illite coating was discontinuous and only present on a minor amount of the detrital quartz grains in each sample.

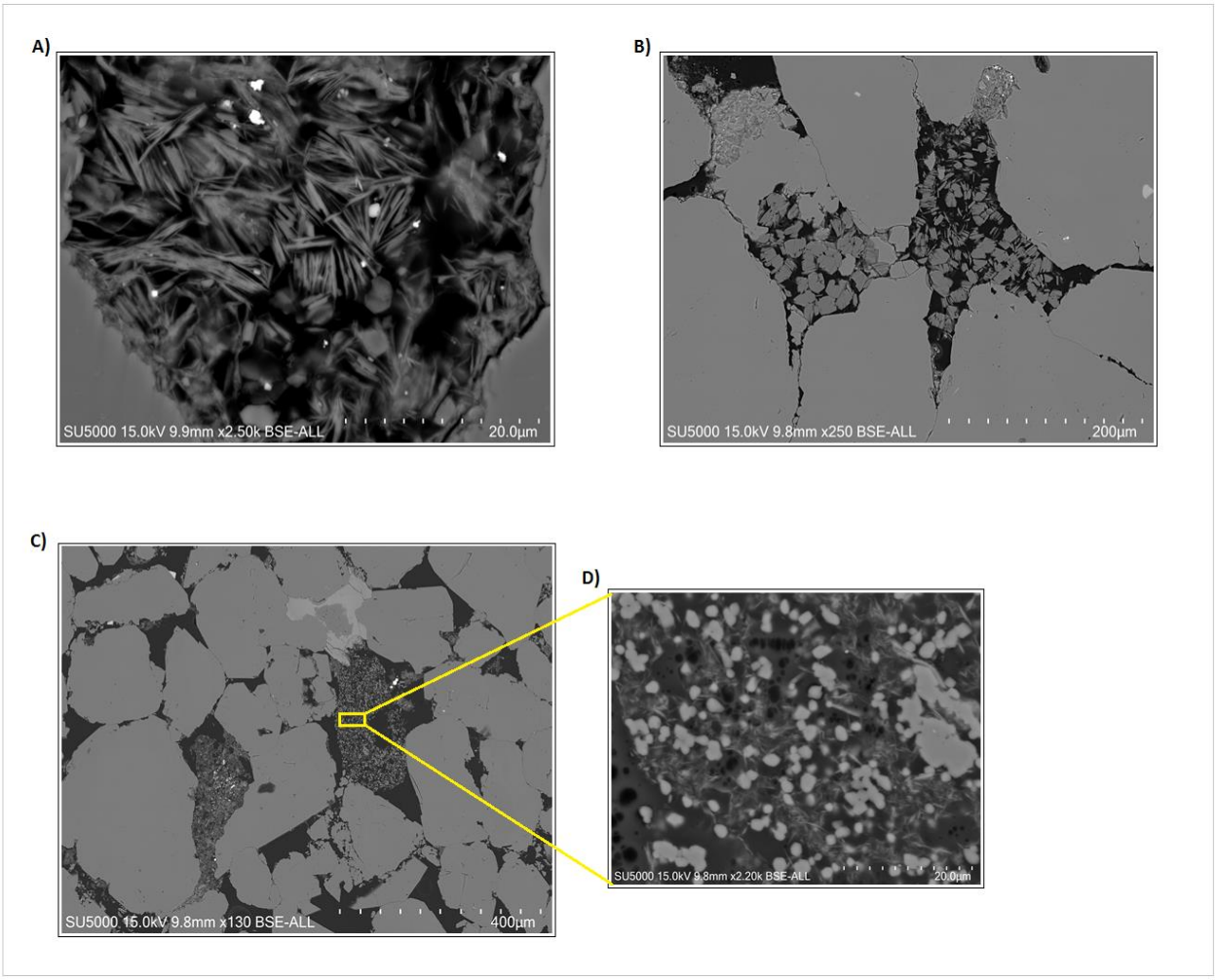

Figure 5.25: The figure shows the three different types of pore filling clay observed in the Stø formation. A) pure illite, B) pure kaolinite and C), D) illite/microquartz mixture. A = 7121/5-1 (3), B=7120/6-1 (20), C and D 7121/5-1 (6).

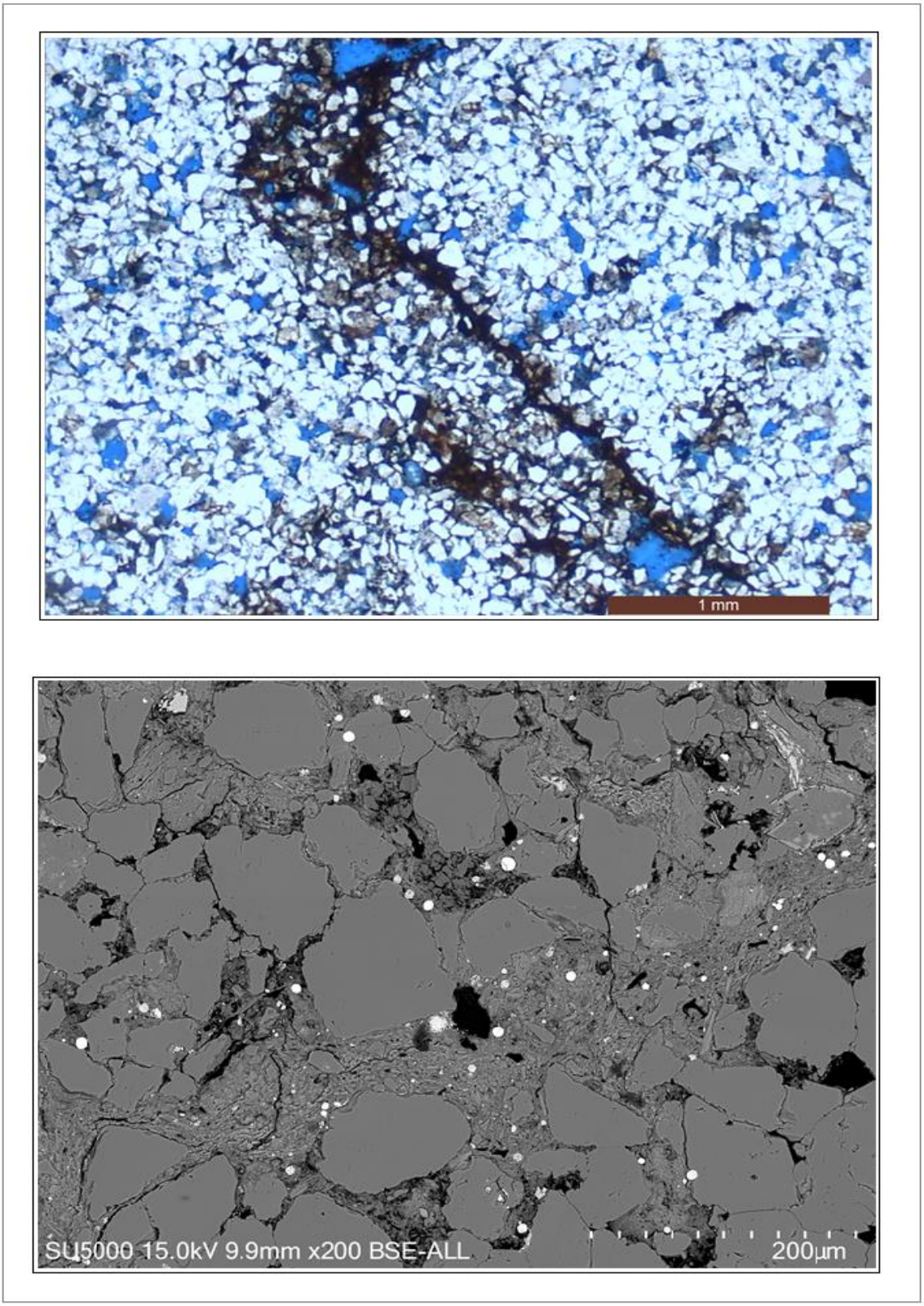

Figure 5.26: The figure shows an example of a thin clay lamination observed in well 7121/5-1 within thin section 3. The upper picture shows such a clay lamination observed in the optical microscope. The lower micrograph shows the same clay lamination, where pyrite can be observed within illite/muscovite mixture.

Below, figure 5.27 and 5.28 summarizes the amounts of the different types of matrix observed within the examined thin sections obtained during the petrographic analysis. No relation is observed between the pure illite and illite/muscovite mixture and the illite/microquartz matrix. However, a trend may be observed between kaolinite and illite. In the majority of the samples containing kaolinite, pure illite and the illite/ muscovite mixture makes up more than 40 % of the total clay volume. In the remaining samples not containing kaolinite, the illite and illite/muscovite mixture accounts for less than 40 % of the clay volume (except in sample 14).

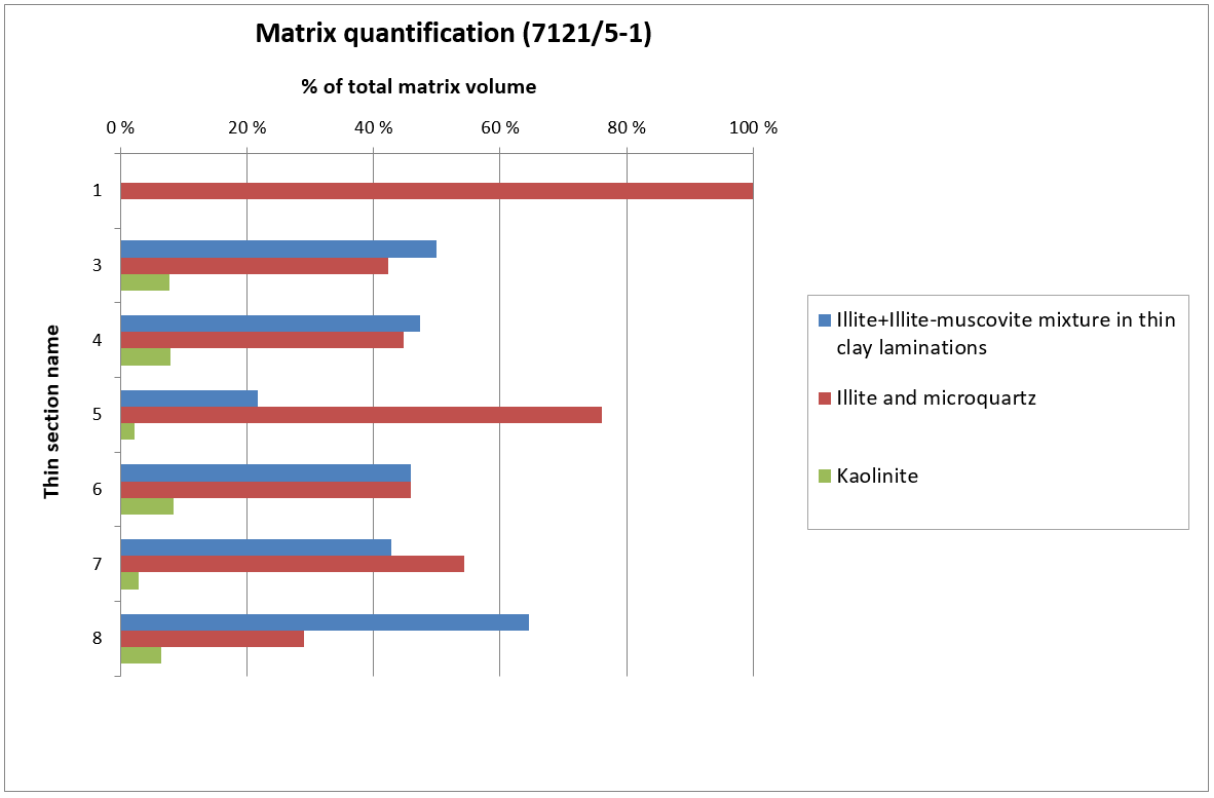

Figure 5.27: The figure shows the amount of different types of matrix observed in the thin sections in well 7121/5-1. The percentages are presented as percentage of the total matrix volume.

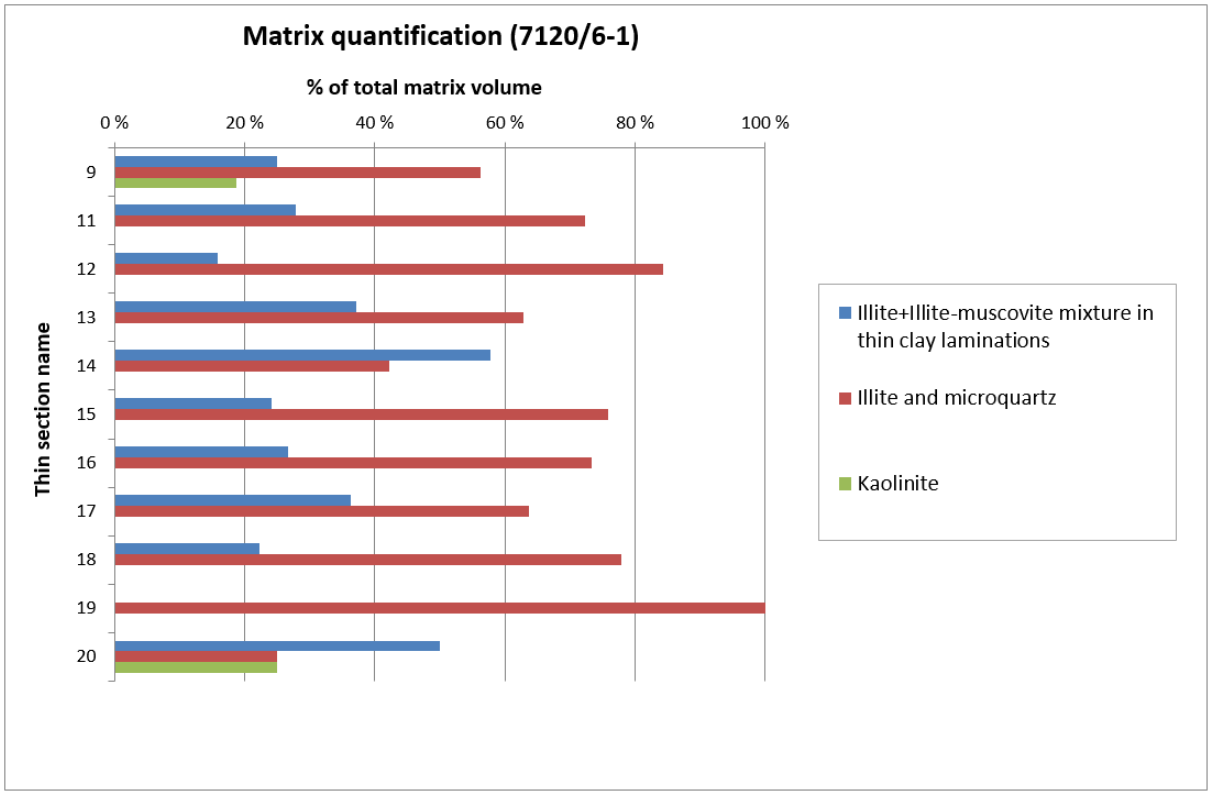

Figure 5.28: Figure 5.25: The figure shows the amount of different types of matrix observed in the thin sections in well 7120/6-1. The percentages are presented as percentage of the total matrix volume.

5.3.3 Other minerals

Minor amounts of pyrite, zircon and rutile where observed during the SEM analysis and as mentioned; these minerals are often located within the pure illite or the illite/muscovite mixture. Further, both small amounts of K-feldspar and albite was observed in the scanning electron microscope (figure 5.29). These minerals were not found during the optical microscope analysis, and hence not quantified. In addition, smaller amounts of dolomite and ankrite were observed. These carbonate minerals were observed together where the ankerite encompasses the dolomite and further fills in the neighboring pore spaces (figure 5.30).

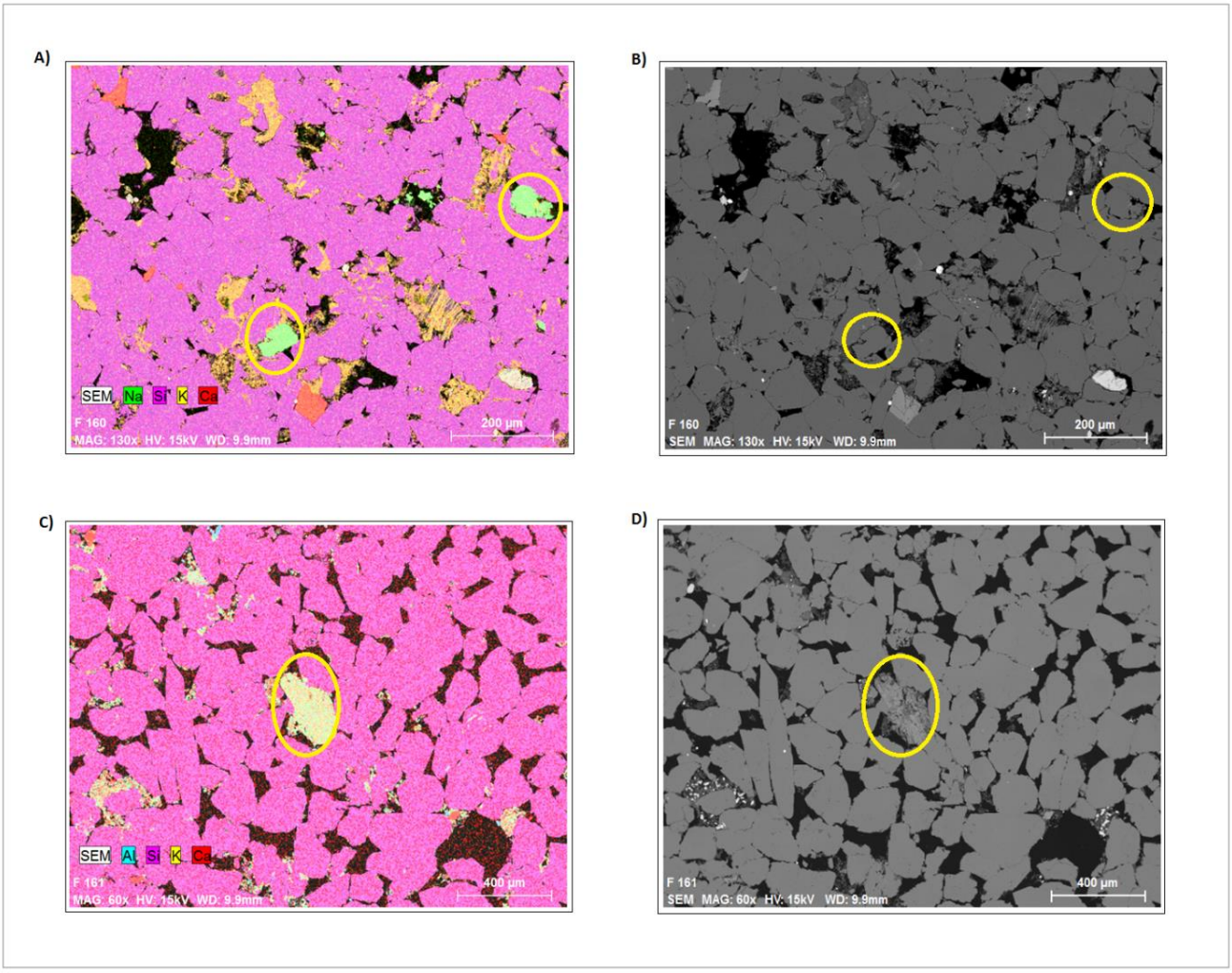

Figure 5.29: Both albite (A) and K-feldspar (B) were observed during mapping in the SEM. B) and D) shows the micrographs of the mapped area and displays how difficult, especially the albite, it is to separate from the quartz grains. All the micrographs are from well 7121/5-1 (3).

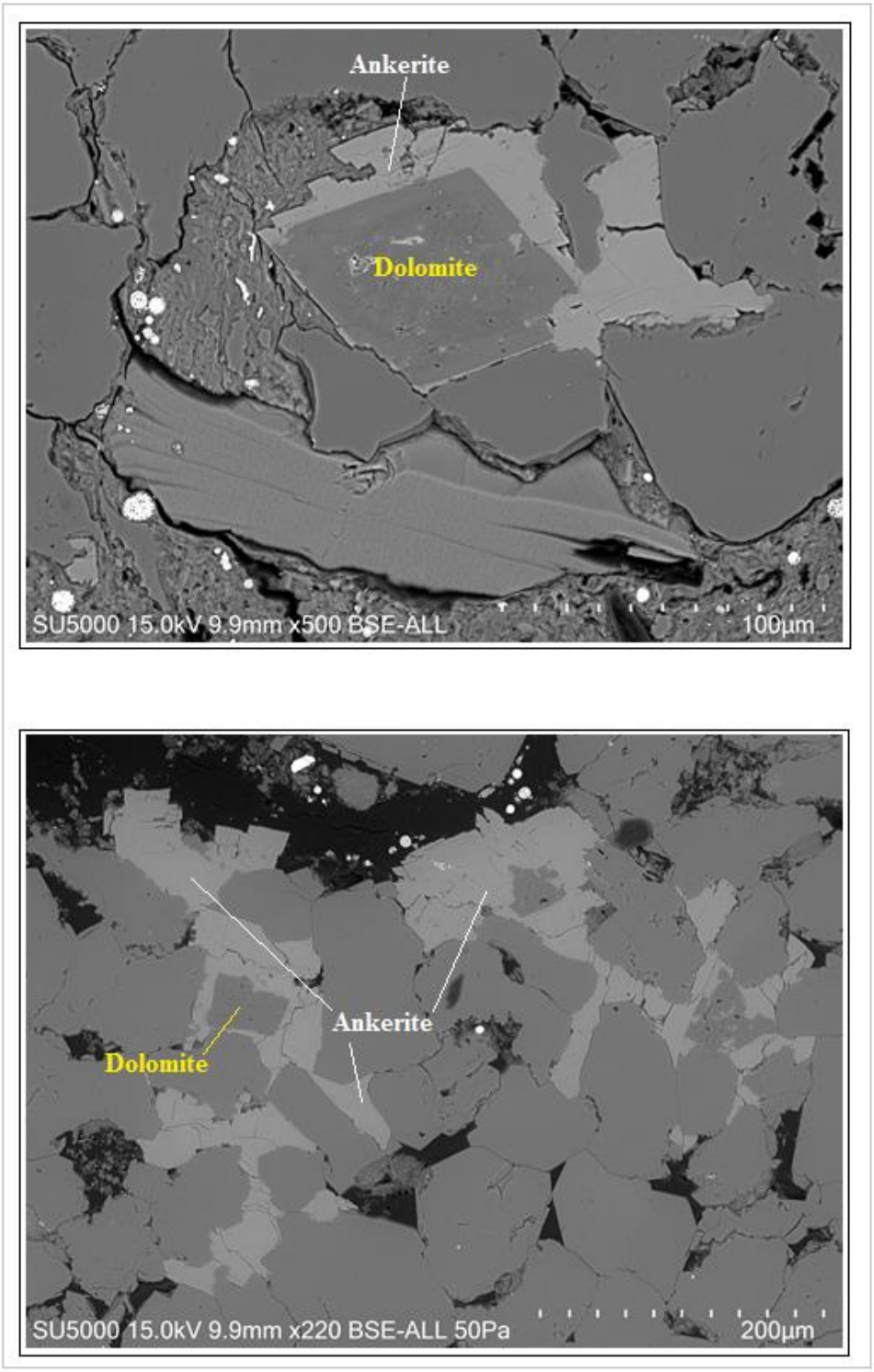

Figure 5.30: The figure shows two examples of dolomite and ankerite observed in thin section 3 from well 7121/5-1.

6. Petrophysical analysis

6.1 Introduction

The main purpose of the petrophysical analysis is to get an overview of the Stø formation and recognize intervals with similar properties. This includes lithology description, porosity- and quartz cement estimation. By comparing the results with the observed thin section analysis, there may be a possibility to recognize similar intervals beyond the sample depth investigated during petrographic analysis. In addition, the geophysical well logs were used to recognize compaction trends. This is important in order to understand diagenetic processes in the study area, which subsequently will influence the reservoir quality of the Stø formation. From the literature, several predictions regarding uplift in the SW Barents Sea has been described, and an uplift estimation will be presented at the end of this chapter.

6.2 Results

6.2.1 Lithology characterization

6.2.1.1 Gamma log

In figure 6.1, the gamma log response of the Stø formation is displayed for both wells. The Stø formation is 84 and 76 m thick in well 7120/6-1 and 7121/5-1, respectively. The distance between the wells is about 16,8 km and the Stø formation lies approximately 23 meters deeper in well 7120/6-1. The Stø formation stands out as an interval with a very low gamma response in comparison with the overlying Fuglen- and Hekkingen formations. From the top of the underlying Nordmela formation, an upwards fining trend can be recognized within the Stø formation in both wells. The lower part, from 2445 – 2406 m and 2469 – 2426 m in well 7121/5-1 and 7120/6-1 respectively, appears to be very clean where consistently low API values characterizes this interval. From the top of this interval and up towards the top of the Stø formation, a general increase in API values can be recognized. In addition, there are regions within the upper part of the Stø formation with an increased gamma response compared to the background response. In well 7121/5-1 a thin interval with a similar gamma response as the lower part of the Stø formation can be observed in uppermost part of sequence A1. The upper/lower intervals correspond to sequence A1/A2 and B1/B2 in well 7121/5-1 and 7120/6-1, respectively (see section 4.2). Moreover, the gamma ray response is generally

lower in well 7121/5-1 where API values around 15 in the lower part is common. API values at the corresponding interval in well 7120/6-1 displays values in the range of 45-50. A full-range gamma ray distribution from the Stø formation in both wells can be seen in figure 6.2.

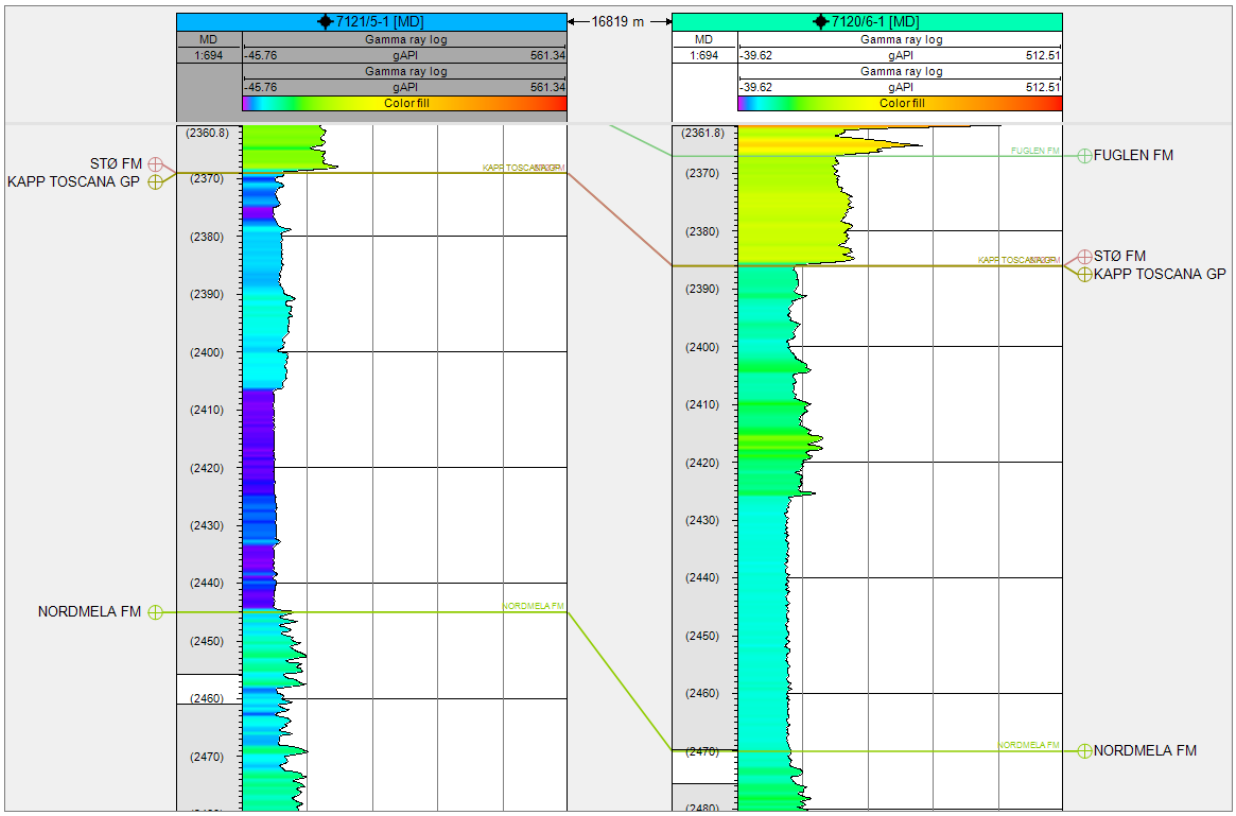

Figure 6.1: The figure shows the gamma ray log for both wells examined in this study, through the Stø formation. Two different intervals based on the gamma ray response may be observed. A lower interval where the response is very consistent and an upper interval where the API values fluctuates more.

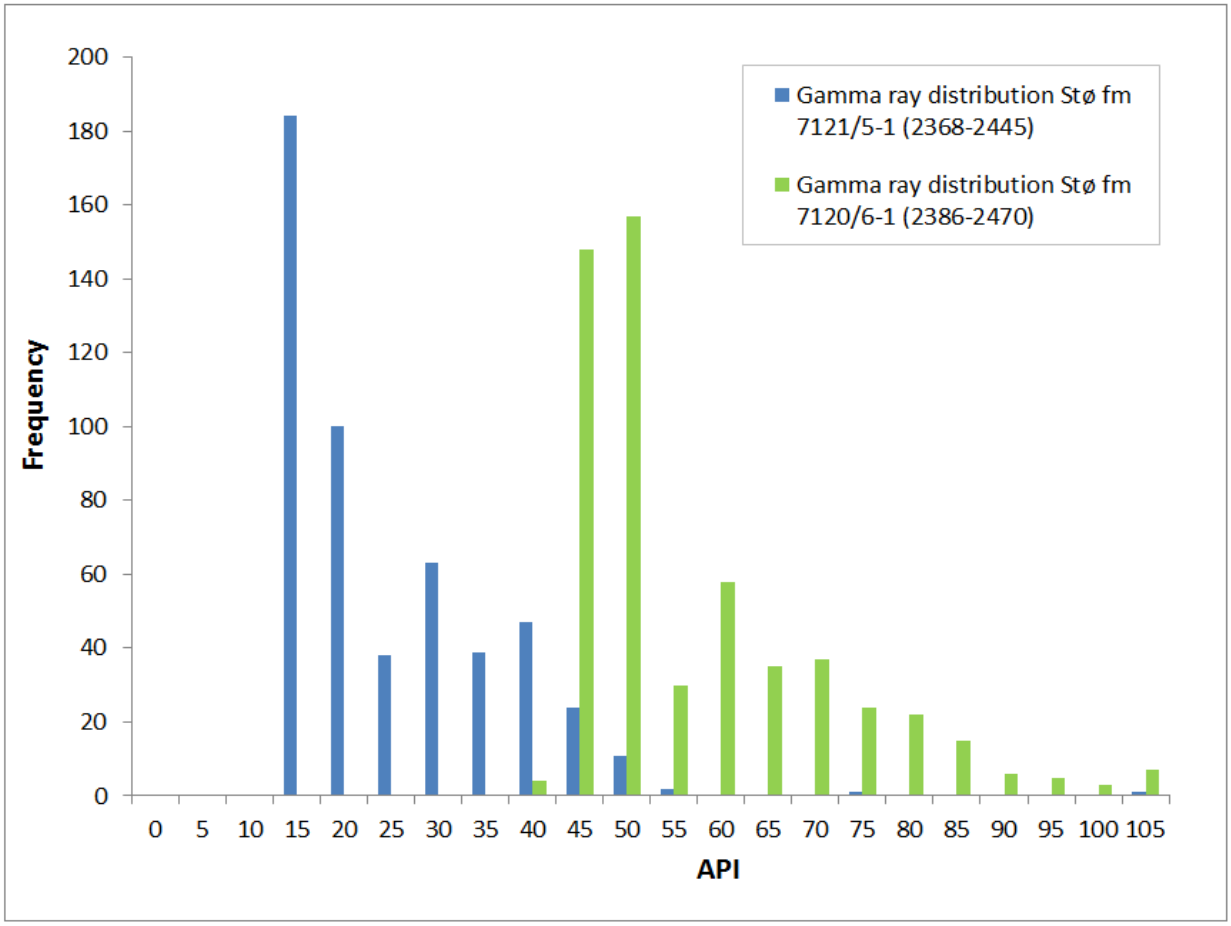

Figure 6.2: The figure displays the gamma ray distribution within the Stø formation in both wells.

6.2.1.2 Density log

The density logs (figure 6.3) shows the same trends as the gamma ray log. The upper part of the Stø formation differs from the lower part, where densities are generally higher in sequence A1 and B1. Sporadically, densities above 2,5 g/cm^3 appears as thin stringers within these sequences, especially in sequence B1 (7120/6-1) where they appear at depth of 2413, 2415 and 2417m (MD from KB). The uppermost part of sequence A1 in well 7121/5-1 shows a density response similar to the lower sequence B2. In addition, a thin stringer can be observed in lower part of sequence A2 (7121/5-1). From figure 6.3, B, sequence B2 appears as a consistent interval in terms of densities.

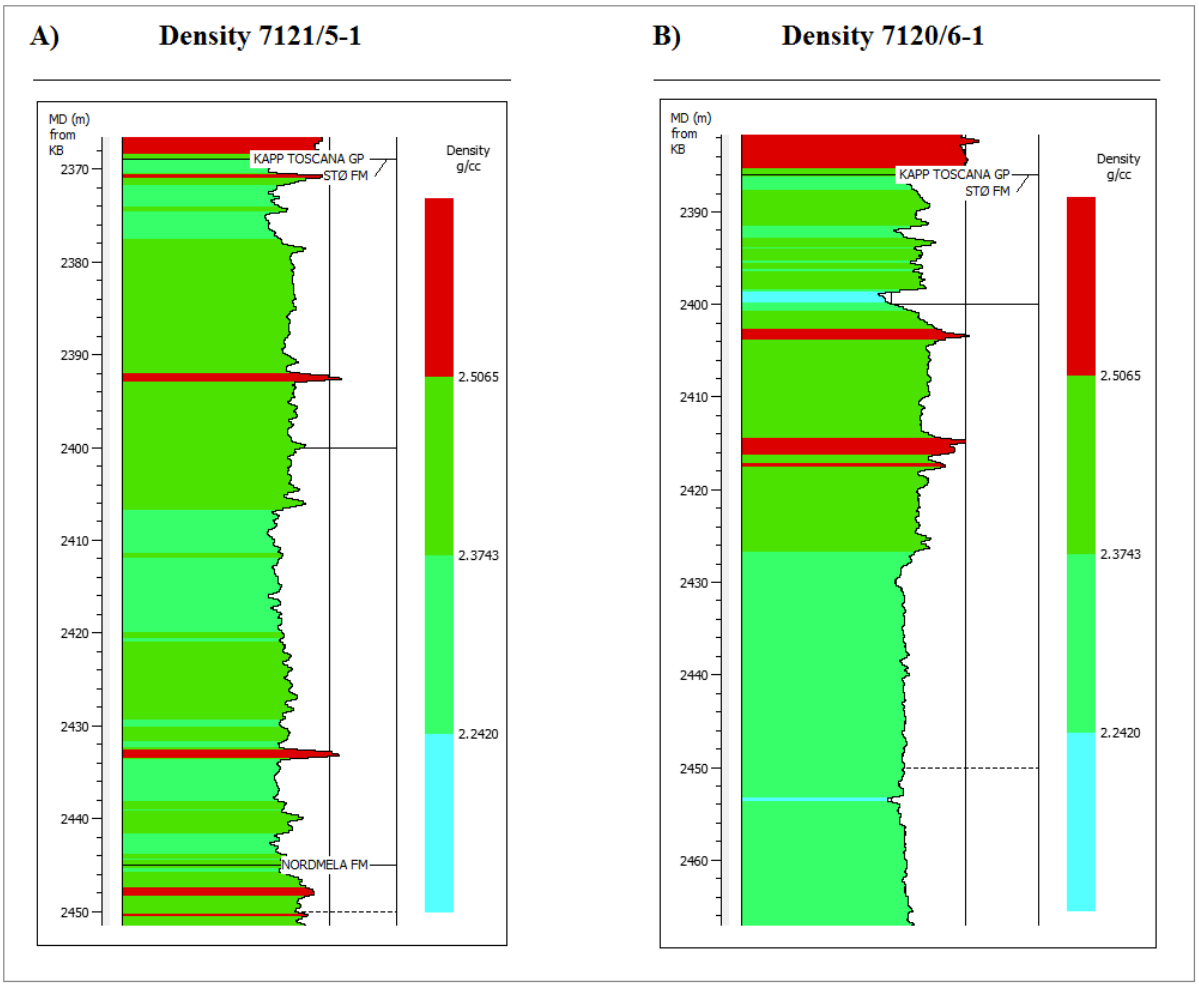

Figure 6.3: The figure displays the density logs from both wells within the Stø formation. The density logs shows that high density intervals appear as thin stringers within the Stø formation, commonly located in upper sequences (A1 and B1).

6.2.1.3 Shale volume estimation

The predicted shale volume for both wells is presented in figure 6.4. The results suggest that the shale volumes are highest in sequence A1 and B1. Further, the highest estimated shale volumes are located within sequences where the depth corresponds to the highest responses from the density log in figure 6.3. Again, in the uppermost part of sequence A1 within the Stø formation in well 7121/5-1, the shale volume displays similar values to the lowermost sequence. The lower sequences of the Stø formation, A2 and B2, shows very low responses in terms of shale volume (< 5%) and a constant response can be recognized through this interval.

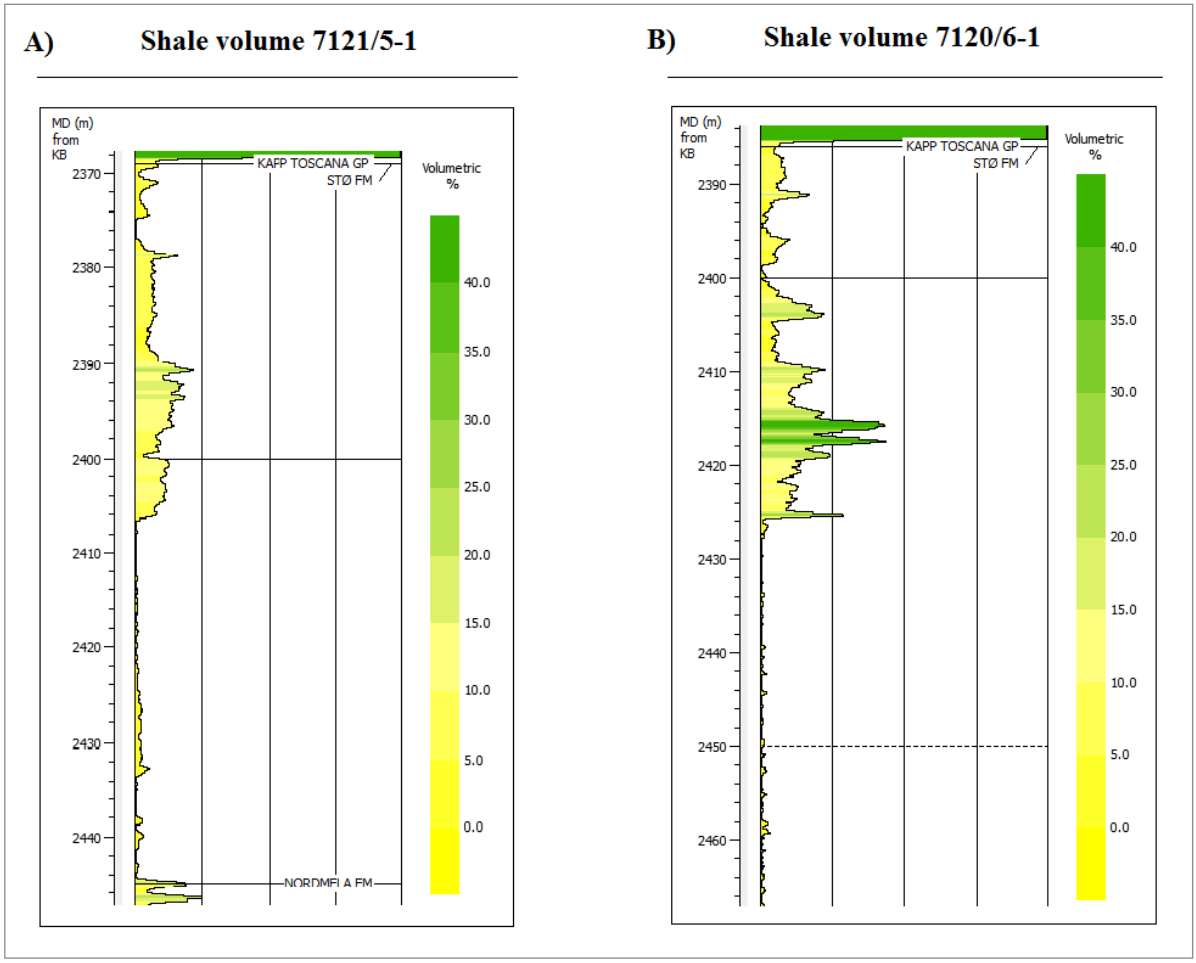

Figure 6.4: The figure displays the estimated shale volume from both wells within the Stø formation.

6.2.2 Porosity estimation

Figure 6.5 and 6.6 displays the calculated- and observed porosity within the Stø formation in well 7121/5-1 and 7120/6-1. Generally, the same trend can be recognized in the observed- and calculated porosity while the highest porosity values derive from the calculated porosity. In well 7121/5-1 the boundary between sequence A1 and A2 can be recognized at approximately 2408 meters where the porosity increases in the upper most part of sequence A2, before a porosity decrease is indicated from both approaches (figure 6.5). The interval with the highest porosity estimation can be recognized in well 7120/6-1 below 2430 meters which corresponds to sequence B2. This is indicated both by the observed and calculated porosity. Above this interval, sequence B1 can be recognized as an interval with highly varying porosity values within relatively short distances. This is also the interval with the most significant disagreement between the observed- and calculated porosity at some levels. At approximately 2408 and 2422 meters the calculated porosity increases while the observed porosity decreases (figure 6.6). A significant deviation can also be observed in sequence in A1 (7121/5-1) at depth of 2372 meters. Based on the calculated porosity, a porosity distribution plot is presented in figure 6.7. For well 7121/5-1, the majority of the calculated porosity values lies within the range of 12-17%. In well 7120/6-1 a significant amounts of the data falls in to the same range as in well 7121/5-1, but a substantial amount of the porosity values is located within the 17-19% range. From figure 6.6, it becomes evident that these values mainly represent the porosity values from sequences B2.

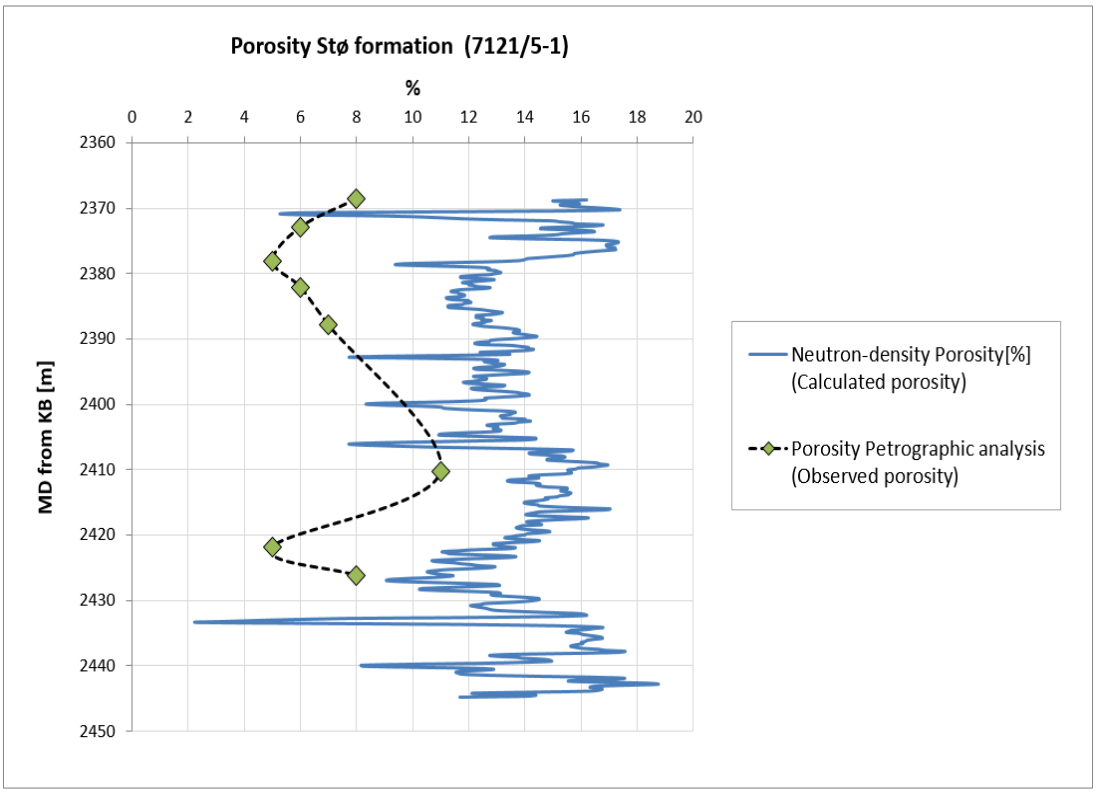

Figure 6.5: The figure shows the calculated- and observed porosity within the Stø formation in well 7121/5-1. The calculated porosity equals the total porosity (neutron-density porosity).

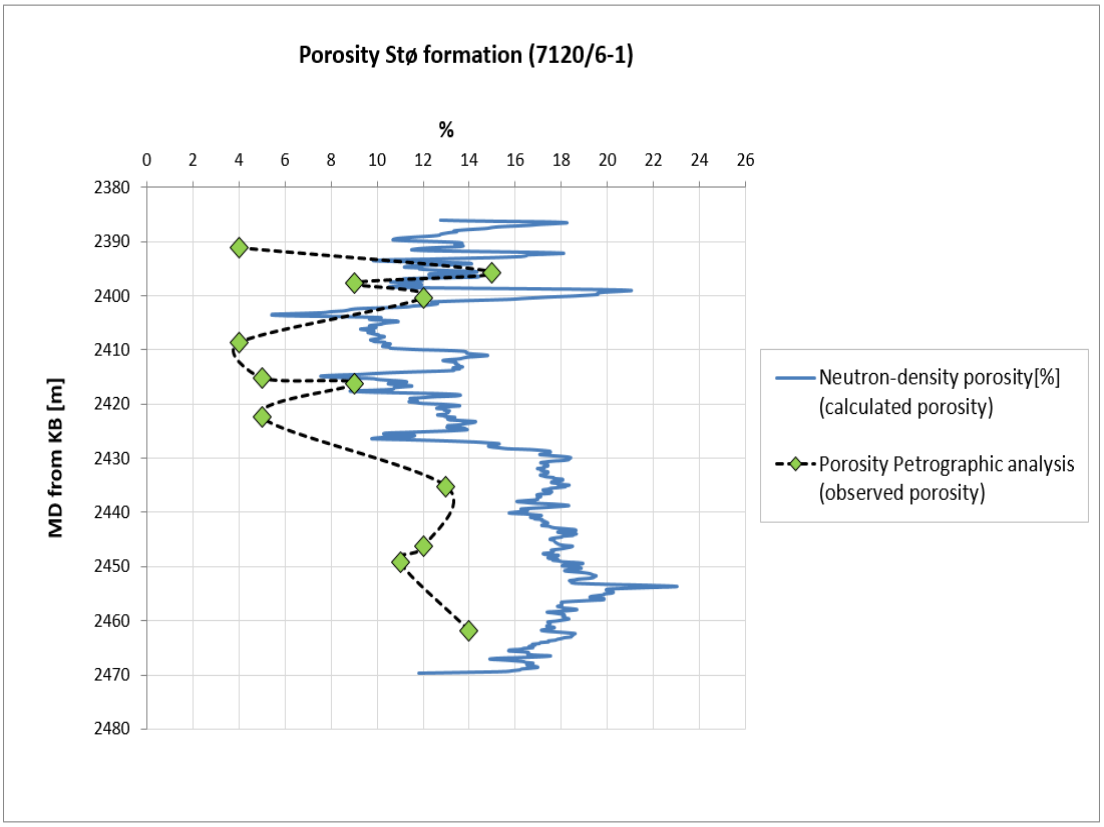

Figure 6.6: The figure shows the calculated- and observed porosity within the Stø foramtion in well 7120/6-1. The calculated porosity represents the total porosity.

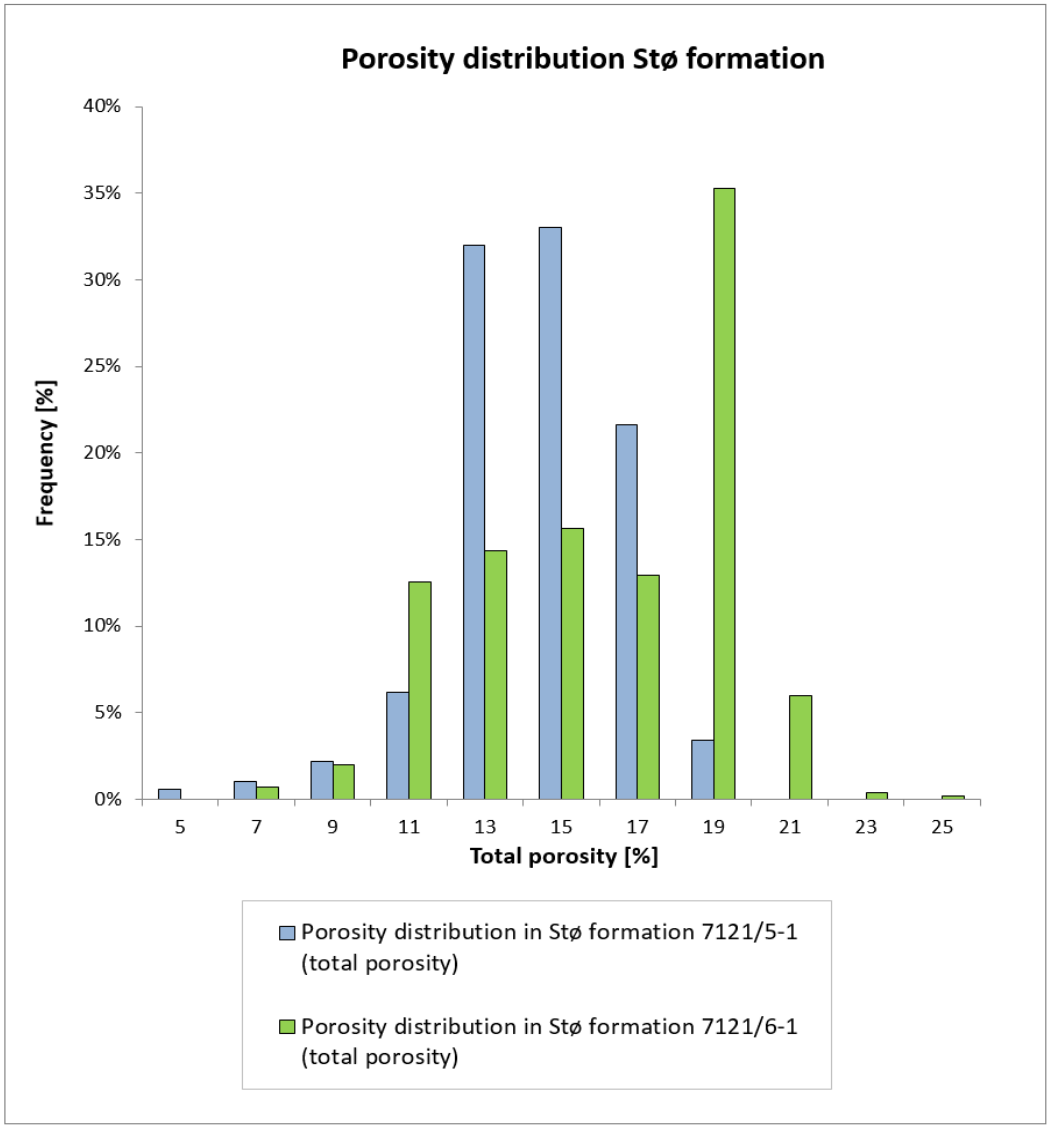

Figure 6.7: The figure displays the porosity distribution within the Stø formation from both wells.

6.2.3 Cement volume estimation

In figure 6.8 and 6.9 the quartz cement volume is plotted against depth in both wells, where also the corresponding observed quartz cement volume is presented. There is a fairly good correlation between the observed and calculated quartz cement volume in well 7121/5-1, yet the calculated values indicate a higher cement volume. In well 7120/6-1 the observed- and calculated cement volume correlates somehow down to approximately 2420 m where a significant discrepancy can be observed. The calculated cement volume indicates an increase with depth through this interval (corresponds to sequence B2), whereas the observed quartz cement volume indicates significantly lower cement volume.

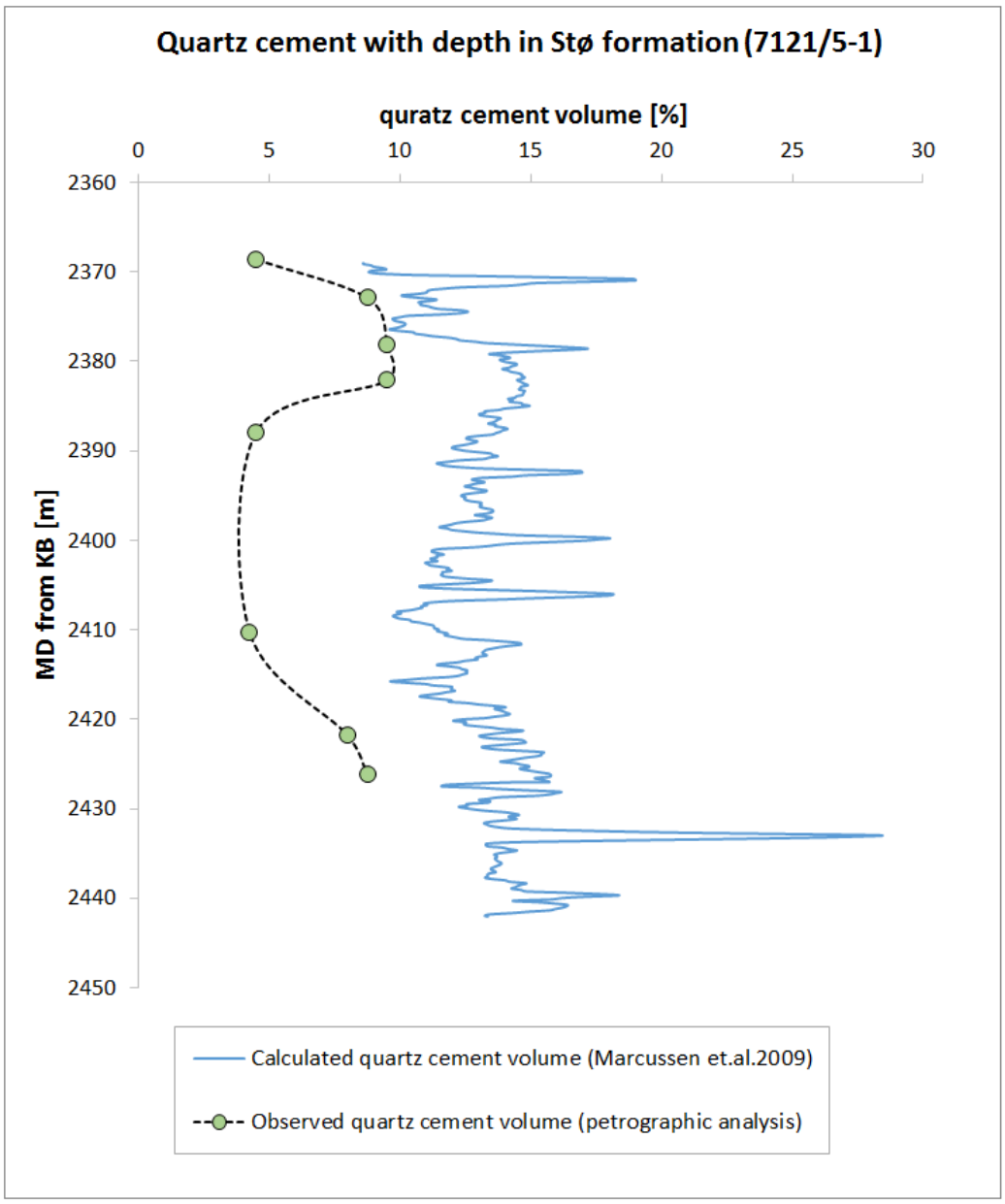

Figure 6.8: The figure displays the predicted- and observed quartz cement volume within the Stø formation in well 7121/5-1.

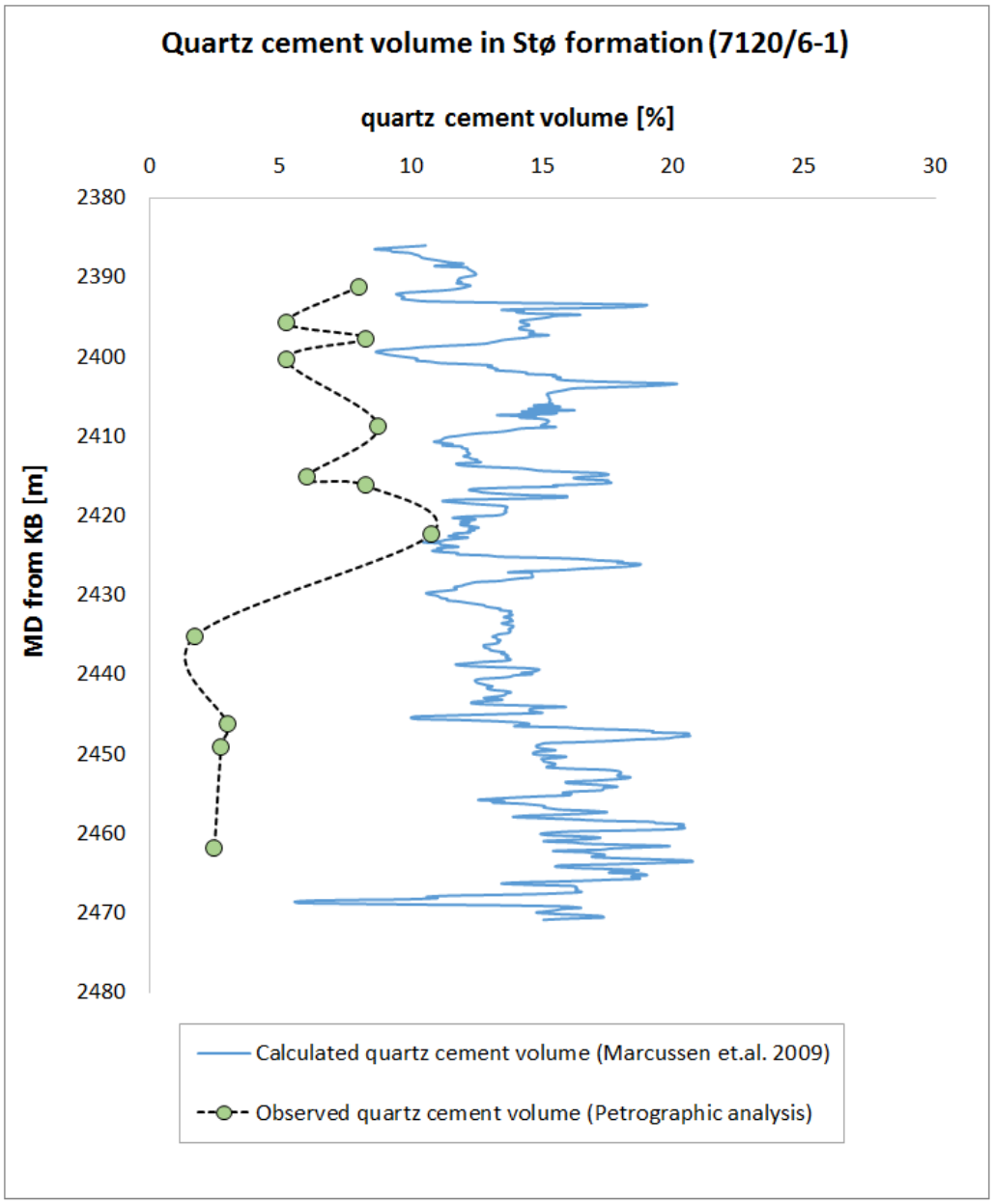

Figure 6.9: The figure displays the predicted- and observed quartz cement volume within the Stø formation in well 7120/6-1.

6.2.5 Compaction

6.2.5.1 Geothermal gradient

Figure 6.10 displays the calculated linear geothermal gradient in well 7121/5-1 and 7120/6-1. As the wells are located close to each other, there is not much deviation between the geothermal gradients. The present day temperature development with depth may suggest an onset of quartz cementation and illitization from K-feldspar and kaolinite at a depth of approximately 2000 m and 3600 m, respectively. Significant amounts of altered illite from smectite would most likely have occurred at temperatures above 80-100°C, and this would correspond to a depth of about 2700 m.

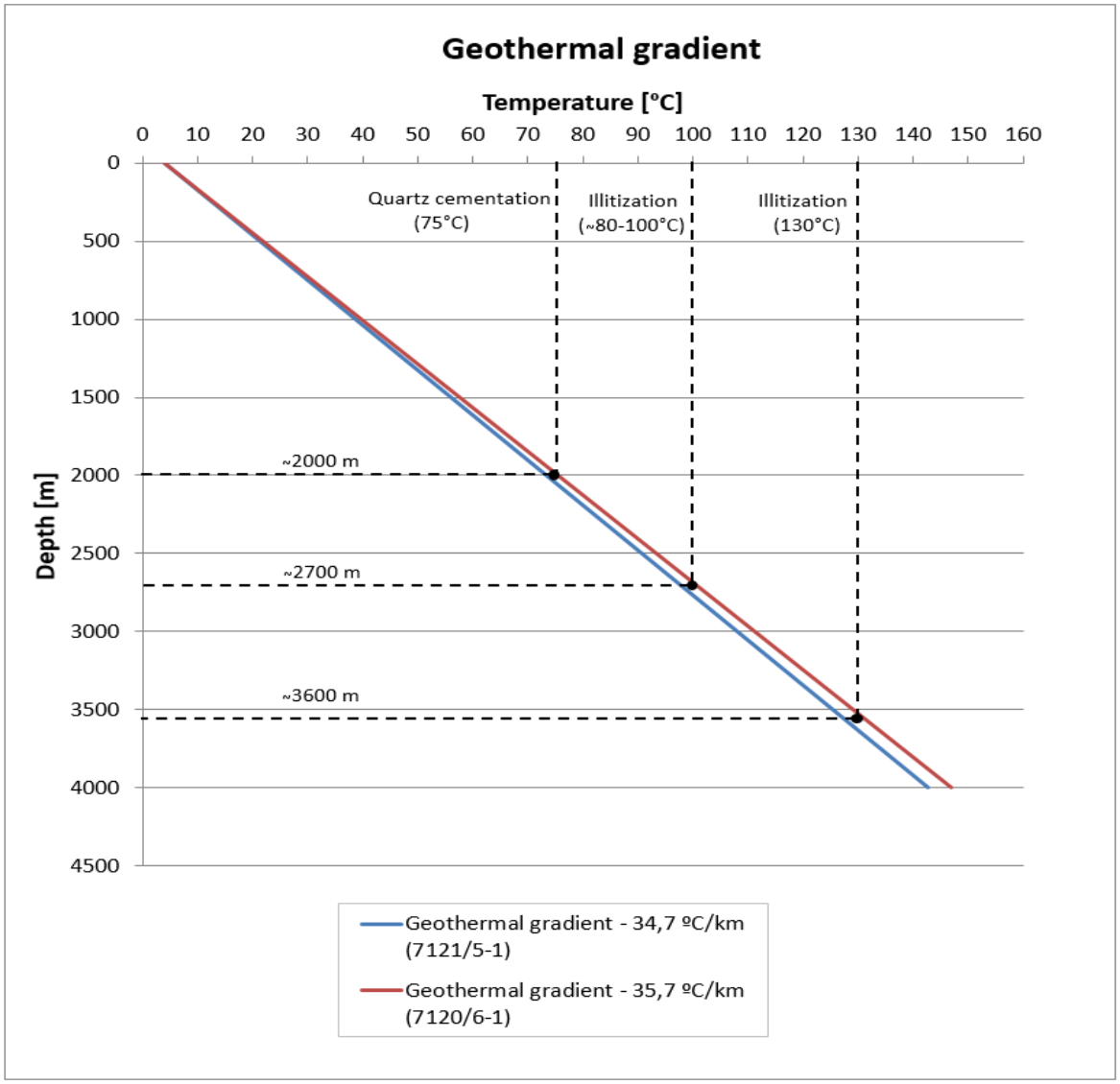

Figure 6.10: The figure shows the theoretically onset of quartz cement, Illitization from smectite and illitization from K-feldspar and kaolinite as a function of the calculated geothermal gradient (present day temperature).

6.2.5.2 P-wave velocity and density with depth

The P-wave velocity trends are quite similar in both wells, where they start just above 2000 m/s and reaches 4500 m/s at about 2800 and 2450 meters in well 7121/5-1 and 7120/6-1, respectively (Figure 6.11, A and C). Two abrupt increases in velocity can be recognized in each well. In well 7121/5-1 one can be seen at approximately 1200 meters depth and another is seen at about 2000 meters (Figure 6.11, A). For well 7120/6-1 the same velocity increases can be recognized. The velocity increases at 2000 meters in both wells are characterized by a decrease in velocity prior to the increase. The density logs (Figure 6.11, B and D), shows an increase in density at the corresponding level for the shallowest velocity increase (~1200 meters) described above. This cannot be recognized in deepest velocity increases, where densities are lower (D) or more or less constant (B) through the lowermost interval (i.e., ~ from 2000m).

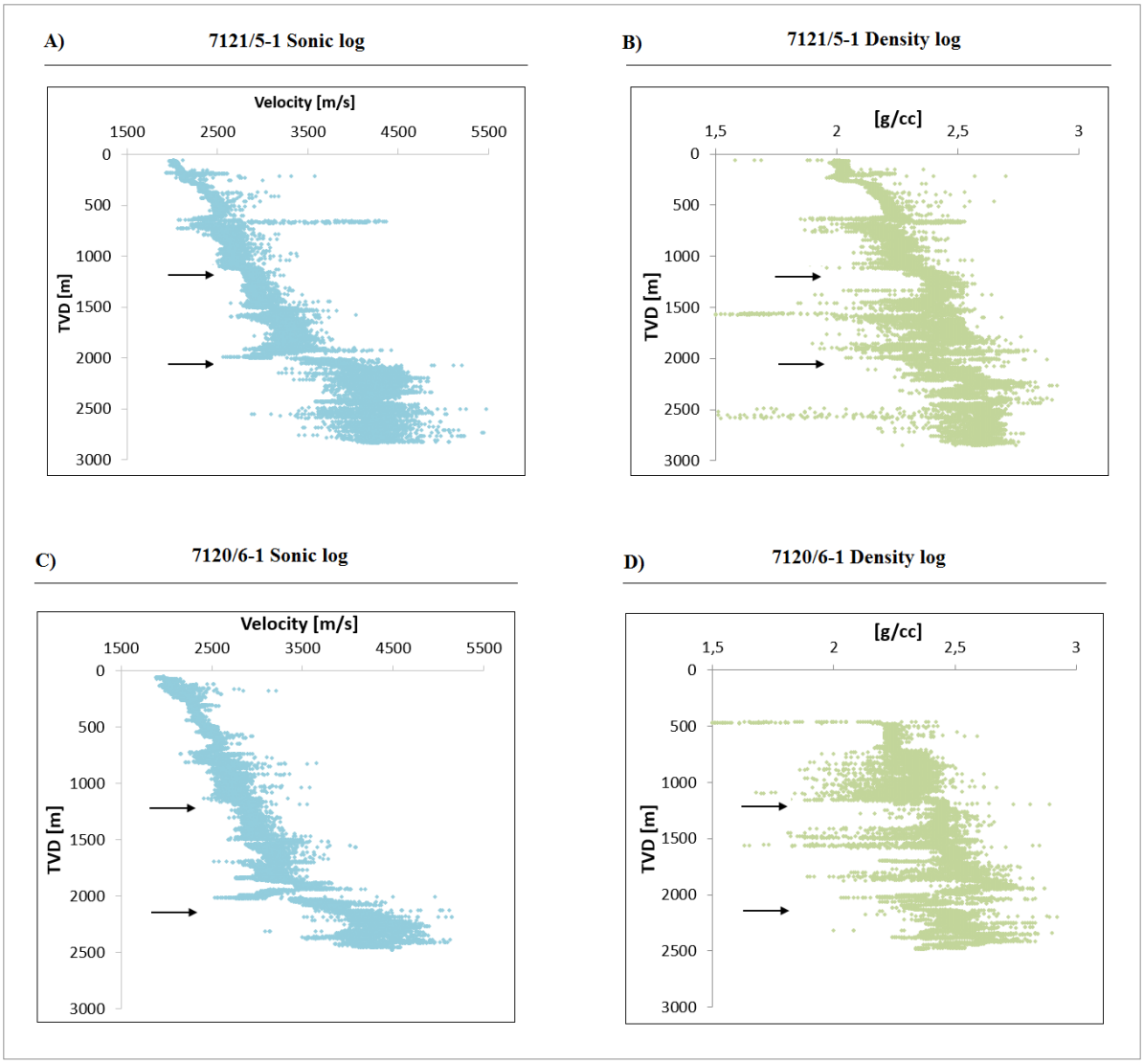

Figure 6.11: The figure displays the sonic- and density logs in well 7121/5-1 and 7120/6-1.

6.2.5.3 P-wave vs total porosity

Figure 6.12 and 6.13 shows the Stø formation plotted against the P-wave and total porosity. Regarding the P-sonic log, the Stø formation plots between 3500 m/s – and 4000 m/s in both wells whereas the majority of the porosity values lies within the 8-18% range. A separation can be observed with in well 7120/6-1, where some of the data plot closer to the contact cement model. In figure 6.14, a cross section through the Stø formation shows where the highlighted data-points in well 7120/6-1(figure 6.13) are located. This indicates that the separation of the data-points corresponds to a separation of sequence B1 and B2. Further, in terms of sorting, the separation may represent a difference in sorting at the time of deposition. In well 7121/5-1, all the data plots just above the lowermost diagenetic bound. All the data in both wells follow the diagenetic cementing models, which from a rock physics point of view indicate that the Stø formation is cemented.

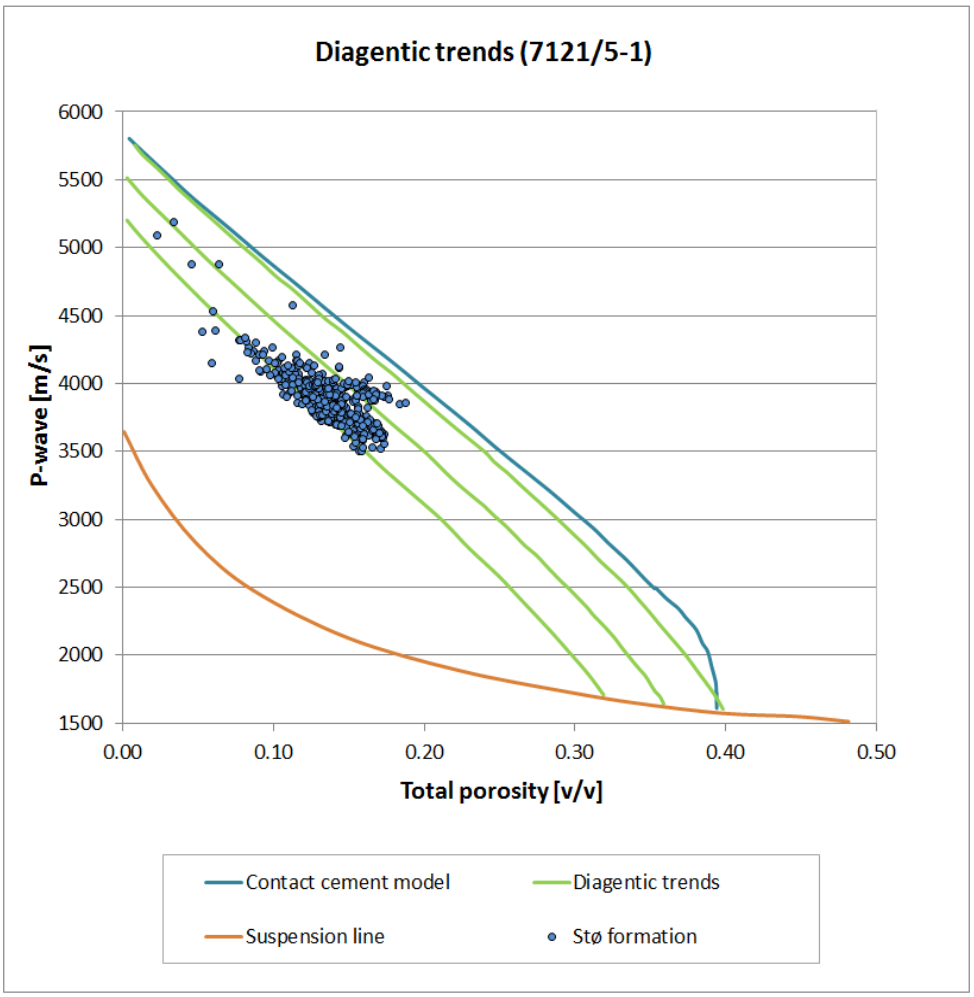

Figure 6.12: The figure displays the Stø formation (well 7121/5-1) as function of P-wave and total porosity where the results are compared with various digitized diagenetic trends. The contact cement model after (Dvorkin and Nur, 1996), diagenetic trends for various sorting (critical porosity) after (Avseth et al., 2005) and the suspension line which corresponds to Reuss

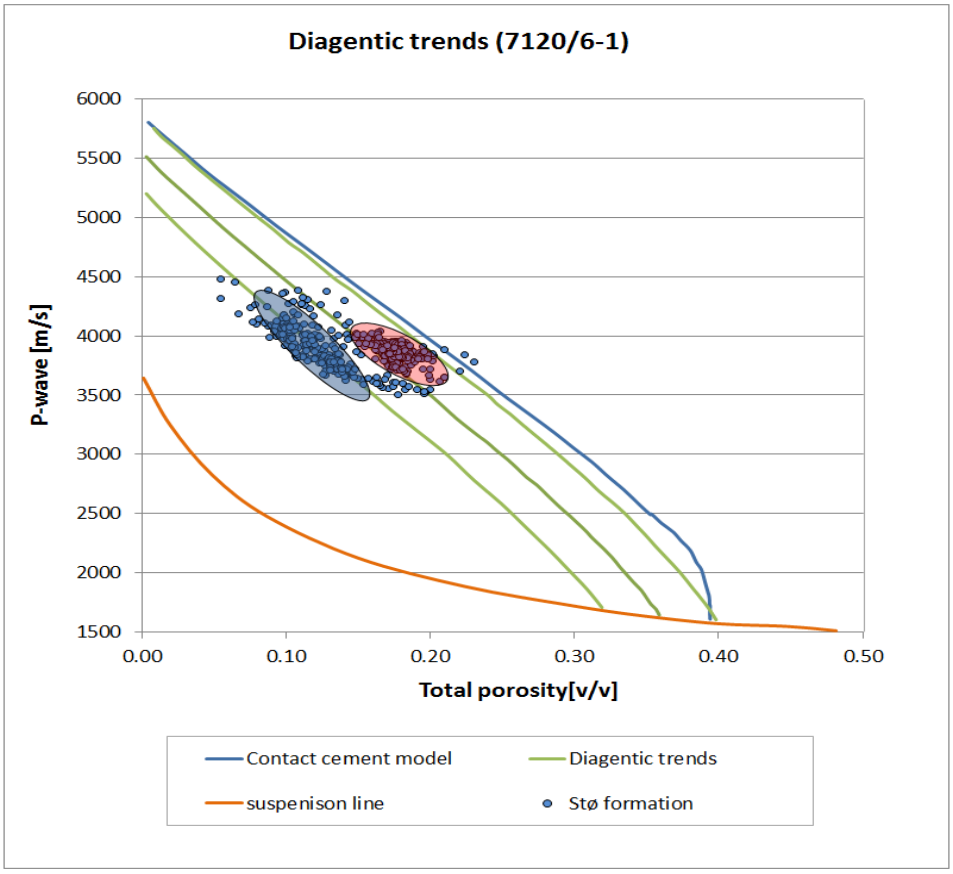

Figure 6.13: The figure displays the Stø formation (well 7120/6-1) as function of P-wave and total porosity where the results are compared with various digitized diagenetic trends. The contact cement model after (Dvorkin and Nur, 1996), diagenetic trends for various sorting (critical porosity) after (Avseth et al., 2005) and the suspension line which corresponds to Reuss bound.

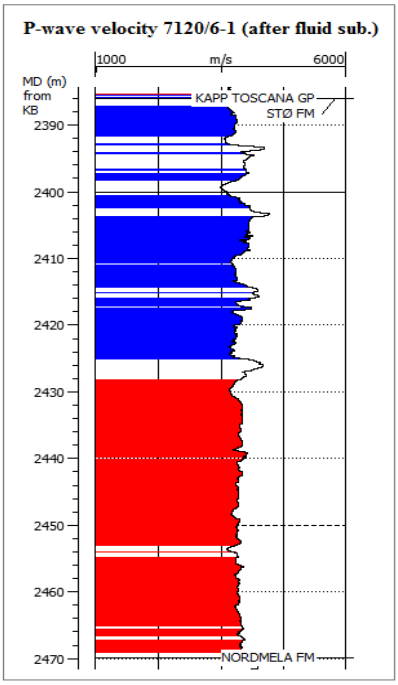

Figure 6.14: A cross section through Stø formation, showing the location of the highlighted points in figure 6.13.

6.2.6 Uplift estimation

The estimated uplift results for both wells can be seen in figure 6.15. The results suggest that this area has been uplifted approximately 1000 meters . This indicates that the Stø formation, prior to uplift, has been subjected to a depth of approximately 3000 - 3100 meters in both wells. Temperature estimates based on the geothermal gradient presented in figure 6.10, are shown in table 6.1. The present day temperature at the top of the Stø formation has been estimated to 69.7 °C and 73.2 °C in well 7121/5-1 and 7120/6-1, respectively. Assuming that the area has been uplifted 1000 meters, the maximum burial temperatures has been predicted to 104.5 °C in well 7121/5-1 and 108.9 °C in well 7120/6-1.

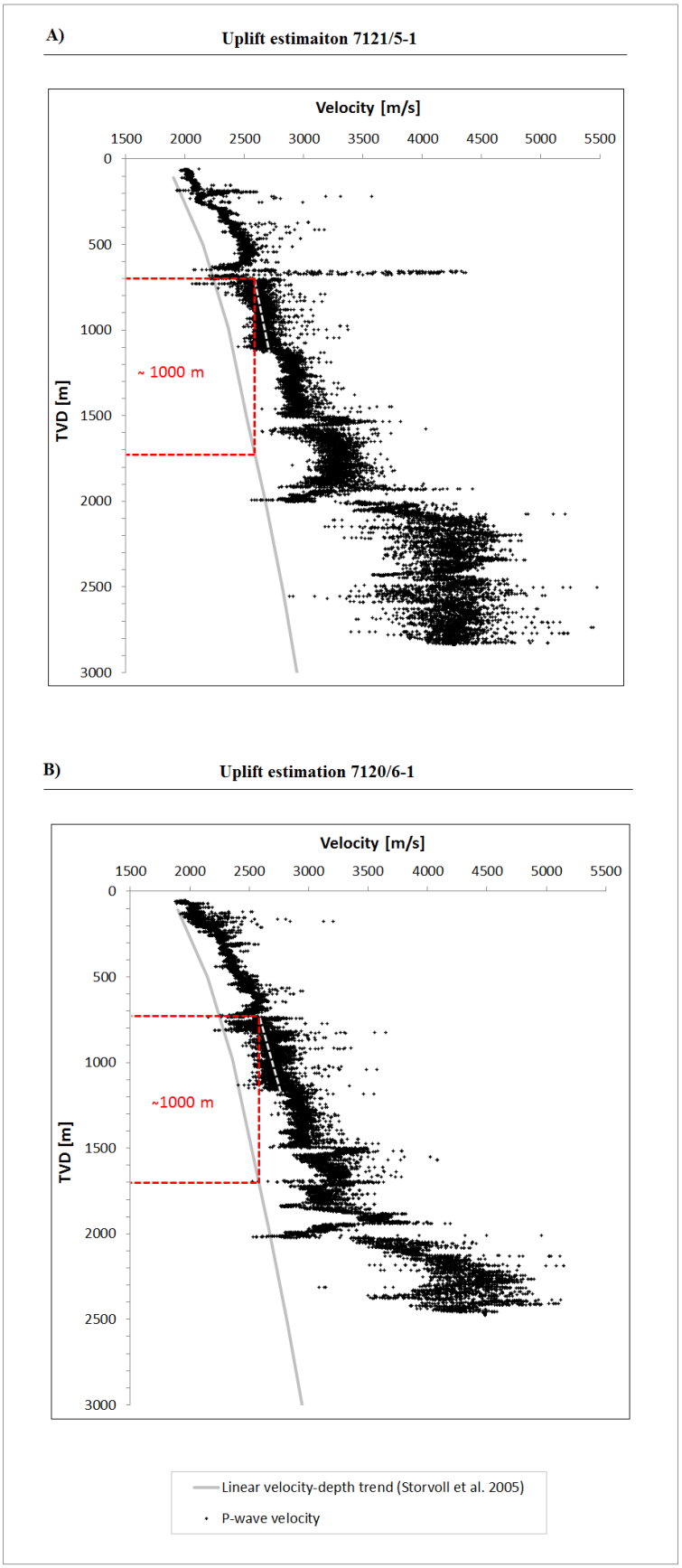

Figure 6.15: The figure displays the uplift estimation results from both wells where a shaly interval was correlated with the velocity depth trend of (Storvoll et al., 2005). The results suggest that the area has been uplifted approximately 1000 meters.

Table 6.1: The table displays the true vertical depths (TVD) and the predicted temperatures prior to- and after uplift with the reference level being the top of the Stø formation. The predicted temperatures derives from the calculated geothermal gradient presented in figure 6.10, and represents the present day geothermal gradient.

Well name	Top of Stø fm. 7121/5-1	Top of Stø fm. 7120/6-1
Geothermal gradient [°C/km]	34.7	35.7
Present day TVD [m]	2011	2049
Estimated present day temperature [°C]	69.7	73.2
Estimated TVD prior to uplift [m]	3011	3049
Estimated temperature prior to uplift [°C]	104.5	108.9

7. Discussion

7.1 Introduction

Reservoir quality is often referred to as the degree of preserved porosity and permeability within a reservoir in the subsurface. As mentioned, reservoir quality is a function of provenance and depositional environment which controls the initial rock properties prior to diagenesis. Further, during diagenesis the rock properties will be altered in response to various processes associated with shallow burial, mechanical- and chemical compaction. In this chapter results obtained from the petrographic and petrophysical analysis will be combined with the aim to image the reservoir quality of the Stø formation in well 7121/5-1 and 7120/6-1, located in the Hammerfest basin in the SW Barents Sea. As the resultant reservoir quality is a function of a great variety of initial properties and processes it is very important to understand these diversities within the rock of interest. First, relevant results obtained from the previous chapters will be related to provenance, depositional environment and facies. Since core logging not were included in this study, the results obtained within these topics will be compared and related to the published literature more frequently. Further, the results will be used to discuss processes related to diagenesis. At the end of this chapter the most important factors controlling the reservoir quality within the Stø formation will be presented, where their relative influence also will be discussed. This will finally be related to the porosity- and permeability distribution within the Stø formation where relative differences in reservoir quality will be suggested.

7.2 Provenance, depositional environment and facies

As mentioned, core logging was not performed in this study but the available core photos at NPD (Norwegian petroleum directory) webpages was used observed relative differences within the Stø formation. The petrographic results obtained in this thesis which can be linked to provenance and depositional environment will mainly be represented by the mineralogical and clay volume observations, respectively. From the petrophysical analysis, the gamma and density log will be used to interpret depositional environment.

7.2.1 Provenance

From figure 5.1 and 5.2, the results from the point count revealed that the mineralogical composition of the Stø formation is almost entirely composed of quartz. Other detrital grain constituents such as feldspar and lithic fragments only made up a minor fraction of the bulk volume. The nearly monomineralic composition of the Stø formation indicates deposition of a mature sediment. This could be a direct function of the source rock being eroded or other processes related transportation which has influenced these sediments before they reached their final depositional site. Even though, feldspar and lithic fragments most likely have been altered during various diagentical processes, the initial volume of these constituents must have been fairly low due to the high volume of quartz compared to the bulk volume. This may indicate that less stable minerals, like feldspar, may have been removed due to leaching and reworking. The quartz to feldspar ratio may increase in response to leaching of feldspar and precipitation of kalolinite, where subsequent reworking of the sediment may remove both constituents. In a setting where these processes are repeated, the quartz to feldspar ratio will increase and result in deposition of a mature sediment.

From the literature, (Pózer Bue and Andresen, 2015) studied zircon population ages within the Mesozoic successions located in Svalbard, where the aim was to better understand provenance changes over time. In the Svalbard area, a change in provenance occurs in the Middle Triassic (figure 7.1), where Early- to Middle Triassic sediments shows a response associated with zircon ages from a western source area, most likely east Greenland and Arctic Canada. In the Late Triassic successions, a quite different signature has been observed. This is characterized by a younger zircon population associated with the Uralian Mountain, which may indicate a shift from a western- to an eastern source area. Further, the Early/Middle Jurassic zircon-response show a signature which has been described as a combined response of the two endmember groups i.e., Early-Middle Triassic (western source) and Late Triassic (eastern source). The mixed zircon signature was interpreted to be a result of reworking of the eastern sourced Uralian sediments with possible renewed input from Greenland. The assumption regarding reworking of Late Triassic sediments were also based on the findings by (Mørk, 1999) which observed a distinct difference in sandstone maturity between Late Triassic- Early Jurassic sands both from Spitsbergen and the Hammerfest basin. With respect to the western Barents Sea, several source areas may prevailed in Triassic, including a southern source from Baltica, but the main sediment source in the Norwegian Barents Sea was probably located to the south-east and has been linked to the Uralian orogenic belt (Mørk, 1999, Glørstad-Clark

et al., 2010). The studies by (Pózer Bue and Andresen, 2015) and (Mørk, 1999), indicate that reworking of Triassic took place on a regional scale, from the SW Barents Sea in the south to Svalbard further north, which may explain the mature mineralogical composition of the Stø formation.

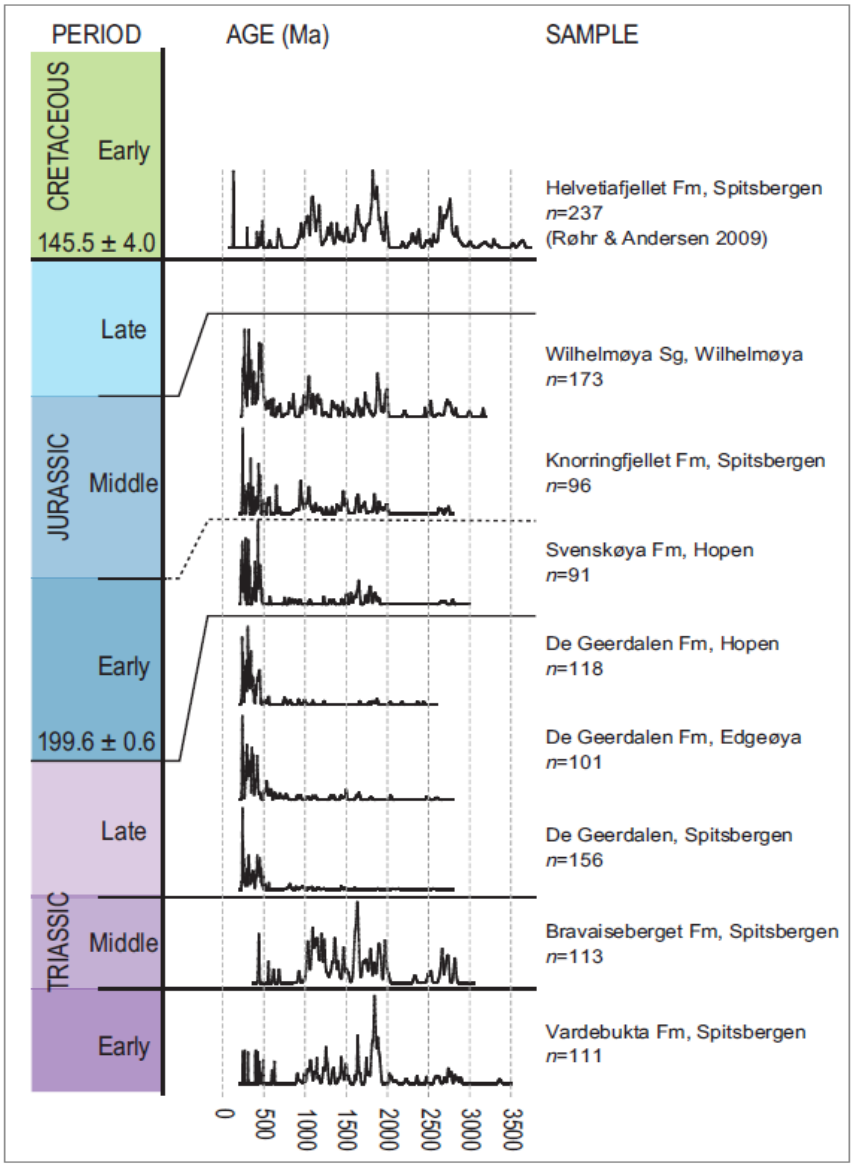

Figure 7.1: The figure displays various zircon populations associated with different sources areas in the Barents Sea region. Older zircons are interpreted to be sourced from the west; eastern Greeenland and Canada, whereas the younger zircons most likely derive from Ural Mountains in the east (Pózer Bue and Andresen, 2015).

7.2.2 Depositional environment

The observed clay-sized fraction, presented in figure 5.9 and 5.10, showed that the clay content where greater within the upper part of the Stø formation compared to the lower part. This corresponds to sequence A1/B1 and A2/B2, respectively. Further, the thin clay laminations (figure 5.9 A and figure 5.24) observed within the Stø formation were only detected in samples (thin sections) restricted to the upper part of Stø formation, i.e. sequence A1 and B1. Table 5.1 illustrates that all the sequences represents moderately well to well sorted grain size populations.

Based on the results from the petrophysical analysis, the gamma ray- and density log (figure 6.1 and 6.3, respectively) shows a separation between the upper- and lower part of the Stø formation which can be recognized as an increase in the response from both logs. The gamma ray log responses from both wells were interpreted to represent an upwards fining trend within the Stø formation. In addition, thin intervals with a significant higher response compared to the background response were suggested to be representing thin intervals possibly consisting of more clay rich sediments. These intervals were also detected in the density log (figure 6.3) where regions with considerably higher densities stand out as irregularities compared to the background trend. The estimated shale volumes, shown in figure 6.4, also indicate that the upper part of the Stø formation is more shale-rich. A separation was also observed between sequence B1 and B2 in figure 6.13, based on a model which describes the expected compaction evolution of sediments with different critical porosities (sorting). Sequence B2 plotted closer to the contact cement model, which would be an expected response for a lithology with small amounts of matrix at the time of deposition, according to these models. An example of core photos from the upper- and lower part of the Stø formation can be seen in figure 7.2, where the upper interval (B1 in this study) seems to be more clay-rich.

Figure 7.2: The figure displays an interval from the upper (A) - and lower(B) sequnce within the Stø formation, where the upper sequence seems to be more clay-rich. The example from the upper sequence (A) represent the interval from 2415 – 2417 m where thin section 14 (2415,25 m) and thin section 15 (2416, 2 m) have been obtained. The example from the lower sequence (B) displays the interval between 2461,5 to 2463,5 m where thin section 20 (2461, 8 m) is located. The core photos are taken from (NPD, 2016).

Based on the results from the petrographic analysis and the petrophysical analysis, a depositional environment and facies interpretation can be suggested in a more general manner. As described above, the separation observed between the upper- and lower sequence of the Stø formation, could possibly reflect a change in the depositional environment. In figure 7.3, a depositional environment interpretation has been suggested and displays a possible scenario which aims to explain the observed differences in clay content within the Stø formation. This interpretation is based on studies which have described that shallow marine environments dominated the western Barents Sea basins in the Early-Middle Jurassic (Worsley, 2008, Smelror et al., 2009). The differences in clay content between sequence A1/B1 and A2/B2 may reflect a change in the energy regime. The low clay content within the lower sequence (A2/B2) may be explained by the influence of a higher energy regime at the time of deposition, where the clay fraction was kept in suspension and transported further basinward. The higher clay content observed within the upper part (A1/B1) of the Stø formation may be explained by a relocation of the shoreline where more distal marine facies were moved landward. As mentioned, the thin clay laminations were only observed within sequence A1 and B1 and could possible represent more low-energy periods which resulted in deposition of suspended clay particles. The suggested shift in energy regime is also consistent with the upwards fining trend observed in the gamma ray- and density log. The degree of sorting, will not directly contribute to understand the depositional environment but well sorted sediments would be expected in a shallow marine setting.

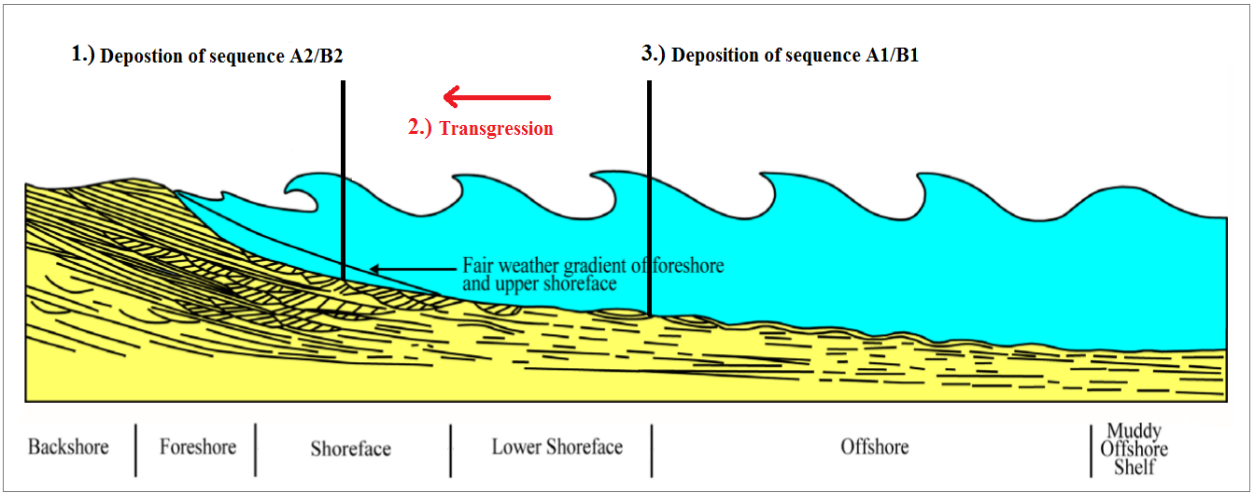

Figure 7.3: The figure illustrate a possible scenario related to deposition of the upper and lower sequence of the Stø formation which most likely have occurred in the following order: 1.) deposition of sequence A2/B2 which has been associated with near-shore facies and from this study reflected in the lower clay content compared to sequence A1/B1. 2.) a transgressive development of the shoreline causes a landward shift of facies associated with deeper marine environments. 3.) deposition of sequence A1/A2 reflected by a higher clay content. Figure modified from (Baniak et al., 2014)

From the literature, the Stø formation has been interpreted to represents mainly nearshore depositional environments, where facies such as foreshore, shoreface, estuarine and more distal shelf facies have been recognized (Berglund et al., 1986). The lower part has been associated with shoreline sediments, influenced by mainly wave processes whereas some intervals may have been tidal dominated (Olaussen et al., 1984). The upwards fining trend between the lower- and upper sequences has been related to a shift to more distal marine facies, and the upper part has been associated with lower shoreface facies (Berglund et al., 1986). This is consistent with the clay volume observations made in this study.

7.3 Diagenesis

7.3.1 Shallow burial

Leaching of feldspar and muscovite and precipitation of kaolinite is a process which has been associated with shallow burial, as the onset of this process has been linked to water flushing of the sediments close to the surface (Bjorlykke et al., 1992). In figure 5.12, the relation between muscovite and kaolinite were examined, and the results suggested a relation between these minerals where an increase/decrease in muscovite content corresponded to an increase/decrease in observed kaolinite. In figure 5.13, an actual evidence of this process was presented where the kaolinite almost entirely has replaced the muscovite grain. Further, by looking at the point count results from thin section 16 to 19 in figure 5.2 (7120/6-1), it becomes evident that no kaolinite was observed in these thin sections nor any mica. The relationship between muscovite and kaolinite indicates that most of the feldspar, if present, was leached and reworked at an earlier stage and that muscovite has been the primary precursor mineral for kaolinite after the final deposition.

The carbonate cement observed in this study is represented by dolomite cores encompassed in ankerite which normally occurs as isolated features. However, occasionally the ankerite occupies some of the neighboring pore space (figure 5.30). The most extensive lateral occurrence of ankerite observed is the one displayed in figure 5.30 (lower photomicrograph). Olaussen et al. (1984), described that the dolomite and ankerite most likely have been altered from calcite, which would explain the source of calcium. A possible iron-source may have been siderite, if siderite were present at an earlier stage.

7.3.2 Mechanical compaction

The estimated IGV presented in figure 5.20 and 5.21 displays generally lower IGV than would be expected for a quartz-rich well sorted sandstone, which might be even higher than a typical IGV of 25-30% at the boundary between mechanical and chemical compaction (Bjørlykke and Jahren, 2015). This is illustrated in figure 5.19, where estimated IGV within the Stø formation has been compared to the IGV compaction curve from Paxton et al. (2002). Rossi and Alaminos (2014) suggested that porosity loss due to mechanical compaction beyond an IGV of 26% would only be possible in extremely well sorted, uncemented quartz arenites. As significant amounts of quartz cement have been observed within the Stø formation, the low IGV are most likely not a result of continued mechanical compaction. As mentioned, it has been suggested that the quartz cement volume has been underestimated during the optical microscopy analyses (see section 5.3.1) which will result in lower IGV values than expected. The majority of the estimated IGV values in this study lie commonly in the range of 20-25% which suggests an error in IGV of < 5%. It can be assumed that the error in estimated IGV due to underestimation of quartz cement is made consistently in all the samples and hence can be used to describe relative differences in terms of IGV.

The IGV results indicate that well sorted and very fine grained sand (mean grain size) intervals within the Stø formation have the highest IGV (figure 5.22 and 5.23). This is consistent with published literature regarding experimental compaction studies, e.g. (Chuhan et al., 2002). This indicates that intervals with the finest detrital grain fraction and/or sorting had the best preserved porosity prior to chemical compaction. In terms of grain roundness, figure 5.17 indicated that the majority of the quartz grains were angular to sub-angular. It has been suggested that the grain angularity may be more rounded than predicted during the optical microscopy analyses (see section 5.3.1). Regarding compaction, Chuhan et al. (2003) described the influence of angularity upon porosity loss as function of increasing vertical effective stress. The study showed that the porosity loss was greater in samples with sub-angular grains compared to samples with sub-rounded grains, as the force acting at the grain contact becomes more concentrated in sediments with an angular grain surface (Chuhan et al., 2003). The degree of grain crushing within the Stø formation was insignificant, which may support the suggestion of more rounded grains and that porosity loss due to grain crushing can be considered a less important process. Nevertheless, the grain contacts results presented in figure 5.18 indicate that the Stø formation has experienced significant reorientation and close packing of the grains as the long and sutured grain contacts dominate.

At the boundary where the dominating porosity reducing mechanism changes from mechanical- to chemical compaction may be referred to as the transition zone. A significant increase in the P-wave velocity is often associated with this boundary, as small amounts of quartz cement stiffens the rock frame (Storvoll et al., 2005). Typically, the onset of quartz cementation will start at temperatures in the range of 70-80°C (Walderhaug, 1994). Assuming a geothermal gradient of 34°C/km (present day) this will correspond to a depth of about 2 km (figure 6.10). In figure 6.11, a sharp increase in P-wave velocity is observed in both wells at about 1200 meters. An increase in density is also observed at this level, but the density increase may be to significant to represent the small amounts of cement (compaction) associated with stiffening of the rock frame. The lower increase in the velocity- and density logs at about 2000 meters is far too deep to be considered a candidate for the transition zone, assuming that the area has experienced 1000 meters uplift (figure 6.15). In addition, a relation between the P-wave velocity and total porosity was also examined during the petrophysical analysis (not displayed in the results) in order to identify the transition zone. No significant increase in velocity with respect to a more or less constant porosity interval was observed, which could be an expected response at this boundary (Avseth, 2015). Hence, the boundary between the mechanical- and chemical compaction regime was not identified in this study.

7.3.3 Chemical compaction

7.3.3.1 Quartz cementation

The onset of noticeable quartz cementation is thought to start at temperatures of about 75°C (Walderhaug, 1994). From table 6.1 it becomes clear that this is a process that has occurred within the Stø formation in the studied wells as the maximum burial depth and temperature has been suggested to be about 3000 meters and 105-110°C, respectively, prior to the uplift. Further this suggests that the Stø formation was influenced by quartz cementation as the uplift occurred. The present day depth and temperature, as indicated by figure 6.10 and table 6.1, shows that the Stø formation is most likely located close to the boundary where this reaction is thought to occur, and hence quartz cementation may be an ongoing process.

Generally, the highest amount of observed quartz cement was identified within sequence A1 and B1 (figure 5.3 and 5.4), whereas the interval with the lowest cement volume was identified within sequence B2. In relation to porosity a trend can be observed where highly

cemented intervals correspond to intervals with poorer preserved porosity. On the contrary, intervals with less observed quartz cement correspond to higher porosity intervals. The calculated quartz cement volume obtained during the petrophysical analysis in figure 6.8 and 6.9 shows that there is commonly a discrepancy between the observed and estimated quartz cement volume in range of 5-10 %, and even higher in some intervals. This separation would be less significant if the quantification of the quartz cement volume in optical microscope were more accurate (see section 5.3.1). However, it seems that the relation between the observed- and calculated quartz cement volume succeeds to describe the relative increase/decrease in quartz cement volume in a broader context. This makes it possible to use the calculated cement volume to predict quartz cement trends between intervals with observed data. This is true in all the sequences, except for sequence B2. The observed data suggest a significant decrease in quartz cement from sequence B1 to B2, whereas the calculated quartz cement volume increases through this interval. The discrepancy can be partly explained by the underestimation of quartz cement, but will not correct for the entire deviation between observed- and calculated quartz cement. As the calculated quartz cement volume is estimated as direct function of the sonic velocity, the discrepancy may be further corrected by looking at velocity sensitive parameters. Some experimental studies have described the relation between small amounts of clay content and grain contact area with regard to sonic velocity. In terms of grain contact area (Fawad et al., 2011) observed an increase in sonic velocity with increasing grain size, and suggested that this partly was due to a greater grain contact area. However, as described by (Storvoll and Bjørlykke, 2004) this only seems to apply during initial stiffening of the framework, as continued cementation will reduce the stress at the grain contacts. Further, (Storvoll and Bjørlykke, 2004) described clay content with regard to velocity as an indirectly controlling factor. A correlation between clay content and sonic velocity was not found and the sonic velocity was suggested to be more sensitive to the structural position of the clay fragment than the total volume of clay (Storvoll and Bjørlykke, 2004). Sequence B2 has the lowest amounts of quartz cement- and matrix content and consist of coarser grained sand particles compared to the other sequences presented this study, and hence the arguments discussed above may additionally explain the discrepancy observed in this interval. A discussion regarding the low observed quartz cement volume within sequence B2 will be given below.

As mentioned in the previous section regrading IGV, the results indicated that intervals with very fine sand had the best preserved porosity after mechanical compaction. In figure 5.8,

where quartz cement is plotted against the mean grain size, it becomes evident that these intervals have the highest amount of cement volume. As described by several experimental studies (Heald and Renton, 1966, Walderhaug, 1996), the detrital grain surface area available for quartz cementation increases with a decrease in grain size (increase in phi scale). These intervals correspond to sequence A1 and B1, where an example from sequence A1 was presented in figure 5.5 along with an example from sequence B2 where quartz cement volume is significantly lower. In addition, the thin clay laminations observed in several of the thin sections where mainly located within sequence A1 and B1 (section 5.2.3). As mentioned in chapter 3, Walderhaug et al. (2003) investigated the relation between stylolite spacing and the degree of quartz cement volume and where they observed that regions located closer to a stylolite commonly was more quartz cemented. Based on the core photos presented in figure 5.6, where two examples of an interval with low- and high observed quartz cement volume and accompanying interpretation of the distance to the nearest stylolite were shown. The example from sequence B2, which has the lowest amount of observed quartz cement in this study, had a distance to the nearest stylolite of more than 1 meter. On contrary the example from sequence A1, the most significant cemented regions in this study, indicated a distance to the nearest stylolite in order of a few tens of centimeter. This indicates that dissolution of quartz at styloloites may be the most prominent source of silica in the Stø formation. Minor amounts of microstylolitization, where muscovite grains had started to dissolve quartz at grain contacts were also observed (figure 5.7). As described in section 7.3.1, nearly no muscovite was observed in the optical microscope within sequence B2, which may additionally contribute to the low quartz cement volume within this region. This can be considered a minor silica source within the Stø formation. Hence, the low quartz cement volume within sequence B2 is most likely controlled by the distance between stylolities and the lack of microstylolitization.

7.3.3.2 Precipitation of authigenic clay minerals associated with the chemical compaction regime

As temperature is an important parameter regarding precipitation of authigenic clay minerals a brief discussion of the interpreted maximum temperature within the studied wells will follow. Assuming that the study area has experienced approximately 1000 meters uplift (figure 6.15), the maximum burial depth of the Stø formation was about 3000 meters prior to the uplift (table 6.1). Even though the uplift estimation obtained in this study is based on a simple procedure, but the results are in agreement with published literature where often several approaches are used to predict uplift. (Baig et al., 2016) suggest an uplift estimate of about 1000 – 1125 meters in this region and (Storvoll et al., 2005) suggested an uplift estimate of 1055 meters in well 7121/5-1, which is the same well as used in this study. Based on the present day geothermal gradient this corresponds to a maximum temperature of approximately 110 °C (table 6.1). Thus, figure 6.10 indicates that alteration of smectite to illite could have occurred within the Stø formation, whereas the temperature may have been too low for illitization from K-feldspar and kaolinite.

A mixture of illite and microquartz were observed in several of the thin sections during the SEM analysis and as shown in figure 5.25 (micrograph C and D), the illite and microquratz mixture were commonly observed with a clear grain rim. This indicates that a detrital lithic fragment may have been the precursor for the illite and microquartz mixture. Further, pure illite were also observed in some of the samples. The pure illite was mainly recognized as pore-filling clay (figure 5.25 A), but partly illite coated quartz grains were observed in some regions (figure 7.4).

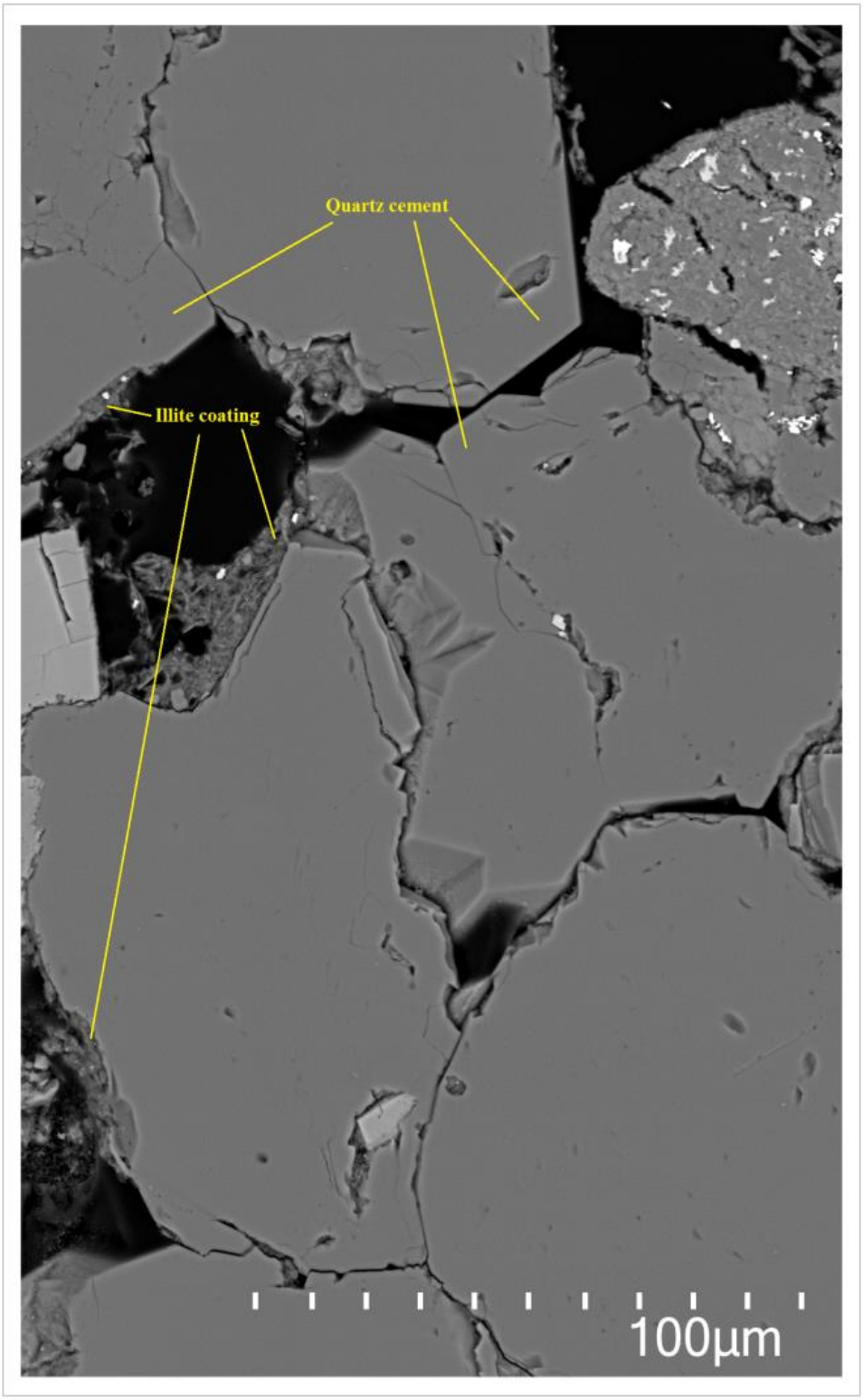

Figure 7.4: An example of illite present at the detrital quartz grain surfaces from thin section 14 in well 7120/6-1. The illite seems to only prevent quartz cementation locally.

As mentioned, K-feldspar and kaolinite are no longer stable together at temperatures above 130°C (Bjørlykke, 1998). Both K-feldspar and kaolinite have been observed during the petrographic analysis and in addition it is not likely that the Stø formation has reached these temperatures based on the uplift estimate. According to these arguments, it is not likely that the observed illite presented in section 5.3.2 is an alteration product of kaolinite and K-feldspar. This means that the observed illite in this study derives from an earlier diagentic process, which may be from illitization of smectite (S-1 reaction). However, no smectite has been observed during the petrographic analysis and hence this explanation is only valid if all the smectite has been altered to illite. This would be very likely as the Stø formation has been buried to depths of about 3000 meters and smectite is less stable at higher temperatuers, i.e.~ 50-60°C (Abercrombie et al., 1994). Several studies within shales e.g. (Dypvik, 1983, Thyberg et al., 2010) have shown that precipitation of significant amounts of illite from smectite have occurred as temperatures have reached 80 – 100°C. In sandstones, the S-I reaction starts at 65°C (Bjørlykke, 1998) and is thought to mainly be altered from aluminous minerals, e.g. smectite, (Bjorlykke et al., 1995). A simplified version of the smectite to illite reaction can be stated as (Peltonen et al., 2009):

$$\text{Smectite} + K^{+} \rightarrow \text{Illite} + SiO_2 + H_2O.$$

At about 65°C , the released silica from the S-I reaction may start to precipitate as quartz and the reaction will proceed to the right (Abercrombie et al., 1994). (Peltonen et al., 2009) observed microquartz within the clay matrix, though in mudstones, and suggested that these were a result of precipitation of quartz cement within the micro-pores. A similar process may explain the illite and microquartz mixture observed in this study. As mentioned, the grain rim observed in relation to the illite and microquartz mixture indicates recrystallization of lithic fragments. These fragments most have been very smectite-rich in order for S-I reaction to occur, and could probably represent pre-compacted smectitc clay fragments which were mixed with sediments during deposition. These arguments could possibly explain the formation of the observed illite and microquartz mixture in this study. In cases were pure illite has been observed in the pore spaces, the released silica from the S-I reaction may have precipitated as quartz cement on the detrital quartz grains rather than within the micro-pores

of the illite. The illite present at quartz grain surfaces are most likely detrital clay consisting of smectite and/or illite.

Albite was also observed during the petrographic analyses (figure 5.29), where they appeared as untwinned complete grains with no evidence of dissolution porosity. (Saigal et al., 1988) suggested that albitization may form from direct replacement of K-feldspar, assuming a constant supply of sodium and removal of potassium. They discussed the possibility of the removal and supply of potassium and sodium could be linked to the alteration of smectite to illite, where this reaction consumes potassium and releases sodium (Saigal et al., 1988). Evidence of direct replacement of feldspar may be related to the fact that the observed albite in this study lacked any indication of dissolution porosity and appears as complete grains. The direct replacement of K-feldspar by albite can be stated as (Saigal et al., 1988):

$$KAlSi_3O_8 + Na^+ \rightarrow NaAlSi_3O_8 + K^+.$$

Further it has been suggested that completely replaced K-feldspar grains reflect a balance between the dissolution rate of K-feldspar and the precipitation rate of albite (Saigal et al., 1988). Even though feldspars not were quantified during in the optical microscope analyses, this process may have increased the albite/K-feldspar ratio during diagenesis within the Stø formation, as albite was observed more frequently than K-feldspar during the SEM analysis.

7.4 Reservoir quality

As described in chapter 3 (section 3.4), the reservoir quality of a given lithology depends mainly upon porosity and permeability as these parameters controls the total hydrocarbon storage capacity and the fluid flow within a reservoir. The discussion above described the processes with respect to provenance, depositional environment and diagenesis observed within the Stø formation, which may have increased or decreased the reservoir quality. In the following, the most important processes will now be highlighted, combined and related to what kind of influence they have had on the reservoir quality. Finally, a discussion related to which sequence/sequences that has the best preserved reservoir quality, i.e. porosity and permeability will be presented.

The discussion above has indicated that all processes affecting sediments from the source area, to the depositional environment and through diagenesis are collectively responsible for resultant reservoir quality of Stø formation. For example quartz cementation, which has been suggested to be the most prominent porosity reducing mechanism within the Stø formation has been linked to parameters such as grain size and matrix content which is controlled by processes way before the onset of quartz cementation. These parameters are a direct function of provenance and depositional environment which emphasizes the importance that these processes had on resultant reservoir quality within the Stø foramtion. Heavily cemented intervals A1 and B1 where associated with grain size and the amount of clay- and matrix content, as these parameters controls the available grain surface area and the silica source mechanism, i.e. stylolitization. These intervals had also the highest IGV and further indicate the impact that quartz cement had on sequence A1 and B1 with respect to porosity reduction. Increased grain sizes and the low matrix content in sequence A2 and B2 compared to A1 and B1 are thought to be responsible for the low quartz cement volume within this interval and hence better preserved porosity. Further, sorting and grain size had a great influence on porosity preservation during the mechanical compaction regime, reflected by the IGV with respect to these parameters. Sorting is also a direct function of pre-diagenetic processes and has been associated with reworking of sediments and depositional environment. In addition, the high detrital quartz content, also directly linked to provenance and depositional environment, may additionally have contributed to retard mechanical compaction due the rigidity of the quartz grains.

The processes mentioned above are thought to be most important reservoir quality controlling factors within the Stø formation. Minor reservoir quality controlling factors are mostly related

to precipitation of clay minerals. Dissolution of muscovite may produce secondary porosity which could slightly increase the reservoir quality, but due to the precipitation of kaolinite there is most likely no net gain in porosity (Bjørlykke and Jahren, 2015). Further, the permeability may be reduced due to pore-filling kaolinite. Precipitation of illite at the expense of smectite may slightly increase the reservoir quality due to the greater surface area of smectite, and may be increasingly more important to consider in very smectite rich reservoirs. Within the Stø formation this reaction may have locally increased the reservoir quality, but in the higher porosity intervals like sequence B2, where only small amounts of clay and matrix was observed, this reaction would not be very important in terms of reservoir quality. As the majority of the observed illite has been associated with alteration of a pre-compacted smectite-rich fragment, there has most likely not been any net gain in porosity. As mentioned, small amounts of partly illite coated quartz grains were observed in this study, but it seems that the grain coating fails to prevent quartz cementation. In order to prevent quartz cementation effectively by grain coating, (Storvoll et al., 2002) suggested that the grain coating must be continues, cover the entire grain surface and be present on the majority of the grains within the sample. This is not the case within any of the intervals examined in this study and hence grain coating is suggested to have had an insignificant impact on the quartz cement volume. The replacement of K-feldspar from albite may alter the pore size and geometry and hence may be considered processes with regard to reservoir quality (Saigal et al., 1988). In the Stø formation this is suggested to be a minor process which not drastically changes the reservoir quality. The observed dolomite and ankerite may locally reduce porosity and permeability and if these features occurs as more lateral extensive beds they may significantly reduce the vertical permeability. However, such beds are not observed in this study but they could be present beyond the intervals with observed data.

3.4.1 Porosity and permeability

In terms of porosity, figure 6.7 displayed the porosity distribution within the Stø formation in both wells based on the total porosity (neutron-density porosity) from the petrophysical analysis. This figure showed that the highest porosity values were located in well 7120/6-1 where about 35% of the porosity data are in the range of 18-19% porosity, and the remaining data displays a porosity of 11 to 17%. In well 7121/5-1, the porosity values are generally lower and are commonly in the range of 13 to 17%. From figure 6.6, which displays the porosity of both the observed- and calculated porosity as function of depth in well 7120/6-1 it

becomes clear that the best preserved porosity interval is within sequence B2. Both the observed and calculated porosity increases from sequence B1 to sequence B2. In well 7121/5-1 a similar trend with depth can be seen (figure 6.5), where the lower sequence A2 displays slightly higher porosity values compared with A1. However, the interval between 2420 and 2430 m shows an interval where both the observed- and calculated porosity decreases. This may be explained by the increase in quartz cement volume through this interval as seen in figure 6.8, which further can be related to the shale volume estimation (figure 6.4) and density log (figure 6.3) which indicates that small amounts of matrix may be present in this region. This was suggested to be typical intervals where stylolite formation was most prominent in the discussion above. The porosity distribution values discussed above originated from the calculated porosity and it should be noted that there is a discrepancy between the observed- and calculated porosity (figure 6.5 and 6.6) within the Stø formation. The observed porosity is commonly 5-8% lower than the calculated porosity, but there are intervals where there is a higher degree of agreement between the two approaches. The observed porosity suggests that there is generally higher porosity in the lower sequence of the Stø formation. However, there are intervals within the upper sequence with similar porosity values, but intervals with significantly higher cement volumes and hence lower porosity occurs sporadically. Sequence A1 and B1 shows porosity values between 4-14%, but the majority of the values are observed to be below 8% (figure 5.3). In sequence A2 and B2 the porosity values ranges from 8-13%, but the majority of the values lies in upper porosity range. In sequence B2 nearly all the values are above 12% (figure 5.4). In terms of reservoir cut-off values with respect to the observed porosity, some of individual intervals within the upper sequence of the Stø formation may be considered inadequate as an economical reservoir, but this would again depend on the saturating fluid and permeability. In a broader context the Stø formation can be classified as a reservoir with god reservoir quality and where the best reservoir quality is restricted to the lower sequence.

Even though porosity has been the parameter that has been quantified and most extensively discussed in this study, the results may be used to suggest permeability differences in a more general manner. From the discussion above the upper sequences (A1 and B1) has been characterized as intervals with a generally higher quartz cement- and matrix/ clay volume, than the lower sequences (A2 and B2). Further, the thin clay laminations where always observed within the upper interval within the Stø formation. This may indicate that the

permeability, and especially the vertical permeability, is lower in the upper part of the Stø formation. Further, this may also result in reservoir compartmentalization, which would make reservoir drainage more challenging.

8. Conclusion

The main objective in this study has been to image the reservoir quality of the Stø formation related to two wells within the Hammerfest basin in the SW Barents Sea. The reservoir quality has been described as a function of provenance, depositional environment and diagenesis where the results obtained in this thesis indicates that the following processes have influenced the resultant reservoir quality within the Stø formation:

- Provenance and depositional environment have been of great importance for the resultant reservoir quality as these processes determined mineralogy, sorting and grain size within the Stø formation.
- The best sorted- and finest sand sized intervals had the best preserved porosity after mechanical compaction, displayed by the predicted IGV with respect to these parameters.
- The results showed that stylolitization is the major cause of silica dissolution which further has been linked to the most heavily quartz cemented intervals within the Stø formation. A relationship between grain size and quart cement volume was observed where a higher cement volume is associated with regions consisting of very fine sand.
- Intervals with the best preserved porosity after mechanical compaction are the same regions with the most prominent porosity reduction during the chemical compaction regime, due to quartz cementation. Hence, quartz cementation is the major porosity reducing agent within the chemical compaction regime and is most widespread within the upper part of the Stø formation, represented by sequence A1 and B1 in this study.
- High-porosity intervals, represented by sequence A2 and B2, are intervals with the lowest quartz cement volume. This is also regions with a greater distance between stylolites and where micro-stylolites are less commonly observed. This was especially true within sequence B2, which is the interval with the best preserved porosity. The absence of clay laminations within this interval has been related to the depositional environment.
- In terms of observed porosity, sequence A1 and B1 displays a great range of porosity values ranging from 14% at best to 4% at the lowest. However, the majority of the porosity values are below 8%. In sequence A2 and B2 the porosity values are higher

and commonly lies in the range of 8-13%. In sequence B2 nearly all the porosity values are above 12%.

- The results showed that muscovite has been the main precursor mineral for kaolinite after final depostion. Precipitation of authigenic kaolinite is suggested to have a minor influence on the reservoir quality, but locally kaolinite may reduce porosity and permeability.
- The observed illite within the Stø formation originates from the S-I reaction, where the released silica precipitates as quartz cement within the micro-pores of the illite or as quartz cement on detrial quartz grain surfaces. The main smectite source is thought be pre-compacted smectitc clay fragments which were mixed with sediments during deposition. This interpretation is based on the observed grain rim which commonly envelopes the clay/cement mixture. Illite forming from the reaction between kaolinite and K-feldspar was not observed.
- Due to the relatively small amounts of authigenic clay minerals within the Stø formation, clay forming processes have had a minor influence on the reservoir quality.

References

Abercrombie, H. J., Hutcheon, I. E., Bloch, J. D. & De Caritat, P. 1994. Silica activity and the smectite-illite reaction. *Geology,* 22**,** 539-542.

Ajdukiewicz, J. M. & Lander, R. H. 2010. Sandstone reservoir quality prediction; the state of the art. *AAPG Bulletin,* 94**,** 1083-1091.

Asquith, G. B. & Krygowski, D. 2004a. Gamma ray (Chapter 3). *In:* MANCINI, E. A. (ed.) *Basic Well Log Analysis.* 2 ed. Tulsa, Oklahoma: AAPG

Asquith, G. B. & Krygowski, D. 2004b. Porosity Logs (Chapter 4). *In:* MANCINI, E. A. (ed.) *Basic Well Log Analysis.* 2 ed. Tulsa, Oklahoma: AAPG

Avseth, P. 2015. Explorational Rock Physics: The Link between Geological Processes and Geophysical Observables (Chapter 18). *In:* BJØRLYKKE, K. (ed.) *Petroleum Geoscience - from sedimentary environments to rock physics.* Verlag Berlin Heidelberg: Springer.

Avseth, P., Mavko, G. & Mukerji, T. 2005. Introduction to rock physics. *Quantitative Sesimic Interpretation - Applying rock physics tools to reduce interpretaion risk* United Kingdom: Cambridge Unveristy Press.

Baig, I., Faleide, J. I., Jahren, J. & Mondol, N. H. 2016. Cenozoic exhumation on the southwestern Barents Shelf: Estimates and uncertainties constrained from compaction and thermal maturity analyses. *Marine and Petroleum Geology,* 73**,** 105-130.

Baniak, G. M., Gingras, M. K., Burns, B. A. & George Pemberton, S. 2014. An example of a highly bioturbated, storm-influenced shoreface deposit: Upper Jurassic Ula Formation, Norwegian North Sea. *Sedimentology,* 61**,** 1261-1285.

Berglund, L. T., Augustson, J., Færseth, R. B. F., Gjelberg, J. & Ramberg-Moe, H. 1986. The evolution of the Hammerfest basin. *In:* SPENCER, A. M. (ed.) *Habitat of hydrocarbons on the Norwegian Continental Shelf. Norwegian Petroleum Society.* Springer.

Bjorlykke, K. 1993. Quartz cementation in sedimentary basins. *AAPG Bulletin,* 77.

Bjorlykke, K., Aagaard, P., Egeberg, P. K., Simmons, S. P., Cubitt, J. M. & England, W. A. 1995. Geochemical constraints from formation water analyses from the North Sea and the Gulf Coast basins on quartz, feldspar and illite precipitation in reservoir rocks. *The geochemistry of reservoirs***,** 33-50.

Bjorlykke, K., Nedkvitne, T., Ramm, M., Saigal, G. C. & Morton, A. C. 1992. Diagenetic processes in the Brent Group (Middle Jurassic) reservoirs of the North Sea: an overview. *Geology of the Brent Group***,** 263-287.

Bjørkum, P. A., Walderhaug, O. & Nadeau, P. H. 2001. Thermally driven porosity reduction: Impact on basin subsidence. *Geological Society Special Publication,* 188**,** 385-392.

Bjørlykke, K. 1998. Clay mineral diagenesis in sedimentary basins - A key to the prediction of rock properties. Examples from the North Sea Basin. *Clay Minerals,* 33**,** 14-34.

Bjørlykke, K. 2014. Relationships between depositional environments, burial history and rock properties. Some principal aspects of diagenetic process in sedimentary basins. *Sedimentary Geology,* 301**,** 1-14.

Bjørlykke, K. 2015. Introduction to Sedimentology - Sediment transport and sedimentary environments *In:* BJØRLYKKE, K. (ed.) *Petroleum Geoscience: From sedimentary environments to rock physics* Berlin, Heidelberg: Springer.

Bjørlykke, K. & Jahren, J. 2012. Open or closed geochemical systems during diagenesis in sedimentary basins: Constraints on mass transfer during diagenesis and the prediction of porosity in sandstone and carbonate reservoirs. *AAPG Bulletin,* 96**,** 2193-2214.

Bjørlykke, K. & Jahren, J. 2015. Sandstones and Sandstone Reservoirs (Chapter 4) *In:* BJØRLYKKE, K. (ed.) *Petroleum Geoscience: From Sedimentary Environments to Rock Physics.* Berlin, Heidelberg: Springer

Bloch, S., Lander, R. H. & Bonnell, L. M. 2002. Anomalously high porosity and permeability in deeply buried sandstone reservoirs: Origin and predictability. *AAPG Bulletin,* 86**,** 301-328.

Boggs, S. 2011. *Principles of sedimentology and stratigraphy* Upper Saddle River, N.J, Pearson Prentice Hall.

Chuhan, F. A., Bjørlykke, K. & Lowrey, C. 2000. The role of provenance in illitization of deeply buried reservoir sandstones from Haltenbanken and north Viking Graben, offshore Norway. *Marine and Petroleum Geology,* 17**,** 673-689.

Chuhan, F. A., Kjeldstad, A., Bjørlykke, K. & Heg, K. 2003. Experimental compression of loose sands: relevance to porosity reduction during burial in sedimentary basins. *Canadian Geotechnical Journal,* 40**,** 995-1011.

Chuhan, F. A., Kjeldstad, A., Bjørlykke, K. & Høeg, K. 2002. Porosity loss in sand by grain crushing—experimental evidence and relevance to reservoir quality. *Marine and Petroleum Geology,* 19**,** 39-53.

Dalland, A., Worsley, D. & Ofstad, K. 1988. A litostratigraphic scheme for the Mesozoic and Cenozoic succession offshore mid- and northern Norway. *NPD Bulletin No. 4***,** 42-51.

Dimakis, P., Braathen, B. I., Faleide, J. I., Elverhøi, A. & Gudlaugsson, S. T. 1998. Cenozoic erosion and the preglacial uplift of the Svalbard–Barents Sea region. *Tectonophysics,* 300**,** 311-327.

Doré, A. G. 1995. Barents Sea Geology, Petroleum Resources and Commercial Potential. *Arctic,* 48**,** 207-221.

Doré, A. G. & Jensen, L. N. 1996. The impact of late Cenozoic uplift and erosion on hydrocarbon exploration: offshore Norway and some other uplifted basins. *Global and Planetary Change,* 12**,** 415-436.

Dott, R. H., Jr. 1964. Wacke, graywacke and matrix; what approach to immature sandstone classification? *Journal of Sedimentary Petrology,* 34**,** 625-632.

Duran, E. R., Primio, R., Anka, Z., Stoddart, D. & Horsfield, B. 2013. 3D-basin modelling of the Hammerfest Basin (southwestern Barents Sea): A quantitative assessment of petroleum generation, migration and leakage. *Marine and Petroleum Geology,* 45**,** 281-303.

Dvorkin, J. & Nur, A. 1996. Elasticity of high-porosity sandstones: Theory for two North Sea data sets. *Geophysics,* 61**,** 1363-1370.

Dypvik, H. 1983. Clay mineral transformations in Tertiary and Mesozoic sediments from North Sea. *AAPG Bulletin,* 67**,** 160-165.

Faleide, J. I., Bjørlykke, K. & Gabrielsen, R. H. 2015. Geology of the Norwegian Contiental Shelf (Chapter 25) *In:* BJØRLYKKE, K. (ed.) *Petroleum Geoscience: From Sedimentary Environments to Rock Physics.* Berlin, Heidelberg: Springer

Faleide, J. I., Gudlaugsson, S. T. & Jacquart, G. 1984. Evolution of the western Barents Sea. *Marine and Petroleum Geology,* 1**,** 123,IN1,129,IN5,137-128,IN4,136,IN8,150.

Fawad, M., Mondol, N. H., Jahren, J. & Bjørlykke, K. 2011. Mechanical compaction and ultrasonic velocity of sands with different texture and mineralogical composition. *Geophysical Prospecting,* 59**,** 697-720.

Folk, R. L. 1974. *Petrology of sedimentary rocks : The University of Texas Geology 370 K, 383 L, 383 M,* Austin, Texas, Hemphill`s.

Gabrielsen, R. H. 1984. Long-lived fault zones and their influence on the tectonic development of the southwestern Barents Sea. *Journal of the Geological Society of London,* 141**,** 651-662.

Gabrielsen, R. H., Færseth, R. B., Jensen, L. N. & Kalheim, J. E. 1990. Structural elements of the Norwegian continental shelf: The Barents Sea region *NPD Bulletin No. 6.* **,** 33.

Glørstad-Clark, E., Faleide, J. I., Lundschien, B. A. & Nystuen, J. P. 2010. Triassic seismic sequence stratigraphy and paleogeography of the western Barents Sea area. *Marine and Petroleum Geology,* 27**,** 1448-1475.

Halland, E. K., Muljezinovic, J. & Riis, F. 2013. CO2 storage atlas Barents Sea. *Norwegian Petroleum Directorate*.

Heald, M. T. & Renton, J. J. 1966. Experimental study of sandstone cementation *Jornual of Sedimentary Petrology,* 36**,** 977-991.

Henriksen, E., Bjornseth, H. M., Hals, T. K., Heide, T., Kiryukhina, T. A., Klovjan, O. S., Larssen, G. B., Ryseth, A. E., Ronning, K., Sollid, K., Stoupakova, A. V., Spencer, A. M., Embry, A. F., Gautier, D. L., Stoupakova, A. V. & Sorensen, K. 2011. Uplift and erosion of the greater Barents Sea; impact on prospectivity and petroleum systems (Chapter 17). *Arctic Petroleum Geology,* 35**,** 271-281.

James, N. P. & Dalrymple, R. W. 2010. Introduction to Siliciclastic Facies Models *In:* JAMES, N. P. & DALRYMPLE, R. W. (eds.) *Facies Models 4* Canada: Geological Association of Canada.

Lander, R. H., Larese, R. E. & Bonnell, L. M. 2008. Toward more accurate quartz cement models; the importance of euhedral versus noneuhedral growth rates. *AAPG Bulletin,* 92**,** 1537-1563.

Lundegard, P. D. 1992. Sandstone porosity loss; a "big picture" view of the importance of compaction. *Journal of Sedimentary Petrology,* 62**,** 250-260.

Lundschien, B. A., Høy, T. & Mørk, A. 2014. Triassic hydrocarbon potential in the Northern Barents Sea; integrating Svalbard and stratigraphic core data. *Norwegian Petroleum Directorate Bulletin***,** 3-20.

Marcussen, Ø., Maast, T. E., Mondol, N. H., Jahren, J. & Bjørlykke, K. 2010. Changes in physical properties of a reservoir sandstone as a function of burial depth – The Etive Formation, northern North Sea. *Marine and Petroleum Geology,* 27**,** 1725-1735.

Mcbride, E. F. 1989. Quartz cement in sandstones: a review. *Earth-Science Reviews,* 26**,** 69-112.

Mørk, A., Dallmann, W. K., Dypvik, H., Johannessen, E. P., Larssen, G. B., Nagy, J., Nøttvedt, A., Olaussen, S., Pcelina, T. M. & Worsley, D. 1999. Mesozoic Lithostratigraphy. *In:* DALLMANN, W. K. (ed.) *Lithostratigraphic Lexicon of Svalbard: Upper Paleozoic to Quaternary Bedrock Review and Recommendation for Nomenclature Use.* Norwegian Polar Institute, Tromsø.

Mørk, M. B. E. 1999. Compositional variations and provenance of triassic sandstones from the barents shelf. *Journal of Sedimentary Research,* 69**,** 690-710.

Npd. 2016. *Norwegian Petroleum Directorate - Fact pages* [Online]. Available: http://www.npd.no/en/ [Accessed 27.04.2016].

Nyland, B., Jensen, L. N., Skagen, J., Skarpnes, O. & Vorren, T. 1992. Tertiary Uplift and Erosion in the Barents Sea: magnitude, Timing and Consequences. *Structural and Tectonic Modelling and Its Application to Petroleum Geology. Norwegian Petroleum Society. Elsevier, Amsterdam* 153-162.

Ohm, S. E., Karlsen, D. A. & Austin, T. J. F. 2008. Geochemically driven exploration models in uplifted areas: Examples from the Norwegian Barents Sea. *AAPG Bulletin,* 92**,** 1191-1223.

Olaussen, S., Dalland, A., Gloppen, T. G. & Johannessen, E. P. 1984. Depositional environment and diagenesis of Jurassic reservoir sandstones in the eastern part of Troms area. *Petroleum Geology of the North European Margin. Norwegian Petroleum Society***,** 61-79.

Osborne, M. J. & Swarbrick, R. E. 1997. Mechanisms for Generating Overpressure in Sedimentary Basins: A Reevaluation. *AAPG Bulletin,* 81**,** 1023-1041.

Ostanin, I., Anka, Z., Di Primio, R. & Bernal, A. 2012. Identification of a large Upper Cretaceous polygonal fault network in the Hammerfest basin: Implications on the reactivation of regional faulting and gas leakage dynamics, SW Barents Sea. *Marine Geology,* 332-334**,** 109-125.

Paxton, S. T., Szabo, J. O. & Ajdukiewicz, J. M. 2002. Construction of an intergranular volume compaction curve for evaluating and predicting compaction and porosity loss in rigid-grain sandstone reservoirs. *AAPG Bulletin,* 86**,** 2047-2065.

Peltonen, C., Marcussen, Ø., Bjørlykke, K. & Jahren, J. 2009. Clay mineral diagenesis and quartz cementation in mudstones: The effects of smectite to illite reaction on rock properties. *Marine and Petroleum Geology,* 26**,** 887-898.

Pittman, E. D. & Larese, R. E. 1991. Compaction of lithic sands: Experimental results and applications. *AAPG Bulletin,* 75.

Pittman, E. D., Larese, R. E. & Milton, T. H. 1992. Clay coats: occurrence and relevance to preservation of porosity in sandstones. *Origin, Diagenesis and Petrophysics of Clay Minerals in Sandstones. Society for Sedimentary Geology (SEPM),* 47.

Powers, M. C. 1953. A new roundness scale for sedimentary particles. *Journal of Sedimentary Petrology,* 23**,** 117-119.

Pózer Bue, E. & Andresen, A. 2015. Constraining depositional models in the Barents Sea region using detrital zircon U-Pb data from Mesozoic sediments in Svalbard. *Geological Society Special Publication,* 386**,** 261-279.

Rossi, C. & Alaminos, A. 2014. Evaluating the mechanical compaction of quartzarenites: The importance of sorting (Llanos foreland basin, Colombia). *Marine and Petroleum Geology,* 56**,** 222-238.

Saigal, G. C. & Bjørlykke, K. 1987. Carbonate cements in clastic reservoir rocks from offshore Norway-relationships between isotopic composition, textural development and burial depth. *Geological Society Special Publication,* 36**,** 313-324.

Saigal, G. C., Morad, S., Bjørlykke, K., Egeberg, P. K. & Aagaard, P. 1988. Diagenetic albitization of dettrital K-feldspar in Jurassic; Lower Cretaceous and Tertiary clastic reservoir rocks from offshore Norway. Textures and origin. *Jornual of Sedimentary Petrology,* 58**,** 1003-1013.

Santin, C. E., Abel, M., Goldberg, K. & De Ros, L. F. 2009. Automatic Detection of the Degree of Compaction in Reservoir Rocks Based on Visual Knowledge. *AAPG Annual Convention and Exhibition.* Denver, Colorado, USA.

Smelror, M., Basov, V. A. & Norges Geologiske, U. 2009. *Atlas : geological history of the Barents Sea,* Trondheim, Geological Survey of Norway.

Storvoll, V., Bjoerlykke, K., Mondol, N. & Storvoll, V. 2005. Velocity-depth trends in Mesozoic and Cenozoic sediments from the Norwegian Shelf. *AAPG Bulletin,* 89**,** 359-381.

Storvoll, V. & Bjørlykke, K. 2004. Sonic velocity and grain contact properties in reservoir sandstones. *Petroleum Geoscience,* 10**,** 215-226.

Storvoll, V., Bjørlykke, K., Karlsen, D. & Saigal, G. 2002. Porosity preservation in reservoir sandstones due to grain-coating illite: a study of the Jurassic Garn Formation from the Kristin and Lavrans fields, offshore Mid-Norway. *Marine and Petroleum Geology,* 19**,** 767-781.

Szabó, N. 2011. Shale volume estimation based on the factor analysis of well-logging data. *Acta Geophysica,* 59**,** 935-953.

Taylor, T. R., Giles, M. R., Hathon, L. A., Diggs, T. N., Braunsdorf, N. R., Birbiglia, G. V., Kittridge, M. G., Macaulay, C. I., Espejo, I. S., Ajdukiewicz, J. M. & Lander, R. H. 2010. Sandstone diagenesis and reservoir quality prediction; models, myths, and reality. *AAPG Bulletin,* 94**,** 1093-1132.

Thyberg, B., Jahren, J., Winje, T., Bjørlykke, K., Faleide, J. I. & Marcussen, Ø. 2010. Quartz cementation in Late Cretaceous mudstones, northern North Sea: Changes in rock properties due to dissolution of smectite and precipitation of micro-quartz crystals. *Marine and Petroleum Geology,* 27**,** 1752-1764.

Walderhaug, O. 1994. Temperatures of quartz cementation in Jurassic sandstones from the Norwegian continental shelf; evidence from fluid inclusions. *Journal of Sedimentary Research, Section A: Sedimentary Petrology and Processes,* 64**,** 311-323.

Walderhaug, O. 1996. Kinetic modeling of quartz cementation and porosity loss in deeply buried sandstone reservoirs. *AAPG Bulletin,* 80**,** 731-745.

Walderhaug, O., Bjoerkum, P. & Walderhaug, O. 2003. The effect of stylolite spacing on quartz cementation in the lower Jurassic Stoe formation, southern Barents Sea. *Journal of Sedimentary Research,* 73.

Walderhaug, O., Bjørkum, P. A., Nadeau, P. H. & Langnes, O. 2001. Quantitative modelling of basin subsidence caused by temperature-driven silica dissolution and reprecipitation. *Petroleum Geoscience,* 7**,** 107-113.

Wilson, D. M. & Pittman, E. D. 1977. Authigenic clays in sandstones: Recognition and influence on reservoir properties and paleoenvironmental analysis *Journal of Sedimentary Petrology*, 47**,** 3-31.

Worsley, D. 2008. The post-Caledonian development of Svalbard and the western Barents Sea. *Polar Research*, 27**,** 298-317.

Yuan, G., Cao, Y., Cluyas, J., Li, X., Xi, K., Wang, Y., Jia, Z., Sun, P. & Oxtoby, N. H. 2015. Feldspar dissolution, authigenic clays, and quartz cements in open and closed sandstone geochemical systems during diagenesis: Typical examples from two sags in Bohai Bay Basin, East China. *AAPG Bulletin,* 99**,** 2121-2154.

Øvrebø, O. & Talleraas, E. 1977. The Structural geology of the Troms Area (Barents-Sea). *An International Journal on Human Geography and Environmental Sciences*, 1**,** 47-54.

Appendix

Appendix A: The table displays the point count results of thin sections within the Stø formation in well 7121/5-1 and 7120/6-1. Samples 1 to 8 are from well 7121/5-1 and samples 9 to 20 are from well 7120/6-1. The data are presented in fraction [v/v].

Sample	Quartz	Rock fragments	Feldspar	Muscovite	Matrix	Kaolinite	Quartz cement	Carbonate cement	Primary porosity	Secondary porosity	IGV	Mean grain size [phi scale]	Sorting
1	0.81	0.015	-	-	0.03	-	0.05	0.02	0.08	0.01	0.17	2.93	0.409
2	0.67	0.013	-	0.003	0.10	0.010	0.09	0.03	0.06	0.03	0.29	3.54	0.369
3	0.69	0.005	-	0.008	0.13	0.010	0.10	0.01	0.05	0.01	0.29	3.62	0.355
4	0.73	0.005	-	-	0.09	0.008	0.10	0.02	0.06	-	0.27	3.45	0.366
5	0.75	0.003	-	0.003	0.11	0.003	0.05	0.01	0.07	0.01	0.24	3.29	0.500
6	0.76	0.020	-	0.003	0.06	0.005	0.04	0.01	0.11	-	0.22	2.51	0.488
7	0.77	0.005	-	-	0.09	0.003	0.08	0.01	0.05	-	0.23	2.93	0.416
8	0.74	0.008	-	0.003	0.08	0.005	0.09	0.01	0.08	-	0.25	2.89	0.343
9	0.75	0.015	-	0.008	0.07	0.015	0.08	0.02	0.04	0.01	0.22	3.30	0.342
10	0.73	0.018	-	0.003	0.04	0.003	0.05	0.01	0.15	-	0.25	3.01	0.382
11	0.77	0.005	-	-	0.05	-	0.08	0.01	0.09	-	0.22	2.67	0.683
12	0.77	0.010	-	-	0.05	-	0.05	0.01	0.12	-	0.23	2.21	0.416
13	0.76	0.008	-	0.005	0.09	-	0.09	0.02	0.04	-	0.23	3.36	0.353
14	0.74	0.005	-	-	0.13	-	0.06	0.03	0.05	-	0.26	3.42	0.351
15	0.73	0.003	-	0.008	0.08	-	0.08	0.01	0.09	-	0.26	3.32	0.319
16	0.76	-	-	-	0.08	-	0.11	0.01	0.05	-	0.24	3.08	0.341
17	0.78	0.010	-	-	0.06	-	0.02	0.01	0.13	-	0.21	2.14	0.536
18	0.81	-	-	-	0.02	-	0.03	0.01	0.12	0.01	0.19	2.53	0.383
19	0.84	0.005	-	-	0.01	-	0.03	0.01	0.11	0.01	0.15	2.39	0.535
20	0.79	0.005	-	-	0.02	0.005	0.03	0.01	0.14	0.02	0.19	2.45	0.539